Testing the Standard Model Lepton Symmetries in Collider and Fixed-Target Experiments

---

Dissertation

zur

Erlangung der naturwissenschaftlichen Doktorwürde
(Dr.sc.nat.)

vorgelegt der

Mathematisch-naturwissenschaftlichen Fakultät

der

Universität Zürich

von

Iaroslava Bezshyiko

aus

der Ukraine

Promotionskommission

Prof. Dr. Nicola Serra (Leitung der Dissertation)
Dr. Patrick Owen
Dr. Katharina Müller
Pd. Dr. Olaf Steinkamp
Prof. Dr. Guy Wilkinson
Prof. Dr. Marta Calvi

Zürich, 2021

Contents

List of Figures

List of Tables

Abstract

There has been much excitement in the high energy physics community in recent years. The discovery of the Higgs boson at CERN confirmed all the predictions of the Standard Model, the theory that describes elementary particles and their interactions. Despite this tremendous success, other experimental results have been observed that cannot be described by the Standard Model. This inspires physicists around the world to search for evidence of physics beyond the Standard Model. One potential manifestation of this would be discrepancies between experimental results and theoretical predictions. This requires not only increasing the precision of existing measurements by increasing the luminosity of existing experiments, but also designing new experiments that allow the exploration of new physical phenomena that have not yet been detected.

The results of this work contribute to the various areas of the search for physics beyond the Standard Model. The presented $R(\Lambda_c) = \frac{\Lambda_b^0 \to \Lambda_c^+ \tau^- \overline{\nu}_\tau}{\Lambda_b^0 \to \Lambda_c^+ \mu^- \overline{\nu}_\mu}$ analysis is devoted to the study of lepton flavour universality in Λ_b decays using data collected in 2016 from the LHCb experiment. Anomalous deviations in semileptonic decays have been observed recently in several measurements, and are known as flavour anomalies. The measurement of the $R(\Lambda_c)$ ratio will help to solve this puzzle. The LHCb experiment is currently undergoing a major upgrade to improve the sensitivity of all measurements that contributed to the anomalies. The system for validation tests of readout chips for one of the detectors has been developed and the results of these tests are presented. Feasibility studies for a newly proposed SHiP experiment are also presented in this work, which would allow to open new regions for the search of new physics. The most dangerous background for the experiment comes from neutrino interactions. Its estimation and the possibilities of the experiment to suppress it are demonstrated. The second most dangerous background is from muons. The optimization of the magnetic system to eliminate this background is presented.

Overall the work in this thesis has contributed to a broad spectrum of how experimental particle physics is performed. The hope is that one of these avenues will lead to a potential discovery.

Introduction

Each scientific question that physicists around the world try to answer can be generalised into one, namely: ‘How do things work?’. For particle physicists, our desire is to know what the world is made of and what holds it together. For many decades now we have our handbook of fundamental physics, known as Standard Model (SM) of particle physics, which always seems provide satisfactory explanations for observations at the sub-atomic scale.

Physicists have been searching for New Physics (NP) signatures beyond the Standard Model in direct searches without success. The possibility that NP might be absent might have arisen, if it weren’t for the clear indications of phenomena which are not yet described by the SM. Such observations include baryogenesis, leptogenesis, the existence of dark matter, the fact that neutrinos have mass and oscillate from one type to another [1].

Although direct searches at high energy haven’t yielded evidence for TeV-scale new physics, indirect searches for particles which occur as virtual contributions in SM processes can probe larger energy scales for NP.

In recent years, several discrepancies between experimental measurements and SM predictions have arisen in indirect searches, known as the flavour anomalies. These anomalies have been observed in decays to different lepton flavours and have been seen by three different experiments: Belle, BaBar and LHCb. Despite the obvious excitement of the potentially first signs of NP, we cannot yet claim any discovery as we don't have precise enough measurements to reject the Standard Model at the 5σ discovery threshold. This requires us to explore other processes to provide independent measurements to help clarify the situation.

Another way to observe the potential NP discovery is to look at the regions which have not been yet investigated. While there are several experiments searching for NP in the high energy scale, the region of weakly interacting particles hasn't been yet fully covered. It motivates to construct new experiments with the cleanest possible environment to be able to observe weakly interacting particles.

The aim of this thesis was to study several different possible ways to discover new physics at collider and fixed-target experiments, analysing already collected data and developing new strategies and techniques that may give us more answers. The first chapter will introduce the current knowledge of the SM together with its inconsistencies, along with possible theoretical explanations. The second chapter will describe tests performed of new readout chips for the Upstream Tracker (UT) to be used in the upgrade of the LHCb experiment. The third chapter will show studies of the semitauonic decay $\Lambda_b^0 \to \Lambda_c^+ \tau^- \overline{\nu}_\tau$ with LHCb data that will contribute to solving the $R(D^*)$ mystery. The fourth chapter presents a new proposed experiment, SHiP, that can reveal new physics particles in the weakly interacting region.

Chapter 1

Theoretical motivation

1.1 Standard Model of particle physics

The most successful theory that describes subatomic particles and their interactions was developed in the early 1970s and is known as the Standard Model (SM) of particle physics [2]. Through the results from many experiments, it was established as a well-tested physics theory, and seems to be valid up to at least the Plank energy scale [3, 4].

According to the SM, matter and anti-matter are made of a set of elementary particles. These particles can be divided into two different classes, called quarks and leptons. There are three groups for each class, so-called generations. A generation is a set of one of each charge type of quark and lepton. Each generation is heavier than the previous one. Between generations, particles differ by their mass and flavour quantum number, but their electric and strong interactions are identical.

These particles interact between each other via four fundamental forces: the strong force, the weak force, the electromagnetic force and the gravitational force (not included in the SM). The interaction between matter happens through the exchange of force-carrier particles, so-called bosons, where the strong force is carried by the gluon, the electromagnetic one by the photon and the weak force is carried by the $W^{\pm}$ and Z^0 bosons. A schematic representation of the SM is depicted in Figure 1.1.

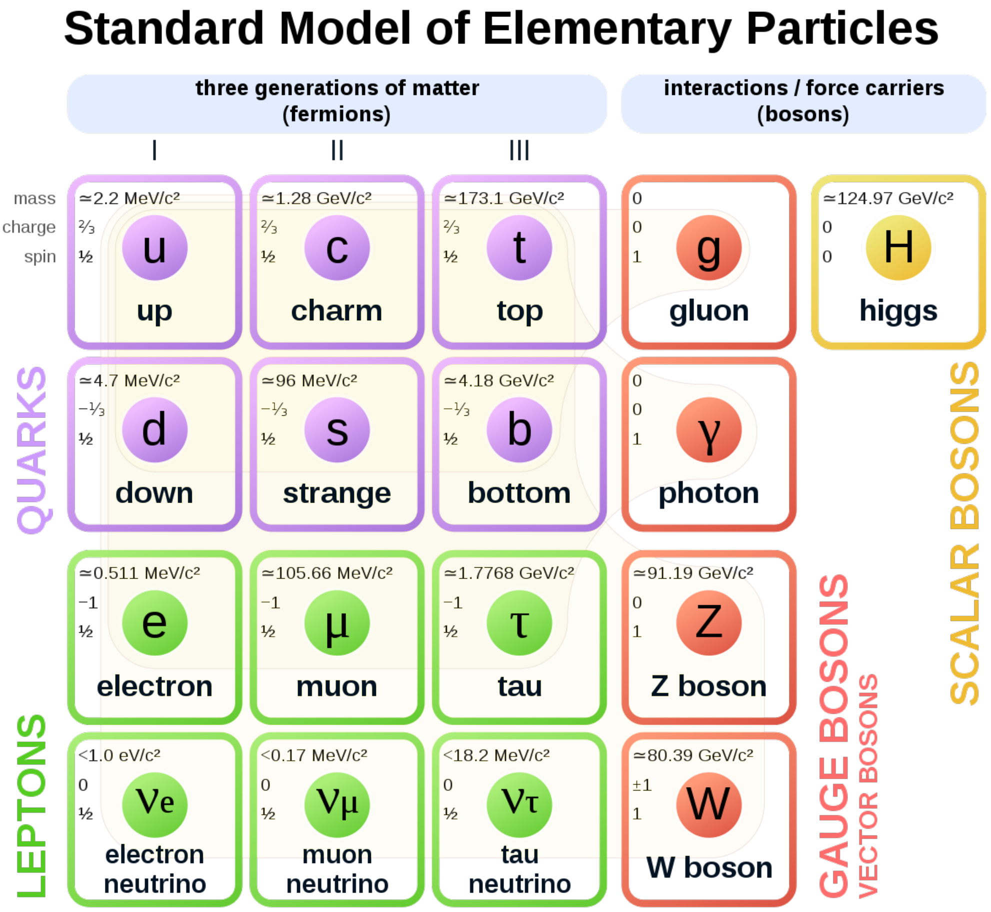

FIGURE 1.1: Representation of the Standard Model [5].

Mathematically, the SM is a quantum-field theory, which means that all particles are described as expectations of quantum fields that are defined at all points in spacetime. The SM is a gauge theory, i.e. its Lagrangian is invariant under local gauge transformations. The gauge group of the SM is

$$G = \mathrm{SU}(3) \times \mathrm{SU}(2) \times \mathrm{U}(1),$$

where $\mathrm{U}(1)$ acts on the boson of weak hypercharge and the Higgs field, $\mathrm{SU}(2)$ acts on the bosons of weak isospin and the Higgs field and $\mathrm{SU}(3)$

acts on the gluon field.

The Langrangian of the SM is made up of four different parts, each named after scientists:

$$\mathcal{L}_{\mathcal{SM}} = \mathcal{L}_{\mathcal{YM}} + \mathcal{L}_{\mathcal{WD}} + \mathcal{L}_{\mathcal{YU}} + \mathcal{L}_{\mathcal{H}},$$

$\mathcal{L}_{\mathcal{YM}}$ - the Yang-Mills part describes the low energy gauge groups of the SM, SU_3 for colour, SU_2 for weak isospean, and U_1 for hypercharge;

$\mathcal{L}_{\mathcal{WD}}$ - the Weyl-Dirac part describes the fermion fields and their gauge interactions;

$\mathcal{L}_{\mathcal{YU}}$ - the Yukawa part describes the Yukawa coupling;

$\mathcal{L}_{\mathcal{H}}$ - the Higgs part describes the Higgs mechanism that gives mass to the gauge bosons.

The masses and mixings of quarks arise from the Yukawa interactions with the Higgs condensate,

$$\mathcal{L}_{\mathcal{Y}} = -Y^d_{ij}\overline{Q}^I_{Li}\phi d^I_{Rj} - Y^u_{ij}\overline{Q}^I_{Li}\epsilon\phi^* u^I_{Rj} + h.c.,$$

where $Y^{u,d}$ are 3×3 complex matrices, ϕ is the Higgs field, i, j are generation labels, and ϵ is the 2×2 antisymmetric tensor. Q^I_L are left-handed quark doublets, and d^I_R, u^I_R are right-handed down and up-type quark singlets in the weak-eigenstate basis. When ϕ acquires a vacuum expectation value, $\langle\phi\rangle = (0, \frac{v}{\sqrt(2)})$, $\mathcal{L}_{\mathcal{Y}}$ yields mass terms for the quarks. The physical states are obtained by diagonalizing $Y^{u,d}$ by four unitray matrices, $V^{u,d}_{L,R}$ as $M^f_{diag} = V^f_L Y^f V^{f\dagger}(v/\sqrt(2))$, $f = u, d$. As a result, the charged-current $W^{\pm}$ interactions couple to the physical u_{Lj} and d_{Lk}

quarks with couplings given by

$$\frac{-g}{\sqrt(2)}(\overline{u}_L,\overline{c}_L,\overline{t}_L)\gamma^\mu W_\mu^+ V_{CKM}\begin{pmatrix} d_L \\ s_L \\ b_L \end{pmatrix} + h.c., V_{CKM} \equiv V_L^u V_L^{d\dagger} = \begin{pmatrix} V_{ud} & V_{us} & V_{ub} \\ V_{cd} & V_{cs} & V_{cb} \\ V_{td} & V_{ts} & V_{tb} \end{pmatrix}$$

The Cabibbo-Kobayashi-Maskawa (CKM) matrix, V_{CKM}, is a 3×3 unitary matrix [6]. The CKM matrix describes the probability of a transition from one quark to another quark.

One of the features of the SM is that the three leptons (the electron, muon and tau lepton) are identical apart from their different masses, meaning that the electroweak gauge bosons couple with equal strength to each generation of leptons. This attribute of the SM is known as Lepton Flavour Universality (LFU).

1.2 Deviations from the Standard Model

Even though many predictions of the SM have been experimentally confirmed, there are some experimental observations which cannot be explained by the SM.

- The presence of neutrino masses:

> There are three different types of neutrinos described in the SM, which do not have mass according to it. Nevertheless, it was found that neutrinos can oscillate and change flavour, transforming from the one type to another. This requires that neutrinos are not massless [7]. The neutrino mass term can be added to the SM, however it requires to have another heavier neutrino.

- Dark matter:

  The existence of dark matter was found in rotation curves of galaxies similar to the Milky Way. The further an object is from the centre, the slower it must travel in orbit. However, most of spiral galaxies show flat rotation curves out, where no more stars are visible. Hence, the gravitational mass is more than ten times more massive than the luminous mass [8].

- Matter and antimatter difference:

  According to current modelling, when the universe was formed in the Big Bang, matter and antimatter would have been produced in equal parts. Normally, when matter and antimatter meet, they annihilate one another. Nevertheless, now we exist in a world where matter dominates over the antimatter. The CKM matrix explains less than 10^7 of the baryon asymmetry in the universe [9].

- Dark energy:

  Most physics theories predicted that the expansion of our universe should have started to decrease after the Big Bang. However, experimental measurements have shown that the expansion of the universe is accelerating instead. The force responsible for this was named dark energy [10].

- No gravity:

  As was mentioned before, one out of four fundamental forces is the gravitational force. However, the SM doesn't account for it. Gravity does not have any impact on the subatomic interactions within the SM and is not explained by the SM.

1.3 Flavour anomalies

Over the last few years, several discrepancies in B meson decays to different lepton flavours were observed by various experiments. This violation of LFU could indicate the existence of new particles which are not included in the SM.

These discrepancies were observed in $B \to D^{(*)} l\nu$ decays by BaBar [11], Belle [12] and LHCb [13] experiments [14–19]. The central values of all measurements are above the SM expectation for the lepton universality ratio,

$$R(D^{(*)}) = \frac{\mathcal{B}(B \to D^{(*)}\tau\nu)}{\mathcal{B}(B \to D^{(*)}\ell\nu)},$$

where $\ell = \mu, e$ and $\mathcal{B}$ denotes the corresponding branching fraction. The SM prediction is determined using a combination of lattice quantum chromodynamics (QCD) and experimental data [20].

The combination of experimental results and the most recent SM predictions are depicted in Figure 1.2. The individual measurements are shown as well, with measurements of $R(D^*)$ shown as horizontal bands and measurements of both $R(D)$ and $R(D^*)$ shown as ellipses. The world average deviates from the SM prediction by 3 standard deviations.

An interesting feature of this discrepancy is that it arises from a combination of e^+e^- and collider experiments. These experiments have different experimental environment and hence different systematic uncertainties. More details on the different $R(D^{(*)})$ measurements are given in Section 3.1.1

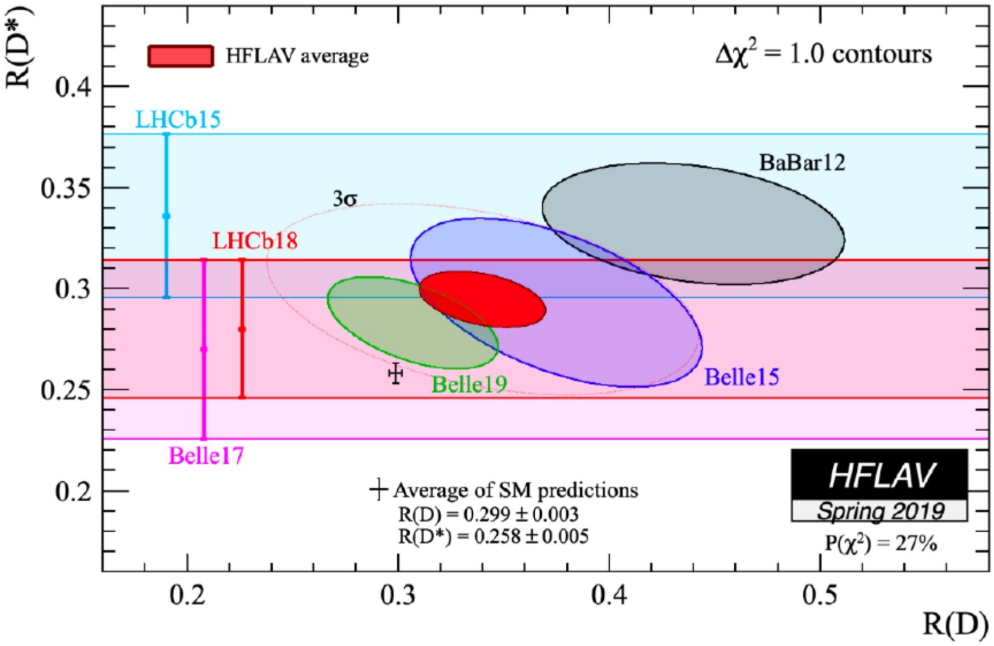

FIGURE 1.2: Measurements of the lepton universality ratios $R(D^*)$ and $R(D)$ for three experiments, the Belle, BaBar and LHCb detectors [21].

The decay of the type $b \to c\ell\nu_\ell$ is called Flavour-Changing Charged-Current (FCCC) transition and it can be described through an effective Hamiltonian:

$$\mathcal{H}_{eff} = \frac{4 \cdot G_F}{\sqrt{2}} \cdot V_{cb} \cdot \sum_i \mathcal{C}_i \mathcal{O}_i,$$

where

- G_F is Fermi constant.
- V_{cb} is the Cabbibo-Kobayashi-Maskawa (CKM) matrix element.
- $\mathcal{C}_i$ are Wilson coefficients, which encode the short-distance interactions associated to a particular operator, i.
- $\mathcal{O}_i$ are operators containing the fields propagating over distances larger than the one associated with the arbitrary renormalization scale μ. All effects of strong interactions above the μ scale are contained in the Wilson coefficient.

The production of the lepton pair goes via a $W^{\pm}$ boson exchange and due to the insensitivity of leptons to the strong interaction it is possible to factorise the amplitude into a leptonic and a hadronic parts. The form factors are used to describe the hadronisation of quarks and gluons. The difference in decay rates for the τ lepton and e-μ leptons is proportional to the mass of the τ lepton, therefore ratios of decays to different modes will involve specific ratios of form factors. The difference between the muon (electron) and tau invariant masses therefore explains the fact that the SM predictions for $R(D^{*})$ is not equal to 1. The larger tau mass leads to a reduced phase-space available to the tauonic decay, and this decay having a greater sensitivity to a helicity-suppressed form-factor [22].

Hints of violation of LFU have also been seen in the measurement of the observables $R(K)$ and $R(K^{*})$:

$$R(K^{(*)}) = \frac{\mathcal{B}(B \to K^{(*)}\mu^{+}\mu^{-})}{\mathcal{B}(B \to K^{(*)}e^{+}e^{-})}$$

These observables are defined as the ratio of the branching fractions of B mesons into $K^{(*)}$ mesons involving electron or muon pairs. The SM tells us that this ratio must be equal to 1, while the LHCb result indicates a deficit compared to the SM prediction.

The result for $R(K)$ was presented only in the dilepton invariant mass squared $q^{2} = [1.1, 6]$ GeV$^{2}/c^{4}$ [23–25], $R(K^{*})$ has been measured in two bins, $q^{2} = [0.045, 1.1]$ GeV$^{2}/c^{4}$, and $q^{2} = [1.1, 6]$ GeV$^{2}/c^{4}$ [26]. The deviations from the SM in the individual ratios are only at the level of $2.2\sigma - 3.1\sigma$, however the combined deviation, depending on how the combination is performed, reaches up to 4σ [27, 28].

The $R(K)^{*}$ observable represents a different class of decays in comparison to $R(D^{*})$, namely Flavour-Changing Neutral-Current (FCNC), where

b hadron decays with a loop-level transition of the type $b \to s\ell^+\ell^-$. In this case, the effective Hamiltonian takes the form:

$$\mathcal{H}_{eff} = -\frac{4 \cdot G_F}{\sqrt{2}} \cdot V_{tb}V_{ts}^{*} \cdot \sum_i \mathcal{C}_i \mathcal{O}_i,$$

where two CKM matrix elements are involved due to the quark runnig through the loop. These decays are suppressed compared to the more frequent FCCC decays and provide an increased sensitivity to the possible existence of new physics. Sensitive probes of FCNC decays are ratios of the branching fractions between final states with electrons and muons. In contrast to FCCC decays, both lepton masses can be neglected over most of the phase space.

1.4 Hidden sector New Physics models

The cause for SM failures can be that it does not yet include some new particles, which can be heavy or do not interact directly with the SM sector. Particles that interact weakly are "hiding" from us, therefore, they are called Hidden Sector (HS) particles. Nevertheless, they are potentially accessible through light particles which are coupled to SM particles via renormalisable interactions with small dimensionless coupling constants, so called portals. Therefore, the SM Lagrangian can be extended as follows:

$$\mathcal{L} = \mathcal{L}_{\mathcal{SM}} + \mathcal{L}_{\mathcal{PORTAL}} + \mathcal{L}_{\mathcal{HS}}$$

According to their mathematical form renormalisable portals can be classified into vector, scalar, fermion portals and the pseudo-scalar axion-like particle portal [29].

1.4.1 Axion-like particles

Axion-like particles (ALPs) are pseudo nambu–goldstone bosons of spontaneously broken global symmetries in high-energy extensions of the SM [30]. ALP can be non-thermal candidates for dark matter or mediators to a hidden sector. Axion-like particles are a generalisation of QCD axions, but can differ in mass.

ALP are interesting, as they can mediate the interactions between the dark sector and SM states and allow for additional annihilation channels relevant for the thermal freeze-out of dark matter. The ALP can couple to the SM via its coupling to two gauge bosons and through those to SM fermions ($pp \to A + X, A \longrightarrow \gamma\gamma$). In this case, SM Lagrangian will be extended to

$$\mathcal{L} = \mathcal{L}_{\mathcal{SM}} + \frac{1}{2}\partial^{\mu}a\partial_{\mu}a - \frac{1}{2}m_a^2a^2 - \frac{1}{4}g_{a\gamma}a\tilde{F}_{\mu\nu}F^{\mu\nu},$$

where $g_{a\gamma}$ denotes the photon-ALP coupling. ALPs are expected to be produced in the proton elastic scattering on the nucleus. Relevant production and decay mechanisms are shown in Figure 1.3. The decay of ALP is possible via pair-production of gauge bosons, such as two photons, or of SM fermions, such as lepton-pair.

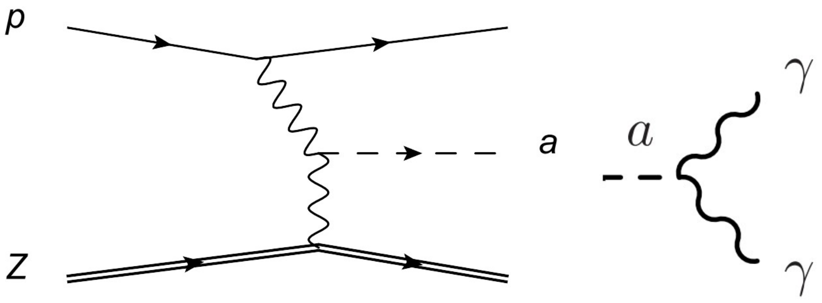

FIGURE 1.3: Feynman diagrams showing relevant ALP production and decay [31].

1.4.2 Vector portal

Another option to extend the SM with the HS is to introduce an additional U(1) gauge group to the SM [32]:

$$G = \mathrm{SU}(3) \times \mathrm{SU}(2) \times [\mathrm{U}(1)]^n$$

One way a new vector particle can couple to the SM is through kinetic mixing ϵ with the photon, so that none of the SM fields needs to be charged under the new gauge groups.

The gauge boson of the new gauge group is called the dark photon and denoted, as A' with a new field strength tensor F'. In this case, the SM Lagrangian will be extended to

$$L = L_{SM} - \frac{1}{4} F'_{\mu\nu} F'^{\mu\nu} + \frac{\epsilon}{2} F'_{\mu\nu} F^{\mu\nu} + \frac{m^2_{\gamma'}}{2} A'_{\mu} A'^{\mu},$$

where A' is a dark photon field.

Dark photons are expected to be produced in meson decay, proton and parton bremsstrahlung through the production of high-energy virtual photons. The decay of dark photons is possible via pair-production to hidden-sector particles or to SM charged particles (i.e., lepton pairs). Relevant production and decay mechanisms are shown in Figure 1.4. The dark photon is also the perfect candidate for a light dark-matter mediator [33].

1.4.3 Scalar portal

Many NP models propose to extend the SM with another light scalar or pseudoscalar particles [34–37], as the Higgs field is the simplest realisation of mass generation for gauge fields and fermions of the SM [38].

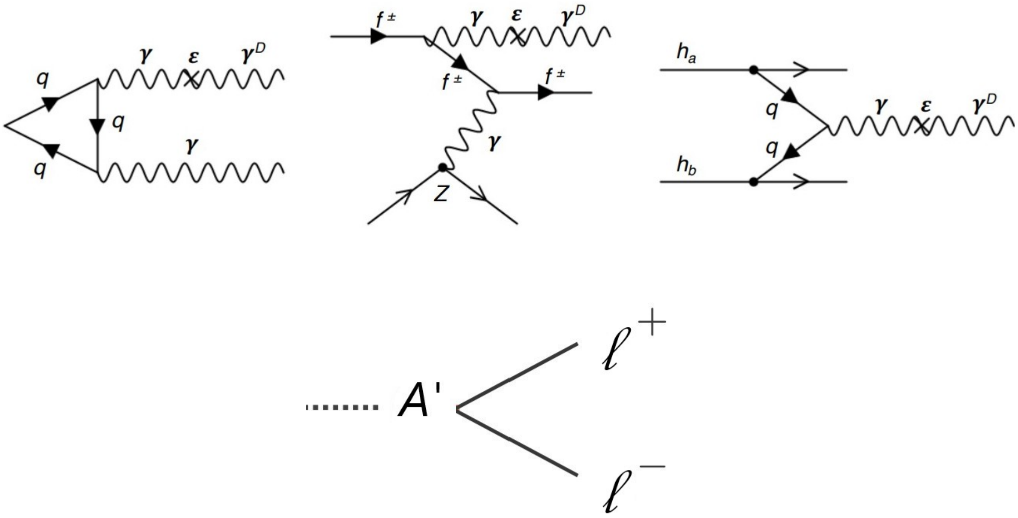

FIGURE 1.4: Feynman diagrams for the dark photon production and decay. The top left picture shows a production through secondary meson decays, the top middle through proton bremsstrahlung and top right through parton bremsstrahlung [29].

The SM can be extended with a scalar portal by adding an additional interaction term $(H^\dagger H)S$, where S is a new singlet scalar coupling to the square of the Higgs field H. In this case, the SM Lagrangian will be extended to

$$\mathcal{L} = \mathcal{L}_{\mathcal{SM}} + \frac{1}{2}\partial_\mu S \partial^\mu S + (\alpha_1 S + \alpha_1 S^2)(H^\dagger H) + \lambda_2 S^2 + \lambda_3 S^3 + \lambda_4 S^4,$$

A sample of dark matter models based on the Higgs portal can be in the MeV-to-GeV range and interact only through their couplings with the Higgs sector [35]. Scalars can be produced in B meson and kaon decays and they can be detected by their decays into observable final states, such as $\gamma\gamma$, e^+e^-, $\mu^+\mu^-$, $\pi\pi$, KK. Relevant production and decay mechanisms are shown in Figure 1.5.

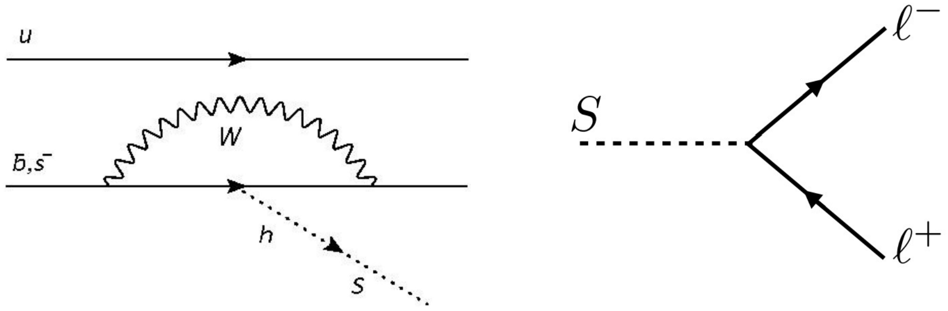

FIGURE 1.5: Feynman diagrams for the scalar production in meson decays [39] and its decay to a lepton pair [29].

1.4.4 Fermion portal

An example of the fermion portal is represented via the neutrino minimal Standard Model. This theory predicts the existence of three heavy neutral leptons (HNL) [40].

In this case, we extend the SM fermion sector by three right-handed (Majorana) leptons N_1, N_2, N_3, which makes the leptonic sector similar to the quark sector. An extended SM is depicted in Figure 1.6.

The lightest singlet fermion N_1 mixes very weakly with the other leptons, being sufficiently stable to be a dark matter candidate. The requirement of N_1 to be a dark matter candidate requires $N_{2,3}$ to be nearly degenerate in mass, which provides sufficient CP violation to explain the baryon asymmetry in the Universe [41].

The tiny neutrino mass can be explained by mixing a small mass neutrino with a very heavy Majorana neutrino. The corresponding mass matrix for the right-handed neutrino is

$$M = \begin{pmatrix} 0 & m_D \\ m_D & m_M \end{pmatrix},$$

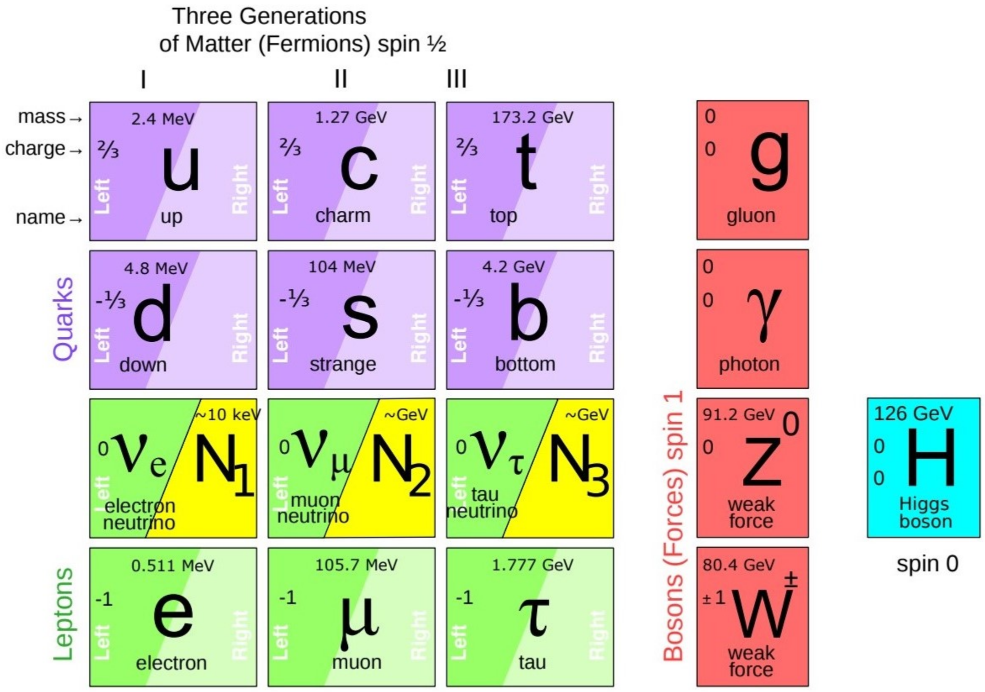

FIGURE 1.6: Particle content of the SM and its minimal extension in the neutrino sector [29].

where m_D is the Dirac mass of electroweak scale, and m_M is the Majorana mass of the Grand Unified Theory (GUT) scale. From here we can achieve two eigenvalues $m_\nu \approx m_M$ and $m_\nu \approx \frac{m_D^2}{m_M}$, where one solution represents the observed neutrinos, while another one indicates the existence of a very heavy neutrino which still needs to be discovered. The fact of this HNL being heavy explains the zero mass of SM neutrinos.

The typical value of the Dirac mass term is $m_D \approx Y_{I\alpha} v$, where v is the vacuum expectation value of the Higgs field and $Y_{I\alpha}$ the Yukawa couplings.

HNL can be produced in the weak decay of heavy mesons and decay to SM particles. The mixing angles for them are small; therefore, HNL are much longer-lived than weakly decaying SM particles of similar mass. For the HNL masses below the charm threshold, the most relevant production and decays mechanisms are shown in Fig 1.7.

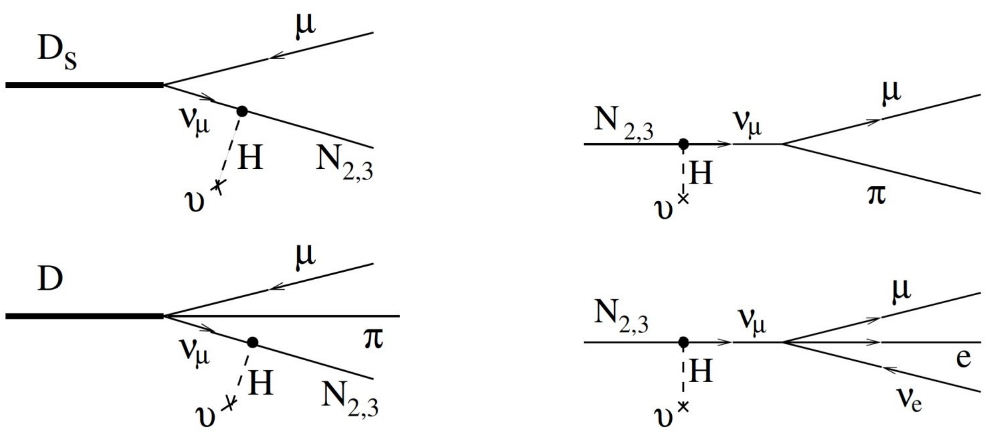

FIGURE 1.7: Feynman diagrams for the HNL production and decay [29].

1.4.5 Lepton Flavour Violating portal

Neutrino oscillation is the first evidence of lepton flavour violation (LFV) in the neutral sector. A consequence of this is the presence of neutrino masses and the implication that lepton flavour might not be conserved in the charged sector, either. Therefore, LFV in the charged sector would be an unambiguous signal of physics beyond the Standard Model.

In the SM, charged LFV (CLFV) branching fractions are heavily suppressed. However, in new physics scenarios, such as Z', SO(10) supersymmetric or Type-II Seesaw models with an extended Higgs sector, predicted branching fractions can be of the order of up to $10^{-10} - 10^{-8}$ [42, 43], opening the possibility of observing such effects. Therefore, for instance, observing $\tau \to 3\mu$ decays would provide immediate proof of physics beyond the SM.

In the case of Type-III Seesaw model, the CLFV decay to three leptons can occur at tree level while the radiative decays proceed only through loops, which makes the trilepton decay the dominant one [43].

1.5 Models explaining anomalies in semileptonic B-decays

The LFU violation in $b \to s\ell^+\ell^-$ and $b \to c\ell\nu_\ell$ transitions can be explained via new physics in two ways: through general effective field theory approach or through specific new physics models. Effective field theory approach is a model-independent method where the values of the short-distant Wilson coefficients are determined from data and compared to the SM ones. In this way, various new physics scenarios can be defined, as a contribution to Wilson coefficients $\mathcal{C}_i = \mathcal{C}_i^{SM} + \mathcal{C}_i^{NP}$ [44].

In case of the $b \to c\ell\nu_\ell$ transitions, most of the effective field theory analyses assume to have new physics contributions only in the $b \to c\tau\nu_\tau$ decays, as there was no signs of violation of LFU in electronic and muonic decay states. The best scenario is left-handed contributions to vector and axial operators, i.e. additional new physics contribution to the Wilson coefficient of the SM operator $\mathcal{O}_{V_\tau} = (\bar{c}\gamma_\mu P_L b)(\bar{\tau}\gamma^\mu P_L \nu)$. Right-handed currents is an alternative approach with having new physics contributions to Wilson coefficient $\mathcal{O}_{V_\tau} = (\bar{c}\gamma_\mu P_R b)(\bar{\tau}\gamma^\mu P_L \nu)$. But it cannot explain fully LFU violation due to constraints from the total lifetime of the B_c meson [45]. The constraint is derived from the requirement that the rate of $B_c \to \tau\nu_\tau$ should not exceed the fraction of the total width that is allowed by the calculation of the lifetime [46]. The measurement of the tauonic decay branching fraction of B_c hasn't been done due to inability to reconstruct its decay vertex. However, it can be extracted from the experimentally measured B_c lifetime τ_{B_c}. Knowing that the total decay width is inversely proportional to the particle lifetime ($\Gamma_{B_c} = \frac{1}{\tau_{B_c}}$) and distributed among different modes in the following proportion:
$\bar{c} \to \bar{s}\,\bar{u}\,d$ (47 %),

$\bar{c} \to \bar{s}\, \ell\, \bar{\nu}$ (17 %),

$b \to u\, \bar{u}\, d$ (16 %),

$b \to c\, \ell\, \bar{\nu}$ (8 %),

$b \to c\, \bar{c}\, s$ (7 %)

only less than 5% of decays can be through the tauonic mode.

The LFU violation in the $b \to c\ell\nu_\ell$ transition requires a new physics contribution of $O(10\%)$ of the tree-level SM contribution. Therefore, new particles added to the SM for explaining $R(D^{(*)})$ anomaly cannot be very heavy and must have sizeable coupling. The $b \to s\ell^+\ell^-$ transition can be explained with a new physics contribution of $\approx 25\%$ of the loop and a CKM-suppressed SM contribution. That means that new physics should couple strongly to the third generation, moderately to the second and almost do not couple to the first generation. At the same time, new physics shouldn't violating lepton flavour for process that have been already measured.

Most of the proposed models to explain flavour anomalies introduce a new Lorentz-scalar or Lorentz-vector with the following transformation properties under the SM gauge group [47]:

- $\mathrm{SU}(3)_C$: a singlet or a triplet;
- $\mathrm{SU}(2)_L$: a singlet or a doublet or a triplet;

One of the natural possibilities to extend the SM is a color-singlet, weak-triplet vector field, i.e. a heavier replica of the $W^\pm$,Z^0 bosons called W' and Z'. Models with W' gauge bosons always involve Z' bosons due to $\mathrm{SU}(2)_L$ gauge invariance, however the total decay width of Z' is required to be very large to be consistent with existing $\tau^+\tau^-$ resonance searches at LHC [48].

There are multiple models for colour-triplet scalars or vectors. Colour triplets are known as leptoquarks (LQ), states coupled to a quark and a lepton. Scalar leptoquarks can be a good explanation for both, FCCC and FCNC, anomalies if right-handed neutrinos are involved in the model. The vector leptoquark singlet gives a particularly good global fit to data.

Another type of models propose having heavy colourless scalars (charged or neutral heavy Higgs-like bosons). An extended Higgs sector with a charged Higgs is a good candidate because the coupling to the lepton is proportional to the mass of the lepton. However, it is disfavoured by constraints [45] from limits on the branching ratio of $B_c \to \tau\nu_\tau$.

The Feyman diagrams of these transitions are depicted in Figure 1.8.

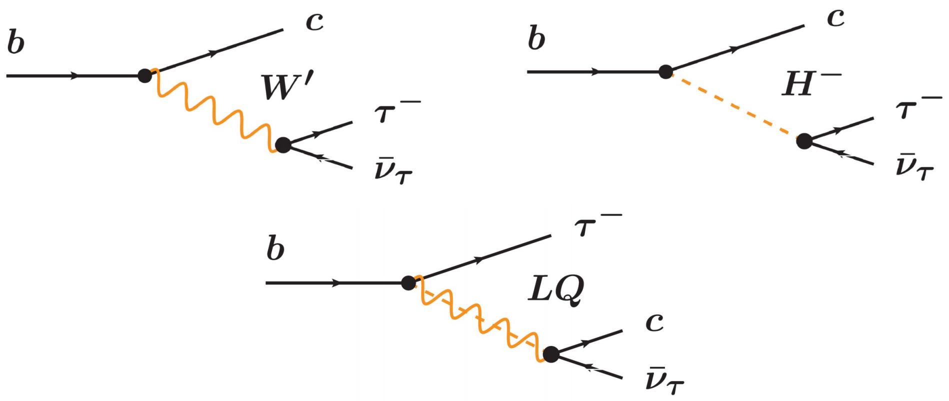

FIGURE 1.8: Feynman diagrams for W' (top left), charged Higgs (top right) and leptoquark (bottom) contributions to $b \to c\tau\nu$ [49].

Chapter 2

Wafer testing of the SALT128 integrated circuit chip for the LHCb upgrade

2.1 SALT128 - the new readout Silicon ASIC for LHCb Tracking

2.1.1 The LHCb experiment and motivations for an upgrade

The Large Hadron Collider Beauty (LHCb) [50, 51] experiment is one of the four main experiments at the Large Hadron Collider (LHC). Although, LHCb was initially designed to measure CP violation and rare decays of b and c flavoured hadrons with high precision, it has expanded its programme to a wide range of particle physics topics. The LHCb experiment benefits from the very large b and c flavoured hadrons production cross sections at the LHC.

The LHCb detector is a single-arm forward spectrometer covering the forward pseudorapidity region $2 < \eta < 5$. The layout of the detector is shown in Figure 2.1. The right-handed coordinate system adopted has the z-axis along the beam, and the y-axis along the vertical. The LHCb detector consists of several specialised sub-detectors to measure the properties and identify decay particles. The track reconstruction system incorporates a vertex detector, called the Vertex Locator (VELO) that is surrounding the collision region, and planar tracking stations. The tracking stations include the Tracker Turicensis (TT) located upstream of the dipole magnet, and three tracking stations (T1, T2, T3) located downstream of the magnet. The purpose of the VELO is that it can locate precisely the collision point and decay vertices of b hadrons. This is essential to separate the b-hadron decays from the prompt tracks and to measure charm and beauty hadron lifetimes. The TT is followed by the magnet whose used to determine the charge of the track and estimate its momentum based on the curvature. The polarity of the magnet is regularly flipped during data-taking to reduce detection asymmetries. The charged particle identification (PID) is performed by two Ring Imaging Cherenkov detectors (RICH1 and RICH2), in addition to the information from the calorimeters and the muon system. The calorimeter system consists of an electromagnetic calorimeter (ECAL) with Preshower (PS) and Scintillator Pad Detector (SPD) and a hadronic calorimeter (HCAL). The calorimeters are used in the hardware trigger and for the reconstruction of photons and electrons. The HCAL is followed by the four muon stations (M2,M3,M4,M5) of the muon system, while the first station is located behind the ECAL.

The LHCb detector's upgrade is needed to deal with higher rates for Run 3 and Run 4 of the LHC, where Run 3 is expected to begin at the start of March 2022. The upcoming upgrade aims to collect 50 fb^{-1} in Run 3 and Run 4 comparing to 9 fb^{-1} of data that have been collected in

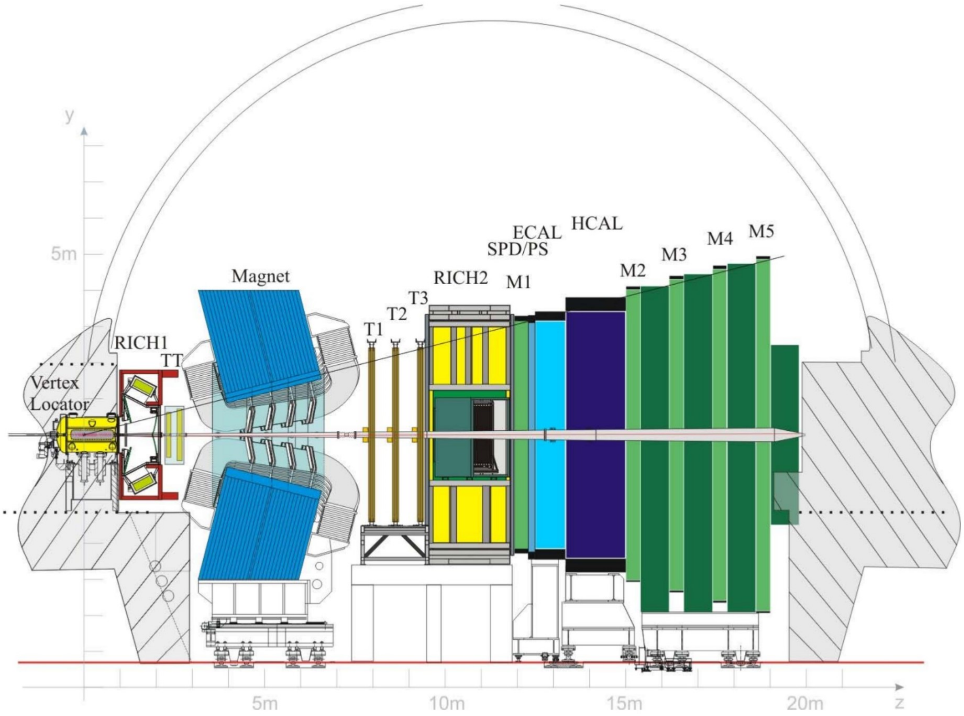

FIGURE 2.1: Schematic view of the LHCb detector [50].

Run 1 and Run 2 [52].

This upgrade is strongly motivated by the need to increase the signal yields in order to improve precision. The increase in data will allow to probe NP not only within the field of flavour physics but also in other physics topics for which the LHCb acceptance in the forward region is particularly interesting [53]. The main goal of the upgrade is to run at a higher luminosity while maintaining or increasing the efficiency of selecting signal candidates. Here the original LHCb detector is potentially limited by readout electronics and data acquisition architecture. This major modification will involve the Data Acquisition (DAQ) that will need to deal with a rate corresponding to the 40 MHz bunch-crossing frequency, instead of 1 MHz which the case in Run 1 and Run 2 and the trigger system which will be fully switched to a software. This necessitates a complete replacement of all front-end electronics and those detector components with embedded electronics, in particular the tracking sub-detector that will be completely re-built.

2.1.2 Overview of the LHCb upgrade

The main challenge for the LHCb upgrade is to introduce the read-out system for all subdetectors that will be able to handle the bunch-crossing rate of 40 MHz, while during the Run 2 rates were cut by the hardware trigger to a level below 1.1 MHz [54]. Improved radiation hardness and finer granularity of detectors is another crucial requirement to deal with the higher density of charged particles. A schematic view of the upgraded LHCb detector is shown in Fig. 2.2.

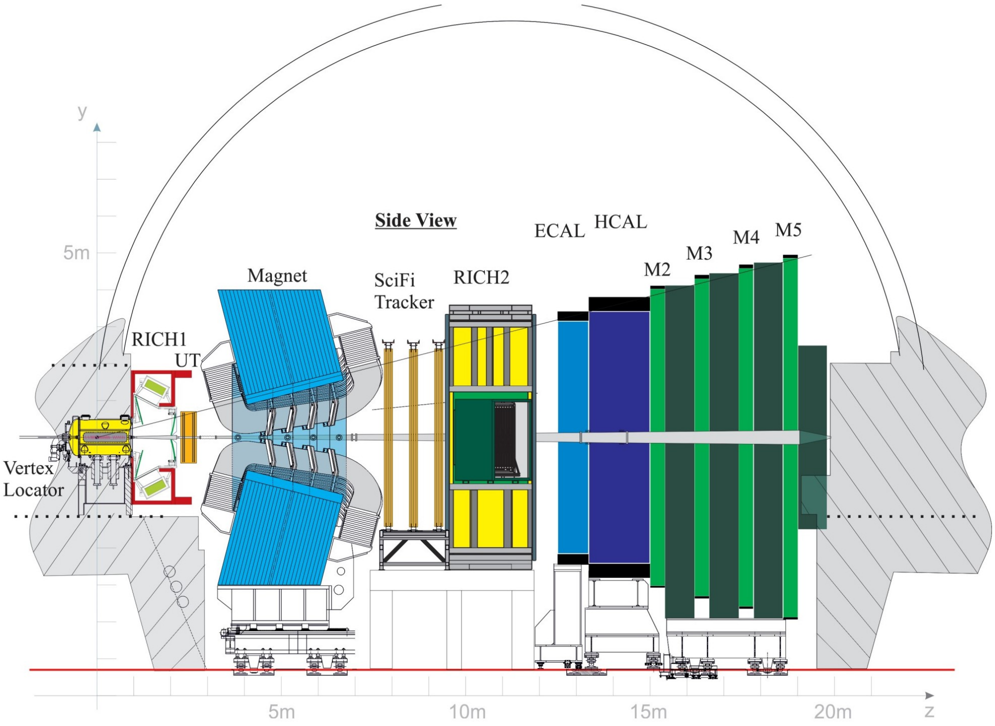

FIGURE 2.2: Layout of the LHCb detector after the upgrade. The beam is along the z axis [52].

The closest sub-detector to the interaction point which will be upgraded is the VELO. The VELO measures the vertex positions of the primary proton-proton collision and the b-hadron decay. The main feature of this sub-detector is that it must have a high granularity and be positioned close to the collision point to distinguish short lived b hadrons while avoiding the damage from the LHC proton beams. The upgraded VELO detector [55] will adopt pixels instead of microstrips, which will have a finer granularity. It will also be positioned closer to the beam, with its sensitive area starting at a distance of 5.1 mm from the beam axis. This will allow improvement of the reconstruction of vertices while avoiding the high occupancy expected in the region closest to the beam. The upgraded VELO detector will consist of 41 million 55 μm wide and 55 μm high pixels, which will be read out at the 40 MHz bunch-crossing rate by the custom-built VeloPix front end ASIC [56]. In order to cool the sensors and decrease the effects of radiation damage, cope with the power dissipation of the ASIC, and respect the material budget constraints of the detector, the cooling system will be embedded in the modules. This will be done by means of evaporative CO_2 circulating through miniature channels into silicon substrates. The layout of a module of the upgraded VELO detector is shown in 2.3. The VELO will be followed by the Upstream Tracker (UT) which will be discussed in detail in the next chapter.

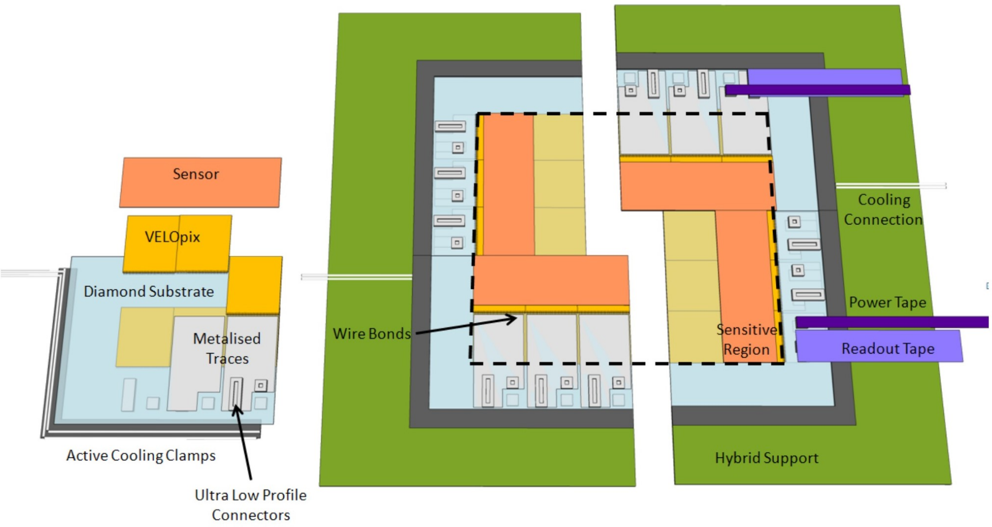

FIGURE 2.3: Layout of the VELO detector module for the upgrade [57].

The rest of the tracking system which was originally consisted of three tracking stations ("T1 - T3") using straw-tube drift chambers with 5 mm cell diameter technology and silicon microstrips will be replaced by the Scintilating Fibre (SciFi) Tracker [58]. The SciFi will consist of three stations organised in four detection planes according to a (x,u,v,x) configuration where u and v are oriented ±5° with respect to the x and y axes. Each detection plane consists of twelve modules made of 8 fibre mats each containing six stacked layers of 250 μm scintillating fibres bonded to each other. A schematic view of the mat is shown in the Figure 2.4. Silicon photomultipliers (SiPMs) will be used to detect the scintillation light generated inside each fibre. Each mat will be equipped by 4 SiPMs with 128 individual channels each to readout the signal with the PACIFIC ASIC [59].

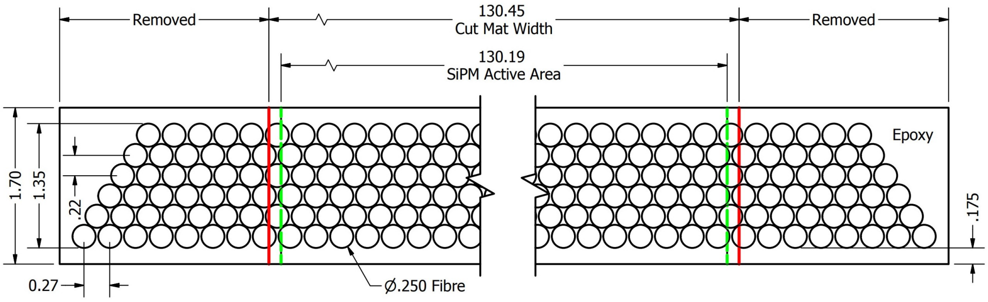

FIGURE 2.4: Schematic of the cross-section of a fibre mat [58].

The Ring-imaging Cherenkov subdetector (RICH) of LHCb has the task of identifying charged particles over the momentum range 1-150 GeV/c, within an angular acceptance of 10-300 milliradians. Particle identification is crucial to reduce background and to provide a tag of the b-quark flavour using the kaon from the other b-quark produced in an event. Currently the system consists of an upstream detector (RICH-1) and C_4F_{10} gas radiators, positioned directly behind the VELO, and a downstream detector (RICH-2) with a CF_4 gas radiator, located behind the magnet and the tracking system. The hybrid photodetectors will be replaced by commercial Multi-Anode Photo-Multiplier Tubes (MaPMTs) together with a new front-end electronics. In addition, the optics of the RICH-1 detector will be optimised to cope with the high occupancy in the innermost region.

Also the upgrade will affect the trigger system, which is going to be fully transferred to software. It will consist of a Low Level Trigger (LLT) and a High Level Trigger (HLT), where the LLT will perform filtering based on E_T and p_T of particles, while the HLT will process events passing the LLT and apply a procedure mirroring the one used in HLT2 during the Run 2. The LLT will deliver the rate of 15-30 MHz to the HLT which will give in turn an output rate of 20 kHz.

2.1.3 New Upstream Tracker for the LHCb upgrade

As was mentioned in the previous chapter, the LHCb detector needs to undergo a major upgrade, including the entire tracking system. Despite the fact that the tracker used in Run 1 and Run 2, called the Tracking Turicensis (TT), performed well it has to be replaced. The TT was not designed to be sufficiently radiation hard to survive the expected radiation damage and needs finer granularity, especially in the inner region of the detector. In addition, the Beetle [60] readout chip will not be able to handle the rate of 40 MHz which is expected for Run 3, while it cannot be replaced without damage, as it integrated in the mechanical structure of the detector modules. In order to address these issues, the TT will be replaced by the Upstream Tracker (UT) upstream of the magnet.

The UT will be a crucial element in track reconstruction. Although it is possible to reconstruct tracks using only long segments from the VELO and the downstream tracker, the track reconstruction efficiency is higher using information from UT [61]. In addition, mismatching lead to the reconstruction of false tracks, so-called ghosts. The requirement that extrapolated hits positions at the UT match real hits will reduce the ghost rate substantially [58]. The effect of it shown in the Figure 2.5.

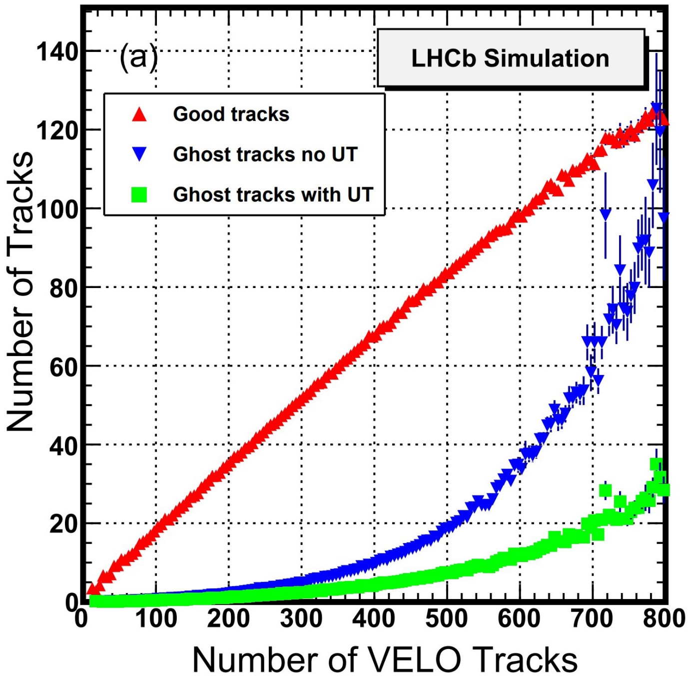

FIGURE 2.5: Simulation of the number of real reconstructed downstream tracks and ghost tracks as a function of the number of VELO tracks at a luminosity of $2 \cdot 10^{33}\text{cm}^{-2}\text{s}^{-1}$. The generated sample consists of events containing inclusive b-hadron decays at 14 TeV centre-of-mass energy. The ghosts are in two categories, one not requiring, and the other requiring a UT track match [58].

The UT will consist of four planar detection layers covering the full acceptance of the experiment. In total, the detector will use about 1000 silicon sensors where each sensor is directly connected to a hybrid that carries either 4 or 8 custom-made front-end readout chips (ASICs), which sample and digitize the detector signals, perform common-mode noise correction and zero-suppression algorithms, multiplex and send the data via copper traces to the periphery of the detector. The planes are constructed with vertical modules, called staves. These staves run vertically in Y direction, in order to measure the momentum of particles from the bending of their trajectory in the magnetic field. Therefore, the middle two planes, which are labelled U and V, are placed at an angle of ±5° to the vertical allowing to determine also a Y coordinate. The full detection coverage of the solid angle is provided by staggering of the staves in Z. Each plane also carries a circular hole in the centre for the beam-pipe keeping a good acceptance. A schematic view of the UT planes is shown in Figure 2.6.

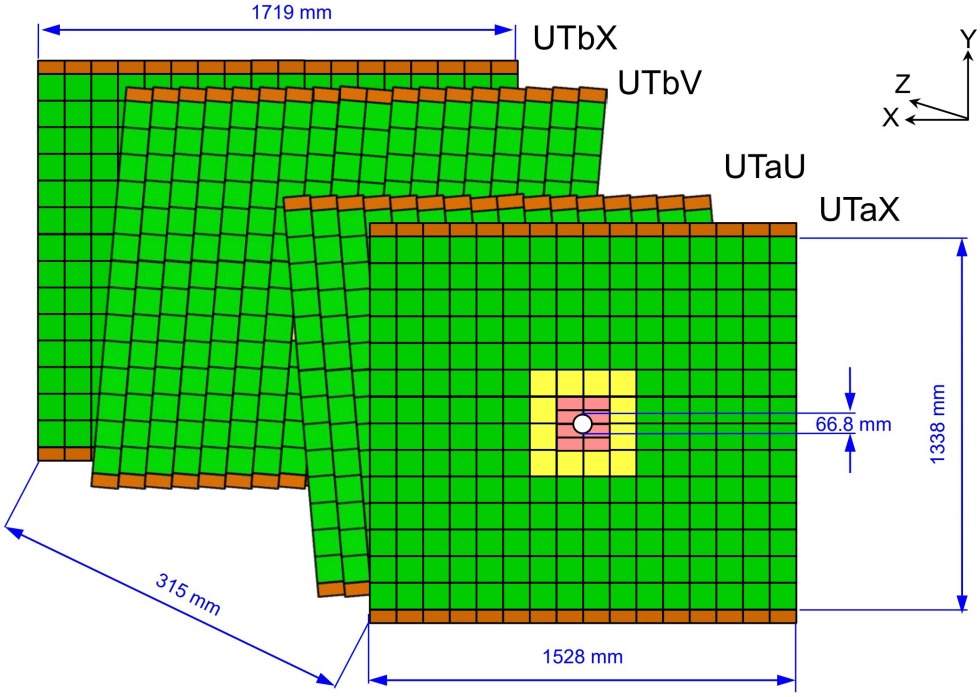

FIGURE 2.6: Overview of the UT geometry from simulations looking downstream. A colour coding indicates the different sensor geometries [58].

Each stave has a length of 130 cm and the width of a silicon sensor. The silicon strip sensors will have a pitch of 95 and 190 μm and two lengths of 5 and 10 cm. The staves consist of light-weight foam embedded between two sheets of carbon fibre. Embedded titanium cooling pipes with circulated innovative bi-phase CO_2 will be used for cooling of the silicon sensors and the front end electronics and keeping their temperature below -5°. Output signals and control signals, low-voltage power for the front-end chips and bias voltage for the silicon sensors are transported along the staves via kapton flex cables that are glued onto both at sides of the stave. Each of these cables carries up to 120 high-speed differential pairs with a total of 38.4 Gbps and 8 A of current to power up to 24 ASICs, while maintaining a minimal material budget. The stave structure is shown in Figure 2.7.

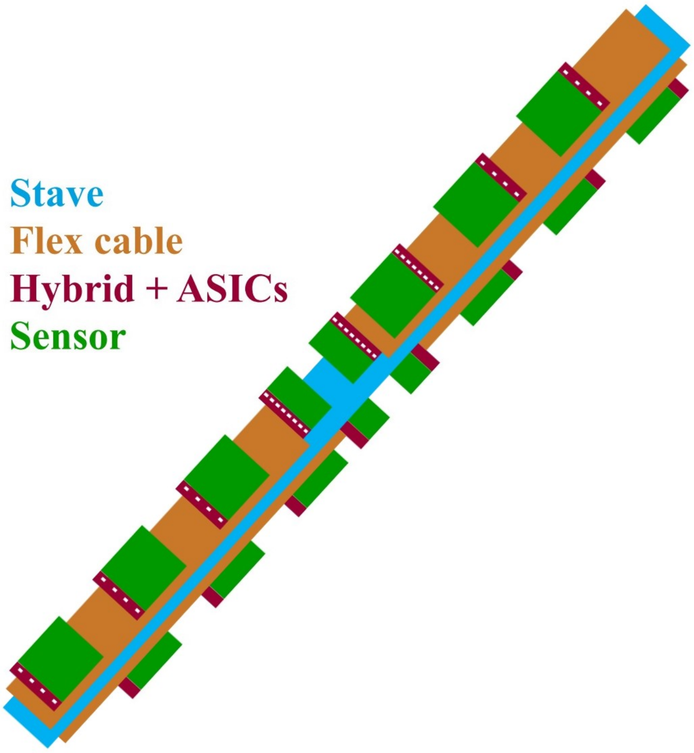

FIGURE 2.7: Overview of a UT stave [62].

2.1.4 The SALT128 ASIC

The harsh radiative environment and the high cross-section frequency rate puts large requirements on the read-out system. It necessitates the development of a special front-end read-out Application Specific Circuit (ASIC) for the purposes of transferring data out of the silicon micro-strip sensors of the UT at 40 MHz. The ASIC which is going to be used in the UT is known as the SALT128 chip, where 128 indicates the number of read-out channels. The chip is based on the radiation-hard TSMC

Complementary Metal Oxide Semiconductor (CMOS) 130 nm technology [63]. The main advantage of CMOS over NMOS and BIPOLAR technology is the much smaller power dissipation. A block diagram of the SALT128 chip is illustrated in Figure 2.8.

Each channel of the chip comprises an analogue block consisting of a charge sensitive preamplifier, a shaper, to support a fast signal with a peaking time of less than 25 ns and fast recovery to minimise the pile-up and spill-over into the next bunch crossing, and a single-ended-to-differential converter. The chip is designed to be able to read out both types of sensors, p^+ - on - n and n^+ - on - p. The differential analogue signal after being read goes to an Analogue to Digital Converter (ADC) implemented as a 6-bit fully differential Successive Approximation Register (SAR) operating at 40 Ms/s. After digitising the data is then sent to the digital signal processing block (DSP), which allows to filter noisy channels, performs pedestal subtraction, mean common mode subtraction, zero suppression and data compression. After the DSP the data, with added header information, are placed into a de-randomising buffer [64] and transmitted to the consecutive parts of the read out system using five serial links with SLVS standard at 320 MBit/s data rate. The ASIC is controlled via the LHCb common protocol consisting of two interfaces: the Timing and Fast Control (TFC) and the Experiment Control System (ECS) [65]. The TFC interface delivers the 40 MHz clock and other crucial information and commands, synchronised with the experiments clock, while the ECS serves to configure and monitor the ASIC and is realised through the Inter-Integrated Circuit (I^2C) interface.

The high bunch crossing rate of 40 MHz requires a charge preamplifier, and a fast shaper with a peaking time $T_{peak} = 25$ ns and fast recovery to minimise the pile-up and spill-over into the next bunch crossing.

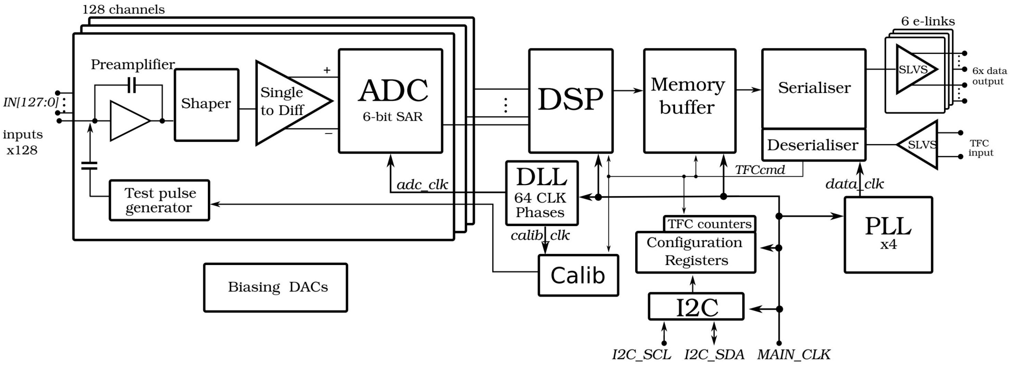

FIGURE 2.8: Block diagram of SALT128 [63].

2.2 Validation tests before the installation

2.2.1 A description of the test system

The Test Stand

All produced SALT128 chips needed to be tested before being integrated on hybrids in the UT. Chips are produced on wafers and these quality assurance tests are performed using a semi-automatic probe station (Figure 2.9) before the wafers are diced . Each wafer holds 467 chips and has a round shape with a diameter of 300 mm.

A wafer probe card is used to make electrical contact with the chip. Its purpose is to provide an electrical path between the test system and the circuits on the wafer, thereby permitting the testing and validation of the circuits at the wafer level. For our tests we used the cantilever probe card with 99 pads to probe specially manufactured by T.I.P.S. company (T.I.P.S. Messtechnik GmbH, Europastraße 5, A-9524 Villach, Austria). The probe card has an aluminium pad material which provides a good contact resistance with little to no probe cleaning.

This probe card is then connected to a DAQ system controlled by a PC which also controls power supplies and the movement of the probe station chuck. A calibration test pulse implemented inside SALT128 allows

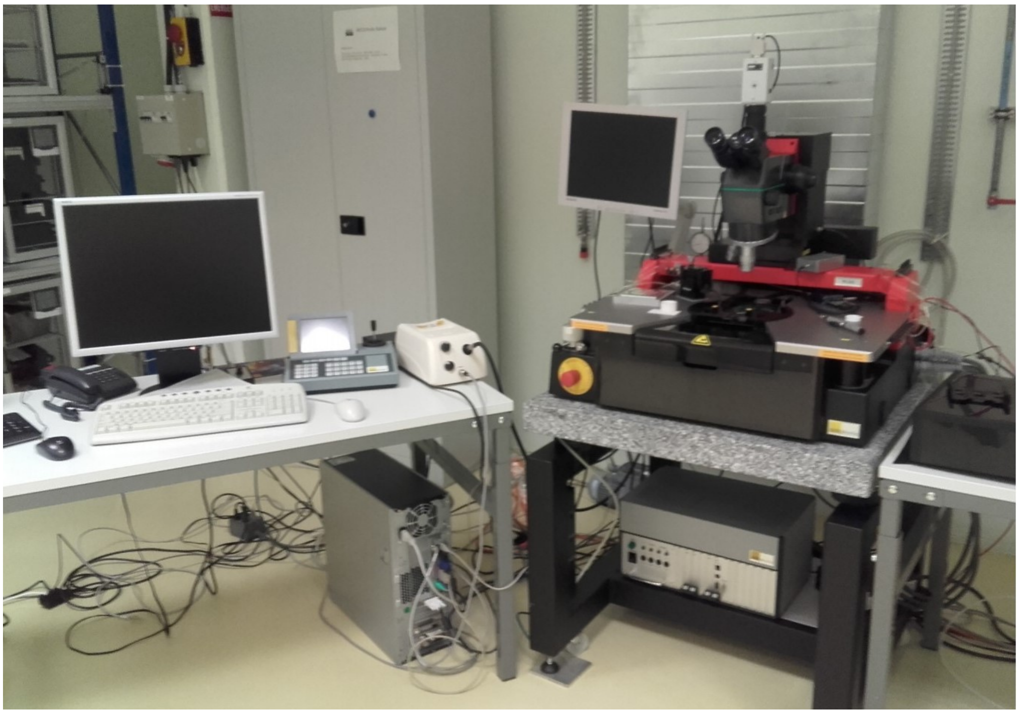

FIGURE 2.9: Semi-automatic probing station for testing silicon sensors at CERN which is used for the validation test.

the check of the whole processing chain in the chip without radiation or even sensor attached. The algorithm of the testing procedure is illustrated in Figure 2.10.

The DAQ System

System on chip as the control element

The Terasic Cyclone V SE System on Chip (SoC) Field Programmable Array (FPGA) was chosen as the skeleton for the data acquisition system for the set-up [66]. SoC is an integrated circuit that integrates all components of a electronic system. Cyclone SoC integrates an ARM-based hard processor system (HPS) consisting of processor, peripherals, and memory interfaces, with the FPGA fabric using a high-bandwidth interconnect backbone. This provides us with needed abilities to control and test all relevant features of the SALT128 chip. A photograph of the SoC is depicted in Figure 2.11. The FPGA is an integrated circuit

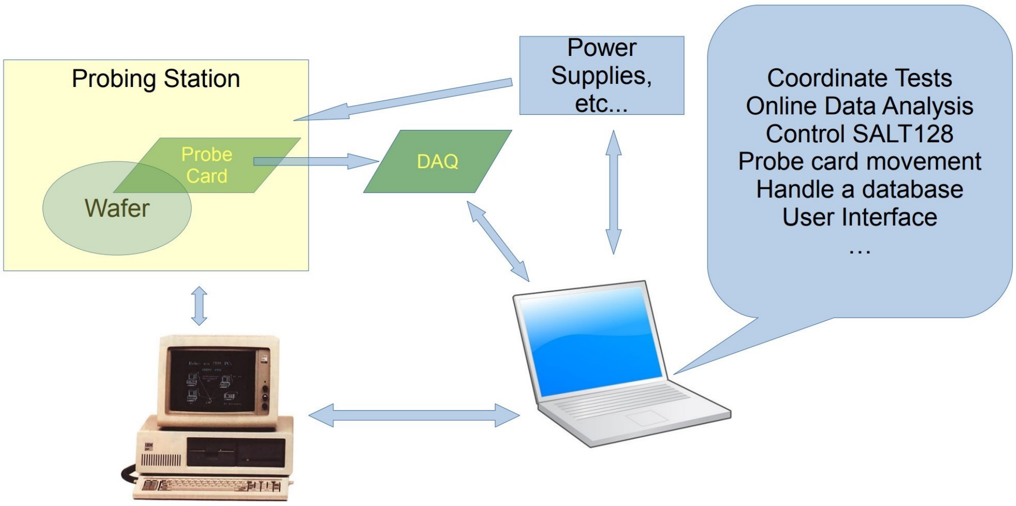

FIGURE 2.10: Schematic of the wafer testing.

designed to be configured by a user after manufacturing which is represented in the name as "field-programmable". FPGAs contain an array of programmable logic blocks, and a hierarchy of "reconfigurable interconnects" that allow the blocks to be "wired together", like many logic gates that can be inter-wired in different configurations. Logic blocks can be configured to perform complex combinational functions, or merely simple logic gates like AND and XOR. In most FPGAs, logic blocks also include memory elements, which may be simple flip-flops or more complete blocks of memory. Many FPGAs can be reprogrammed to implement different logic functions, allowing flexible reconfigurable computing as performed in computer software. The benefit of the SoC is that it also incorporates a central processor on it which allows the control of the FPGA and peripherals in an easy way without a need to reprogram the FPGA. Cyclone V has a Dual ARM Cortex-A9 processor on it and Ethernet connector that allows the whole system to be run and controlled from the special Yocto project. The Yocto project is a Linux Foundation collaborative open source project whose goal is to produce tools and processes that enable the creation of Linux distributions for embedded and IoT software that are independent of the underlying architecture of the

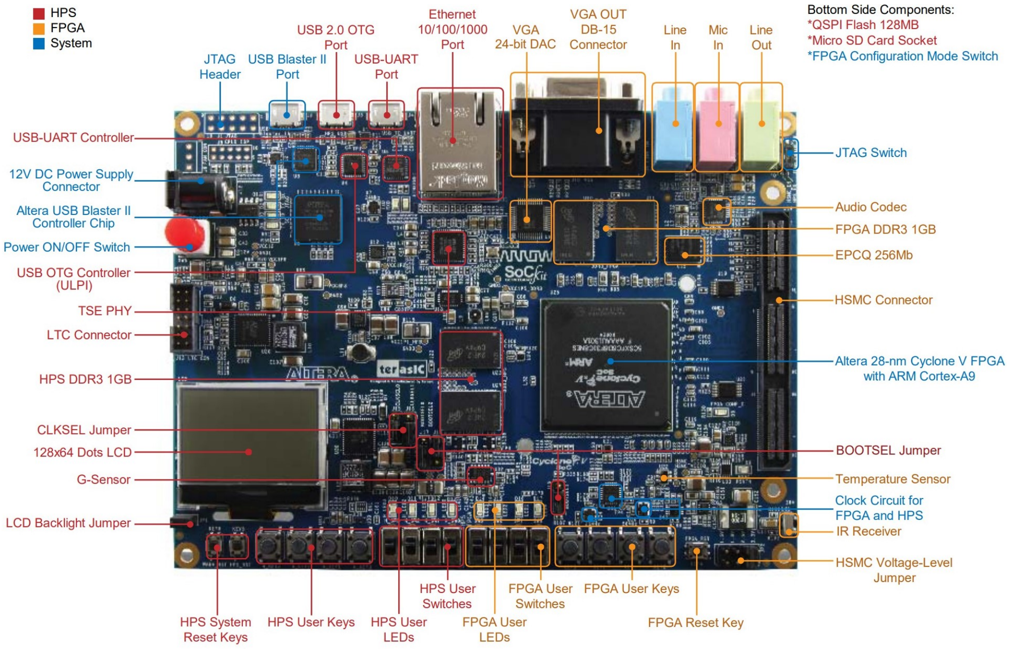

FIGURE 2.11: Cyclone V SoC develepment board [66].

embedded hardware. That allows to compile the special Linux edition with the all needed tools for controlling a FPGA device [67].

The test setup

It was decided to use an additional current reader and external ADCs to test the power consumption through the SALT128 chip and check the analogue to digital converter inside the SALT128.

As an ADC device, a ADS1115 16-Bit ADC-4 Channel with Programmable Gain Amplifier was chosen [68]. ADS1115 provides 16-bit precision at 860 samples/second over I^2C communication protocol to read analogue values. The chip includes a programmable gain amplifier to boost up smaller signals to the full range. It can run from 2V to 5V ($\pm1.024V$ and $\pm2.048V$) power/logic and can measure a large range.

As a current measurer, the Adafruit INA219 DC Current Sensor is used. It can measure both the high side voltage and DC current draw over I^2C

communication protocol with 1% precision. A programmable calibration value, combined with an internal multiplier, enables direct readouts in amperes. The device uses a single +3V to +5.5V supply, drawing a maximum of 1mA of supply current [69].

A special software package was developed to run SALT128 validation tests on Cyclone V SoC based on two programming languages: Very High Speed Integrated Circuit Hardware Description Language (VHDL) to configure logic blocks and their interconnects in FPGA and C++ to control them and directly analyse on the ARM central processing unit (CPU). LabVIEW was used to create a graphical environment to operate the probe station and control data acquisition. A diagram describing the software package is shown in Figure 2.12.

A scheme for the whole validation set-up in depicted in Figure 2.13.

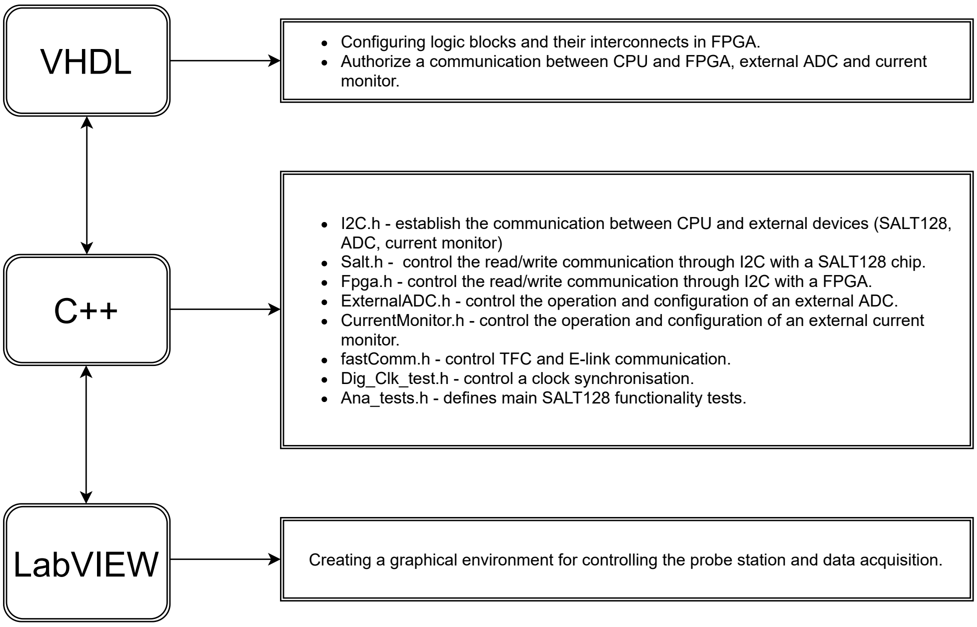

- Configuring logic blocks and their interconnects in FPGA.
- Authorize a communication between CPU and FPGA, external ADC and current monitor.

- I2C.h - establish the communication between CPU and external devices (SALT128, ADC, current monitor)
- Salt.h - control the read/write communication through I2C with a SALT128 chip.
- Fpga.h - control the read/write communication through I2C with a FPGA.
- ExternalADC.h - control the operation and configuration of an external ADC.
- CurrentMonitor.h - control the operation and configuration of an external current monitor.
- fastComm.h - control TFC and E-link communication.
- Dig_Clk_test.h - control a clock synchronisation.
- Ana_tests.h - defines main SALT128 functionality tests.

Creating a graphical environment for controlling the probe station and data acquisition.

FIGURE 2.12: Diagram of the code intercommunication in the software package for SALT128 tests.

The Labelling Scheme

All tested chips on the wafer are classed in three categories:

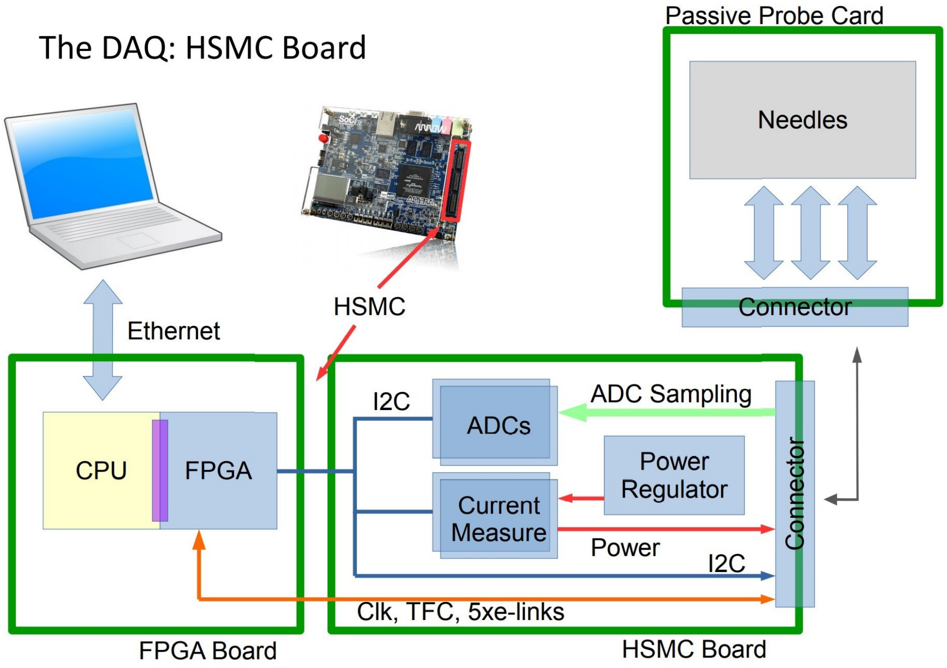

FIGURE 2.13: Schematic view of the system for SALT128 tests.

- Good chips.

  In all tests parameters fall within specifications/tolerance, no bad channels.

- Adequate chips.

  In all tests parameters fall within specifications/tolerance, with only one bad channel present.

- Bad chips.

  One or more parameters fall outside specifications/tolerance; two or more bad channels.

All chips are marked on the scheme according to which group they belong and sent to wafer dicing, while all information is kept. Only chips within a green group must be integrated in the UT. The yellow category will only be used depending on the yield of green category.

A labelling is done within the probing station software. An example of the labelling scheme from the probing station is shown in Figure 2.14. Here, a configuration and colours do not reflect SALT128 wafers.

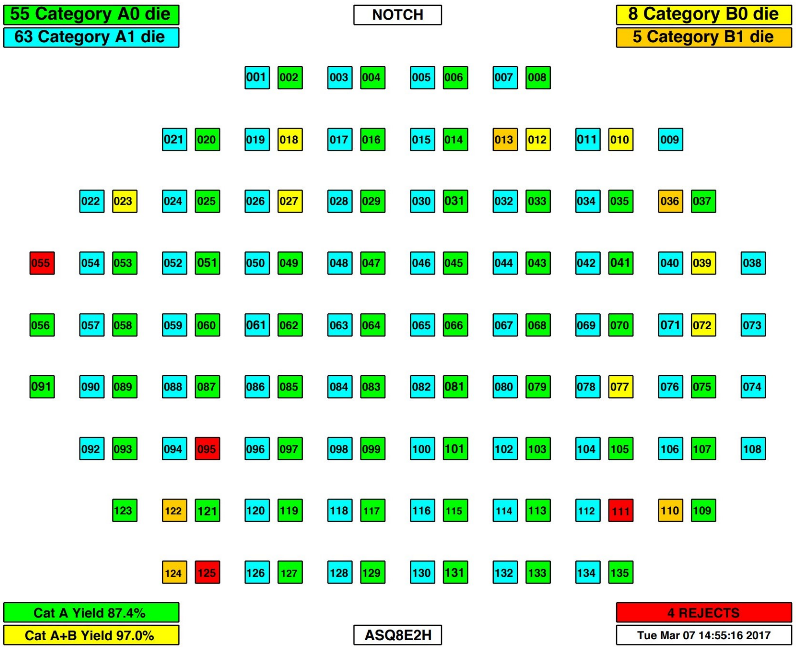

FIGURE 2.14: Example of the labelling scheme on the wafer.

2.2.2 Tests to be performed

In order to validate that chip is good to be installed in the UT all main features of it must be tested. Such as:

- Power tests.

  Test the proper start up of the chip. Check that digital and analogue currents are being drawn correctly. The external current reader is used for this purpose. Both, analogue and digital power consumption, as well as the total current and voltage readings must fall within a tolerance range:

$150 < I_{\text{analogue}} < 250$ mA $\quad 200 < I_{\text{total}} < 600$ mA
$100 < I_{\text{digital}} < 300$ mA $\quad 1.1 < V < 1.3$ V

Distributions of the currents for one wafer is shown in Figure 2.15.

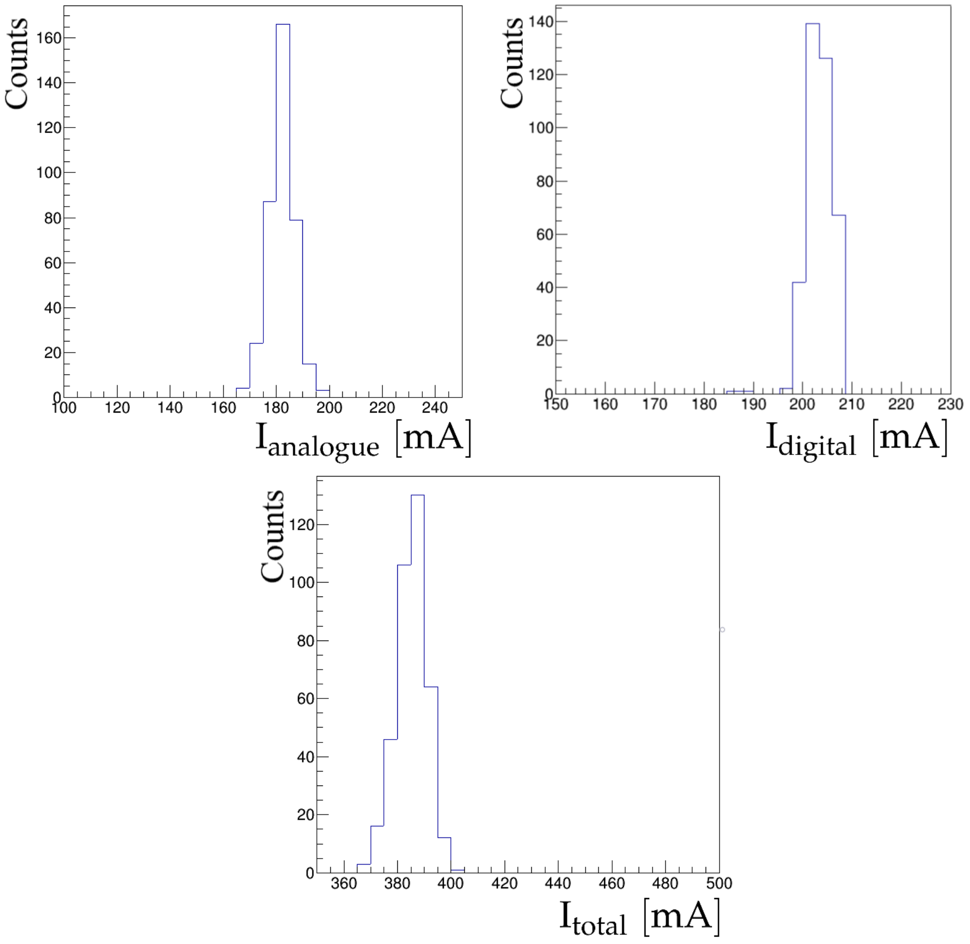

FIGURE 2.15: Distributions of analogical, digital and total power consumption of "good" chips in the wafer (example).

- Communication with I^2C.

  Test that it is possible to write to the main SALT128 registers using the I^2C-bus and read the chip response back.

  - Serializer registers.

    The serializer circuit is used to seralise the data generated in digital signal processing (DSP) and to send it out via the scalable low voltage signaling (SLVS) interface. The serializer sends a byte every main clock cycle.

  - DSP registers.

    The DSP circuitry performs a pedestal subtraction, a mean common mode subtraction and a zero-suppression on the 6-bit data-stream coming from the ADC.

  - Single Event Upset (SEU) registers.

    The technique used in SALT128 for SEU reduction is a Triple Modular Redundancy (TMR) applied to almost every flip-flop in the whole digital part.

- Clock generation tests.

  - Delay Locked-Loop (DLL)

    Internal DLL is dedicated to shift external 40 MHz clock to obtain the ADC sampling signal and to generate test pulse.

  - Phase Locked-Loop (PLL)

    PLL is used for clock multiplication to get a fast 160 MHz clock in the data serialization circuit. The PLL can work in the frequency range 80 MHz – 400 MHz and is characterized by very low power consumption.

- The Timing and Fast Control (TFC) interface and data packet tests.

- DAC tests.

Record output of each DAC over the range of possible values to confirm proper behaviour. Calibrate internal DACs with external ADCs.

- Digital tests.

  Check that the chip can be configured. This includes being able to read/write registers, read chip addresses, pass signals in both directions.

- Analogue tests.

  Checking by five point gain tests (inject five different charges) and read out ADC values to assess analogue functionality comparing. DACs are subject to gain and offset errors due to mismatches in resistors. The trimming technique is being employed to counter the effect of the mismatches. An example of the trim DAC scan for a chip using 10 runs is shown in Figure 2.16.

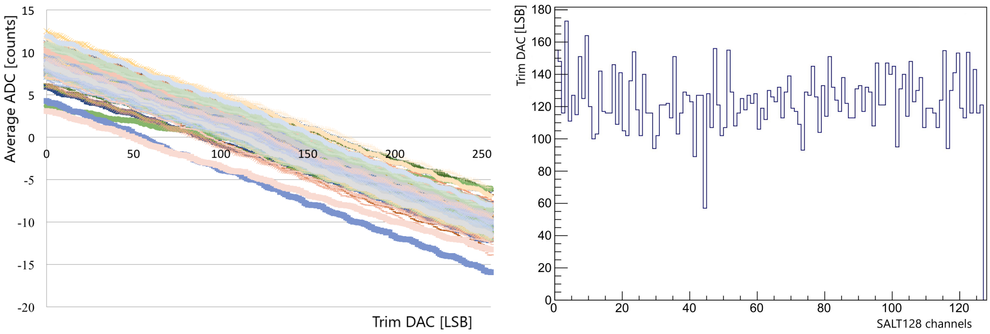

FIGURE 2.16: Example of a trim DAC scan (left) and a best trim configuration for each channel (right).

- Gain uniformity test.

  Check output signal uniformity across channels for a given input. Should test for different input charge.

- Clock checks.

Check different phase shifts of the clock and data lines to confirm optimal value.

- Cross-talk studies.

  Confirm that cross-talk is less than 10% between neighbouring channels. An example of the cross-talk distribution for one wafer is shown in Figure 2.17.

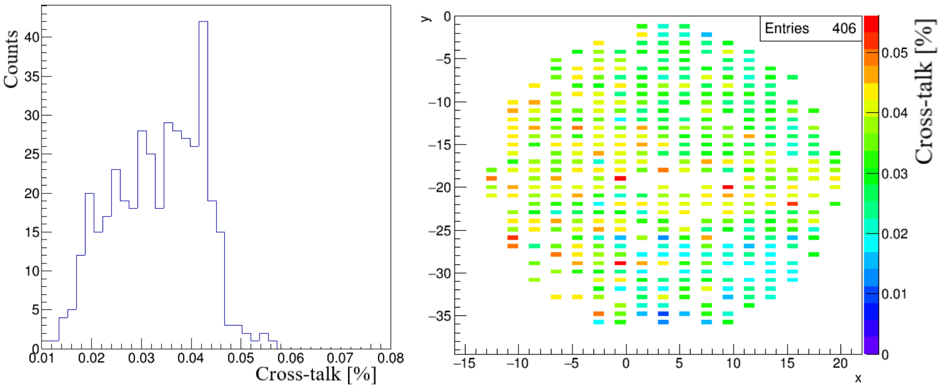

FIGURE 2.17: Distributions of cross-talk of "good" chips in the wafer (example).

- Check proper:

  zero-suppression

  the run is performed with a set zero suppression threshold. The check is successful if no channels have hits above the threshold;

  pedestal subtraction

  the run is performed with a set common pedestal to all channels and repeat 10 times. The check is successful if the average ADC value in each channel is with 2 ADC counts of the set pedestal value;

  mean common mode subtraction (MCMS)

the idea of MCMS block operation is to calculate an average value of all channels without a hit and subtract this value from all channels. Two thresholds are used to distinguish between channels with and without hit. The main threshold is used for the MCMS algorithm, while the second threshold is needed to exclude channels with an extremely low values. The run is performed with set thresholds and set data after pedestal subtraction.

- Check the intrinsic and MCMS noise per channel.

  the run is performed with a set MCMS thresholds and repeat 10 times. The average ADC value is calculated per channel and for whole chip. The check is successful if no channel is outside the range of 5 RMS of the chip. An example of the noise distribution for a wafer is shown in Figure 2.18.

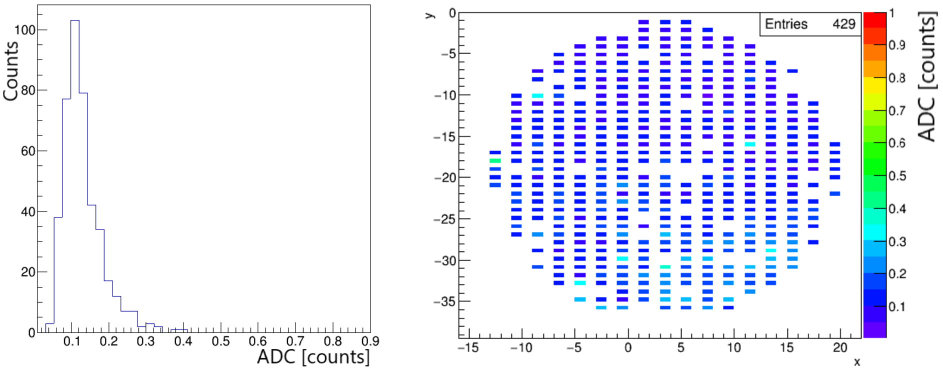

FIGURE 2.18: Distributions of noise mean value of "good" chips in the wafer (example).

2.3 Results

The measurements were carried out in July 2019 at CERN. In total, 18 wafers were tested with 467 chips each. An average time of the testing procedure over one chip was around 30 seconds.

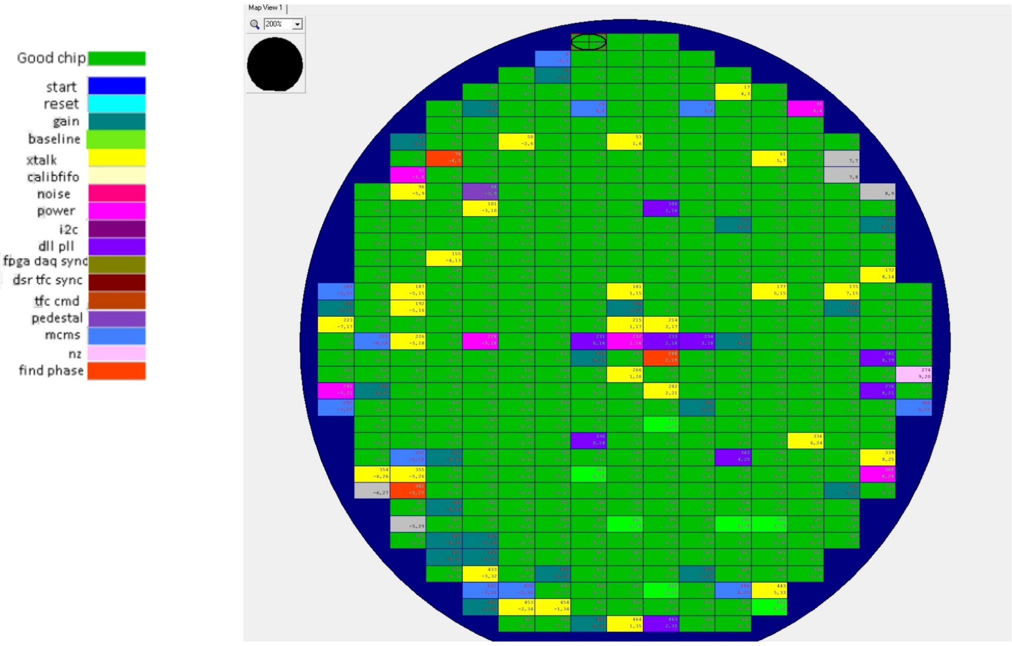

FIGURE 2.19: Results of the validation tests running (example).

The final result for one wafer is shown in Figure 2.19. However, chips which failed one channel/test still can be used for the outer regions of the UT where the intensities are lower, in the case some chips marked as good become damaged at a later stage.

Wafer	Yield, %	N_{chips}	Wafer	Yield, %	N_{chips}
18B4	81	378	09F7	81	378
17C1	77	360	08G4	82	383
16C6	77	360	07H1	86	402
15D3	79	369	06A3	87	406
14E0	73	341	05B0	83	388
13E5	77	360	04B5	84	392
12F2	79	369	03C2	87	406
11F7	85	397	02C7	85	397
10G4	82	383	01D5	90	420

TABLE 2.1: Fraction of good chips per wafer.

The final numbers of SALT128 chips on each wafer that were flagged as "good" are shown in Table 2.1. The average yield of good chips is $\approx$ 82%, which results in 6889 chips and provides the required $\approx$ 4000 SALT128 to be installed in UT.

2.4 Summary

The developed system to test final readout chips for silicon sensors intended to be installed in the upstream tracker of the future LHCb upgrade was presented in this chapter. The system checks all the main functionality of the chip, and is quick. 8406 SALT128 ASICs were tested and showed the rate of 82% successful chips which is sufficient for the UT.

Chapter 3

Probing lepton flavour universality with semileptonic $\Lambda_b^0 \to \Lambda_c^+ \tau^- \overline{\nu}_\tau$ decays

3.1 Introduction

Lepton Flavour Universality (LFU) was mentioned as one of the possible indications of the presence of new physics in Chapter 1. As we know, according to SM, the electroweak bosons couple with the same strength to the three families of leptons, where the only difference in their behaviour caused by the interaction with the Higgs boson, i.e. the mass difference. In recent years, some deviations from SM predictions in $b \to sll$ and $b \to cl\nu$ transitions has been observed. The measurements were performed by calculating so-called R-values, which are ratio of branching fractions for b decays into two different lepton flavours. This observable allows to have both a theoretically (by cancelling QCD uncertainties) and experimentally (by cancelling reconstruction uncertainties) clean result. The $b \to cl\nu$ deviation has been seen by different experiments, however the average discrepancy hasn't reached the 5σ level, which is a requirement to claim a discovery. This motivates us to make more measurements with higher signal yields and analogous decay channels, in order to shed light on these anomalies. One of these measurements of interest, known as $R(\Lambda_c^+)$[1], was studied in this thesis and described in the following.

3.1.1 Previous measurements

Tests of $\tau - \mu$ universality have focused on observables with the $b \to c\tau^-\overline{\nu}_\tau$ transition. The Feynman diagram of this transition is depicted in Figure 3.1. The decay proceeds via a tree-level diagram, therefore large branching fractions and signal yields are expected. However, the analysis is complicated by the reconstruction of a τ lepton due to presence of missing neutrinos. The reconstruction of τ leptons can be done using its muonic decay, $\tau^- \to \mu^-\overline{\nu}_\mu\nu_\tau$, and hadronic decay, $\tau \to \pi^-\pi^+\pi^-\nu_\tau$ or $\tau \to \pi^-/\rho^-\nu_\tau$.

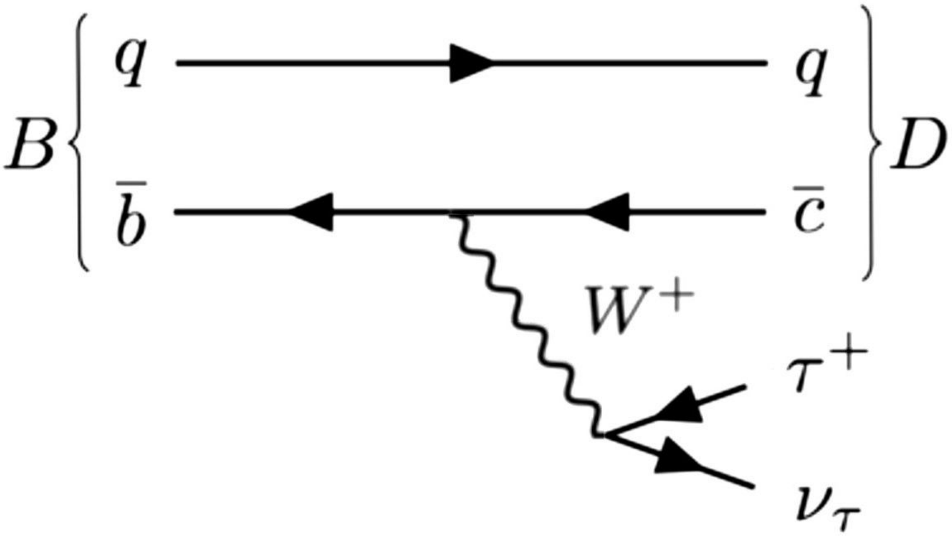

FIGURE 3.1: Feynman diagram of the tauonic $B^0 \to D^-\tau^+\nu_\tau$ decay according to the SM.

---

[1] Charge conjugation processes are implied from now on.

The muonic channel is convenient, as it allows to cancel most of reconstruction uncertainties due to the same final states for signal ($B^0 \to D^{(*)+}\tau^-\overline{\nu}_\tau$) and normalisation ($B^0 \to D^{(*)+}\mu^-\overline{\nu}_\mu$) decays and have high signal yields. However, a difficulty arises in differentiating the muon originating from the τ^- decay and one coming directly from a B^0 or $D^{(*)+}$ meson. Furthermore, the presence of additional neutrinos in the final state complicates the vertex and momentum reconstruction.

There are three experiments which have measured $R(D^{(*)+})$: BaBar, Belle and LHCb. The BaBar and Belle experiments are positioned inside e^+e^- colliders, called B-factories, with energies corresponding to the mass of the $\Upsilon(4S)$ resonance (Figure 3.2), that decays afterwards into two B mesons. These experiments use a tagging technique to reconstruct signal candidates.

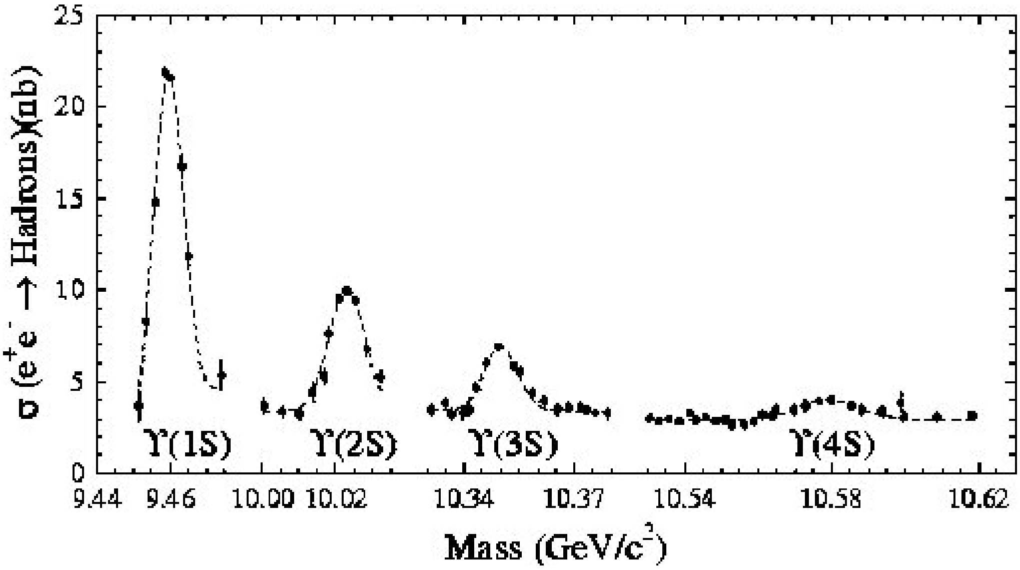

FIGURE 3.2: Cross-section of electron-positron interactions in the region of the Υ resonances. Only the 4th resonance has a mass sufficient to produce a pair of two B mesons [70].

In semitauonic analyses, the two B mesons are assigned as the tagged B_{tag} meson and the signal B_{sig} meson. The reconstruction technique is depicted in Figure 3.3. The benefit of such measurements is that it is possible to fully reconstruct the B_{tag} which allows to have the full kinematic information of the B_{sig} before any signal reconstruction. Tagged B meson can be reconstructed through hadronic modes or semileptonic modes to select signal candidates. Hadronic modes have higher purity but lower efficiency whereas semileptonic modes have higher efficiency with lower purity.

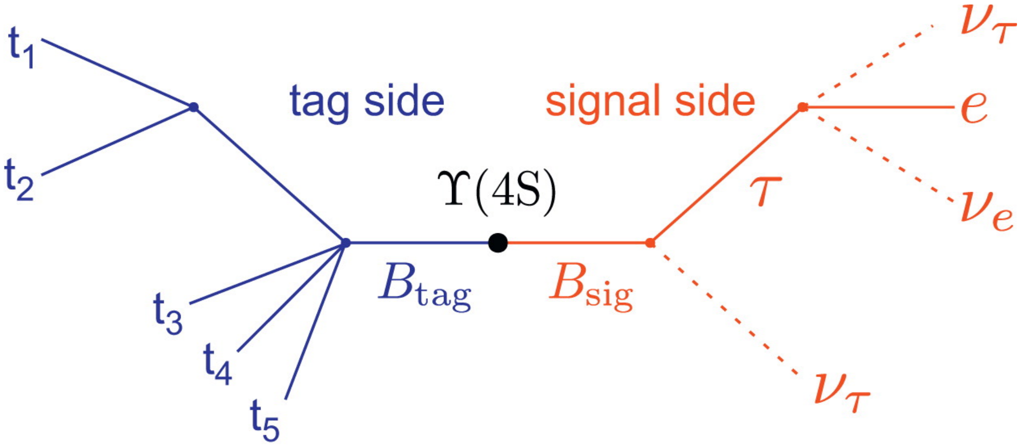

FIGURE 3.3: Illustration of the typical B-factory event [71].

The first combined measurement of $R(D^+)$ and $R(D^{*+})$ was published by the BaBar collaboration using the hadronic tag [14, 15] in 2012, followed by the Belle combined measurement also using a hadronic tag in 2015 [16]. In addition, Belle has published results on $R(D^{*+})$ measurements and the τ^- polarisation using the semileptonic tag, reconstructing τ^- lepton through $\tau^- \to \pi^-\nu_\tau$ and $\tau^- \to \rho^-\nu_\tau$ decay modes in 2017 and 2018 [17, 18]. In 2019, the Belle experiment also presented results on both, $R(D^+)$ and $R(D^{*+})$, using a semileptonic tag while reconstructing the signal-side τ^- in a purely leptonic decay [19].

Measurements of $R(D^{*+})$ were also performed by the LHCb experiment which has very different experimental conditions. It is located on the LHC proton-proton accelerator with significantly higher energies. The creation of the b quark pair happens predominantly through gluon-gluon fusion making them fly collinearly close to the beam line. The cross-section of $b\bar{b}$ production is five orders of magnitude higher compared to the B-factories. However, there is an additional complexity in that b hadrons are produced by inelastic interactions in a high multiplicity environment. In this environment, the b hadron longitudinal momentum is unknown and needs to be approximated with kinematic assumptions. This results in a poorer resolution for the decay variables of interest in the analysis compared with the B-factories. In addition, the trigger system must be selective in this environment, which preferentially favours muons with respect to electrons. For this reason, the LHCb measurements only use the muonic decay channel, omitting electrons in the analysis.

LHCb performed the first measurement of $R(D^{*+})$ in 2015 with the 3 fb^{-1} of data using the leptonic decay $\tau^- \to \mu^- \overline{\nu}_\mu \nu_\tau$ [13], followed by a measurement in 2017 that exploited the hadronic decay $\tau^- \to \pi^+ \pi^- \pi^+ (\pi^0) \nu_\tau$ [72]. The muonic channel had high signal yields but low purity, whereas the hadronic channel had higher purity but lower signal yields. Also, the hadronic channel had to normalise to another hadronic decay to measure $R(D^{*+})$ which is not true for the muonic channel.

The combined results of all three experiments leads to a deviation of 3.08σ from SM predictions. An important fact to mention is that all experiments observe deviations in the same direction, despite the different experimental conditions. However, the combined significance is not conclusive and so we require more measurements to be performed with more data to improve statistical uncertainties and also with different decay modes to have independent systematic uncertainties.

3.1.2 Advantage of the $R(\Lambda_c^+)$ measurement

So far, only measurements of $R(D^+)$ and $R(D^{*+})$ were performed. However, if new physics contributes to these decays, we expect to see it in all types of $b \to c\ell\nu_\ell$ transitions. The measurement which is presented here is

$$R(\Lambda_c^+) = \frac{BR(\Lambda_b^0 \to \Lambda_c^+ \tau^- \overline{\nu}_\tau)}{BR(\Lambda_b^0 \to \Lambda_c^+ \mu^- \overline{\nu}_\mu)},$$

where the Λ_c^+ baryon is reconstructed through the $\Lambda_c^+ \to pK^-\pi^+$ decay chain and the τ^- decays semileptonicaly, $\tau^- \to \mu^- \overline{\nu}_\mu \nu_\tau$.

The Feynman diagram of this decay is shown in Figure 3.4. The difference to previous measurements is not only in the particles taking part in the decay, but also in their spin structure. It allows not only to test LFU, but also to improve the understanding of the potential origin of any discrepancy.

The contribution of the $\Lambda_c^{*+} \to \Lambda_c^+ \pi^+ \pi^-$ decay is crucial and must be included in studies. This allows us to measure also the $R(\Lambda_c^+ \pi^+ \pi^-)$ observable.

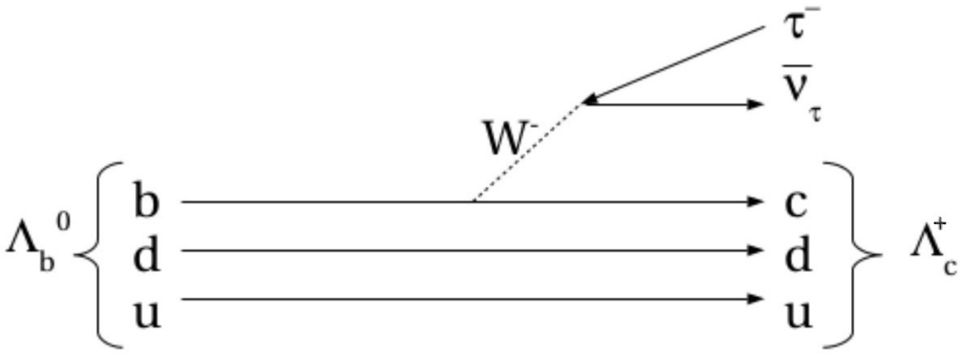

FIGURE 3.4: Feynman diagram of the tauonic $\Lambda_b^0 \to \Lambda_c^+ \tau^- \overline{\nu}_\tau$ decay according to the SM.

In addition, there are also several supplementary benefits of studying this decay channel.

- First of all, the branching fraction of the Λ_b^0 baryon decaying to semileptonic ground state $\Lambda_c^+\ell^-\overline{\nu}_\ell$ is 6% which is three times higher compared to the 2% of the $B^0 \to D^+\ell^-\overline{\nu}_\ell$ decay ($\frac{BR(\Lambda_b^0 \to \Lambda_c^+\ell^-\overline{\nu}_\ell)}{BR(B^0 \to D^+\ell^-\overline{\nu}_\ell)} \approx 3$) [6]. This means less feeddown and higher signal yields for $R(\Lambda_c^+)$ with respect to $R(D^+)$.

- Due to baryon conservation, we have a reduced number of the double-charmed (consisting of more than one hadron containing charm quark) hadron combinations produced in the Λ_b^0 decays. That makes our sample cleaner from background.

- One of backgrounds originates from similar decays with additional pions which are not reconstructed, such as $\Lambda_c^{*+} \to \Lambda_c^+\pi^+\pi^-$. Another conservation law, i.e. isospin conservation, requires the creation of at least two pions in the feed down. Therefore, it will be necessary to have both pions being undetected to misinterpret it for a signal decay. Even in that case, they will take away a bigger amount of energy compared to the one pion case which will be noticeable in the final spectrum.

- Lepton universality tests in different decays helps us to clarify the contribution of new physics. Due to well understood theoretical uncertainties we can express $R(\Lambda_c^+)$ value through $R(D)^+$ and $R(D^{*+})$ [73]. That makes it an essential measurement to validate $R(D^{*+})$ anomaly.

$$\frac{R(\Lambda_c)}{R(\Lambda_c)_{SM}} \approx 0.262 \cdot \frac{R(D)}{R(D)_{SM}} + 0.738 \cdot \frac{R(D^*)}{R(D^*)_{SM}}$$

3.2 Selection

The dataset collected in 2016 from the LHCb experiment was used in these studies in two configurations - MagUp and MagDown - that correspond to different magnet polarities. During the data-taking, the data are filtered through the trigger stage in order to reduce the datasets to a manageable size. The trigger consists of the L0, implemented in hardware, and the high level trigger (HLT), implemented in software. The task of the trigger is to choose only events with a b-hadron candidate decaying semileptonically to a final state containing a c hadron.

Trigger pathways must be chosen to avoid a bias to the signal and normalisation decays fit shapes that can prevent their separation in the fit. Therefore, for the $R(\Lambda_c^+)$ analysis we require our events to pass trigger lines that are independent of the reconstructed muon candidate and avoid any cuts on its transverse momentum. The L0 trigger selects events where at least one out of two conditions are satisfied: any hadron of the Λ_c^+ decay has a transverse energy higher than 3.7 GeV$/c$ or any particle, which is not associated with the signal decay, passes the L0 trigger requirement associated to its type [74]. Events selected by the L0 trigger are transferred to the first stage of the HLT trigger, which performs the reconstruction of a primary vertex and all tracks associated with the trigger signal candidate with a transverse momentum larger than 500 MeV$/c$. The selection of events is based on a single track (or two-tracks) with the high transverse momentum, the decay vertex of which is displaced with respect to the primary vertex. The second stage of the HLT trigger performs the full track reconstruction and selects n-body b-hadron decays containing charmed hadron and muon.

A loose preselection of candidates is performed afterwards in order to select among all these events ones that look like $\Lambda_b^0 \to \Lambda_c^+ \tau^- (\mu^-) \overline{\nu}_{\tau(\mu)}$

and is known as the "stripping". We apply the stripping line that keeps only events of type $\Lambda_b^0 \to \Lambda_c^+ \mu^- X$, where X can be any number of other particles. The stripping requirements of the line is shown in Table 3, where the variables defined as follow:

- χ^2_{vertex} is the χ^2 of the fit of the vertex.
- $\chi^2_{vertex}/N_{d.o.f}$ is the χ^2 per a number of degrees of freedom of the fit of the vertex.
- $\chi^2_{track}/N_{d.o.f}$ is the χ^2 per a number of degrees of freedom of the fit of the track.
- P_{ghost} is the ghost probability to identify reconstructed tracks which do not correspond to a real particle.
- Δm is the absolute difference between the measured mass and the particle data group (PDG) reference value.
- $\chi^2_{\delta(SV-PV)}$ is the χ^2 distance between the decay vertex and the primary vertex (PV).
- $DIRA$ is a cosine of the direction angle of two tracks.
- $min(\chi^2_{PV})$ is the minimum χ^2_{PV} distance of a particle to PV.
- DLL_h is the logarithm of the likelihood of the hadron mass hypotheses.
- $isMuon$ is a boolean decision obtained from the extrapolation of a track through the muon stations, making a statement about whether a track is consistent with a muon hypothesis [75].

In addition, we require the mass of Λ_c^+ to be within the range of 2230 - 2330 MeV/c^2. A boosted decision tree (BDT) classifier is applied to discriminate between background and signal events in the Λ_c^+ peak. A

$\Lambda_c^\pm$
$\Delta m < 80$ MeV
$\sum_{\pi,K,P} p_T > 2500$ MeV
$\chi^2_{vertex}/N_{d.o.f}$ <4
$\chi^2_{\delta(SV-PV)}$ >25
$DIRA > 0.999$

	$p^\pm$	$K^\pm$	$\pi^\pm$	$\mu^\pm$
$\chi^2_{track}/N_{d.o.f}$	>4	>4	>4	>5
P_T	>300 MeV/c	>300 MeV/c	>300 MeV/c	>800 MeV/c
P	>2 GeV/c	>2 GeV/c	>2 GeV/c	>3 GeV/c
P_{ghost}	<0.5	<0.5	<0.5	<0.5
$min(\chi^2_{PV})$	>9	>9	>9	>16
PID	$DLL_p > 0$	$DLL_K > 4$	$DLL_K < 2$	$isMuon = 1$

TABLE 3.1: Requirements for the stripping line to select $\Lambda_b^0 \to \Lambda_c^+ \mu^- X$ decays.

list of discriminating variables used in BDT is shown in Table 3.2, where $IP\chi^2$ is the χ^2 distance of a given particle to the PV. Output of the BDT classifier is shown in Figure 3.5. A BDT score higher than 0.4 is chosen to select the signal candidate.

Discrimination variable	Particle
χ^2_{vertex}	Λ_c
$IP\chi^2$	Λ_c, p, π, K
P_T	p, π, K
PID	p, π, K

TABLE 3.2: Variables used for BDT discrimination.

To remove additional background from the peak region, the sWeight technique[76] was applied using the mass of the Λ_c^+ particle ($m(\Lambda_c^+)$) as the discriminating variable. The fit function is the combination of two gaussians with the same mean, but different σ and an exponential function. The result of the fit to Λ_c^+ mass peak is shown in Figure 3.6.

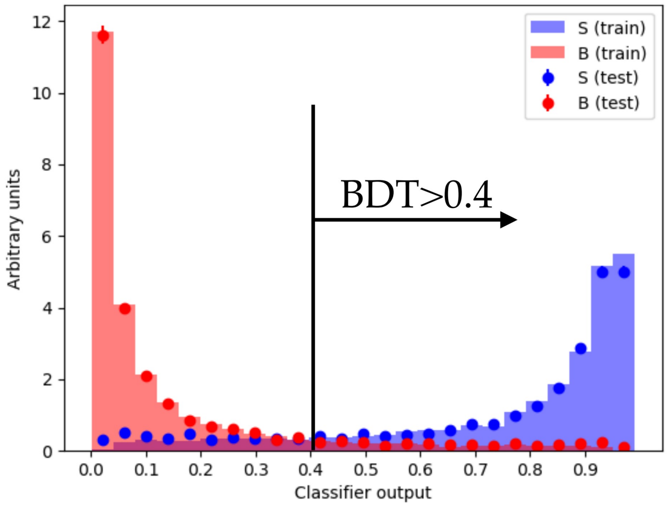

FIGURE 3.5: Distribution of the BDT response on the signal and background simulated samples.

3.3 Methodology and challenges

3.3.1 Distinguishing decays with the same final state: Kinematic variables

The τ^- particle in the decay $\Lambda_b^0 \to \Lambda_c^+ \tau^- \overline{\nu}_\tau$ can be reconstructed through two different decay channels, hadronic or semileptonic. The advantage is that τ^- leptons decaying to the hadronic channel can be easily separated from the normalisation decay in the $\Lambda_b^0 \to \Lambda_c^+ \mu^- \overline{\nu}_\mu$. However, it is highly contaminated from large hadronic backgrounds and one must take into account reconstruction efficiencies of different particles in the final state. Therefore, we have decided to use the muonic, $\tau^- \to \mu^- \overline{\nu}_\mu \nu_\tau$ decay mode.

In Table 3.3 we can see that the visible final state is the same for both signal and normalisation channels, since neutrinos cannot be detected in the LHCb.

Consequently, we cannot differentiate the two decays based on their decay products or visible mass. Instead, we can separate them by looking

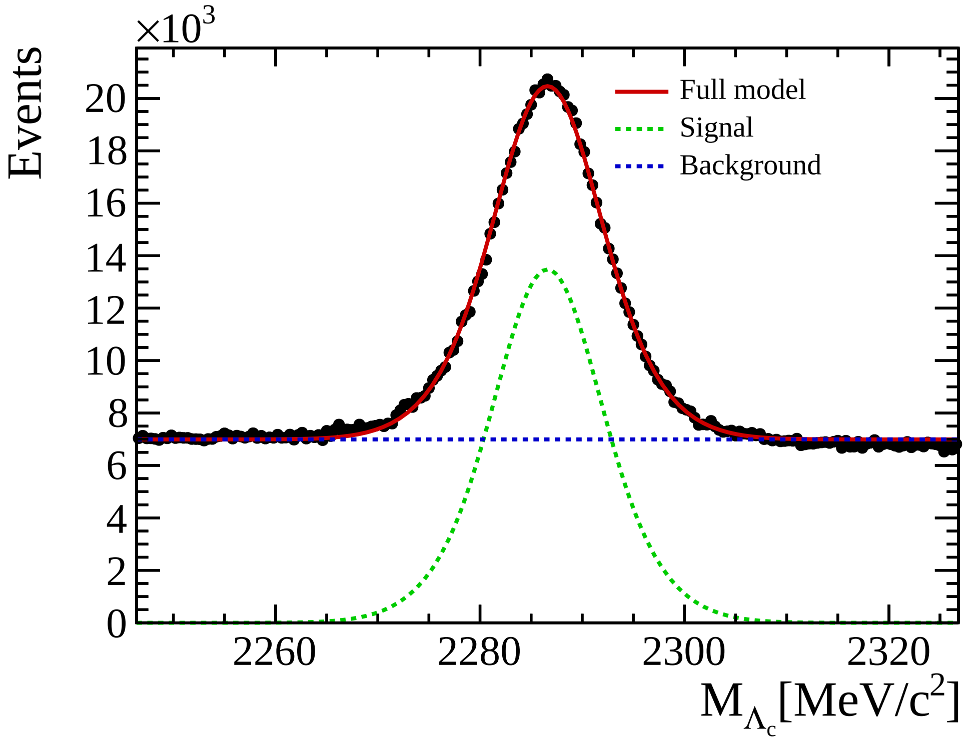

FIGURE 3.6: Fit to the Λ_c^+ mass distribution.

	initial decay of Λ_b^0	final state particles
signal	$\Lambda_c^+ \tau^- \overline{\nu}_\tau$	$pK^-\pi^+\mu^-\nu_\tau\overline{\nu}_\mu\overline{\nu}_\tau$
normalisation	$\Lambda_c^+ \mu^- \overline{\nu}_\mu$	$pK^-\pi^+\mu^-\overline{\nu}_\mu$

TABLE 3.3: Decay chain of Λ_b^0 to signal and normalisation channels. Visible decay daughters are shown in blue, while green indicates particles that cannot be seen in the detector.

at the kinematic distribution of the final state in the Λ_b^0 rest frame. The rest frame of the Λ_b^0 decay cannot be fully reconstructed in the LHCb environment due to missing particles in the final decay. The z component of the Λ_b^0 four-velocity is assumed to be equal to the visible part of the decay, as an approximation for the rest frame [77]. The signal and normalisation channels are distinguished using the three kinematic variables shown in Figure 3.7.

- Missing mass squared - $M^2_{missing} = (p_{\Lambda_b^0} - p_{\Lambda_c^+} - p_{\mu^-})^2$. The mass of the neutrino is negligible. However, the three-neutrino system in the final state of the signal decay $\Lambda_b^0 \to \Lambda_c^+(\mu^-\overline{\nu}_\mu\nu_\tau)\overline{\nu}_\tau$ will form a larger invariant mass from the visible system compare to one neutrino of the normalisation decay $\Lambda_b^0 \to \Lambda_c^+ \mu^- \overline{\nu}_\mu$. Therefore, the distribution of the muonic channel should peak towards region of lower masses, whereas the signal distribution is broader and shifted towards higher masses.

- Muon rest frame energy - E_μ^*. The muon originating from the secondary decay of the τ^- lepton is on average much softer than the one originating from the Λ_b^0 decay directly. Therefore, its energy distribution will peak at lower values than for the normalisation channel.
- Invariant mass of the dilepton system - q^2. Another variable which behaves differently for signal and normalisation is the invariant mass of the dilepton system $q^2 = (p_{\Lambda_b^0} - p_{\Lambda_c^+})^2$, which cannot be smaller than the squared mass of the emitted lepton. While for the normalisation channel the minimum q^2 equals to the squared mass of the muon, which can be considered as essentially zero, for the signal the value of q^2 must be more than $m_{\tau^-}^2 = (1.777\ \text{GeV}/c^2)^2 \approx 3.158\ (\text{GeV}/c^2)^2$.

3.3.2 Multidimensional fit and histFactory

To perform the kinematic discrimination, we perform a 3D binned fit to the three observables ($M_{missing}^2, E_\mu^*, q^2$), that from now on will be referred to as the fit variables. It was decided to use a template fit approach for this analysis, which means that template histograms are used as components of a binned fit. Templates are derived from the simulated samples and from the data-driven control samples. The goal of the fit is to extract the relative $\Lambda_b^0 \to \Lambda_c^+ \tau^- \overline{\nu}_\tau$ and $\Lambda_b^0 \to \Lambda_c^+ \mu^- \overline{\nu}_\mu$ yields, considering all possible components. In addition, the analysis strategy is to

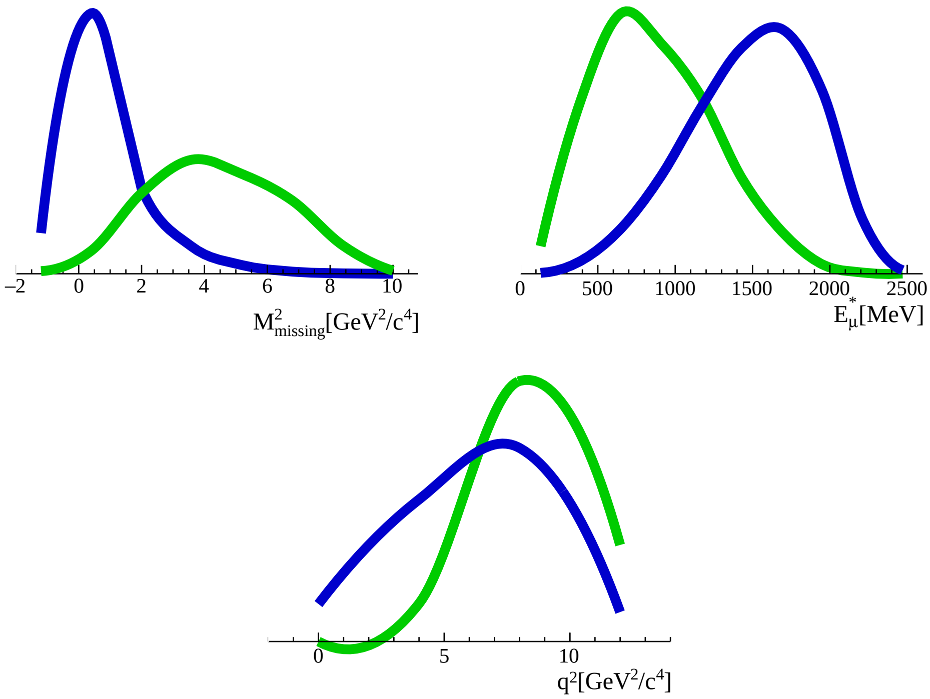

FIGURE 3.7: Illustration of kinematic variables distributions that are used to separate various decays. The green color represents the $\Lambda_b^0 \to \Lambda_c^+ \tau^- \overline{\nu}_\tau$ decay, blue - the $\Lambda_b^0 \to \Lambda_c^+ \mu^- \overline{\nu}_\mu$ decay.

fit simultaneously the different control regions based on the isolation of additional particles. The binned template fit is implemented using the HistFactory [78] toolkit which is a specialised ROOT [79] based tool to construct probability density functions from histograms. As input, it takes histograms of the data and histogram templates of the different components modelled from simulations. The tool takes into account the finite number of events for each component which allows the statistical uncertainty due to the sizes of the simulation samples to be estimated. It also allows us to implement the shape variations for components for the systematic uncertainties which are modulated by Gaussian nuisance parameters. The histogram templates for each signal and background modes were created using:

- 10 bins in $M^2_{missing}$ with $[-2 < M^2_{missing} < 14](\mathrm{GeV}^2/c^4)$

- 10 bins in E_μ^* with $[0 < E_\mu^* < 2600]$(MeV)
- 4 bins in q^2 with $[-2 < q^2 < 14]$(GeV$^2/c^4$)

The binning scheme is the same as that used in the existing $R(D^{*+})$ LHCb measurement and was chosen in the way to balance the low number of bins to speed up the fit performance and avoiding biases by keeping the fit stability and the best shapes description. The ratios of $R(\Lambda_c^+) = \frac{BR(\Lambda_b^0 \to \Lambda_c^+ \tau^- \overline{\nu}_\tau)}{BR(\Lambda_b^0 \to \Lambda_c^+ \mu^- \overline{\nu}_\mu)}$ and $R(\Lambda_c^+ \pi^+ \pi^-) = \frac{BR(\Lambda_b^0 \to \Lambda_c^{*+}(\to \Lambda_c^+ \pi^+ \pi^-) \tau^- \overline{\nu}_\tau)}{BR(\Lambda_b^0 \to \Lambda_c^{*+}(\to \Lambda_c^+ \pi^+ \pi^-) \mu^- \overline{\nu}_\mu)}$ are the parameters of interest of the fit. An example fit is shown in Figure 3.8. The backgrounds contributing to this fit will be discussed in Section 3.5.

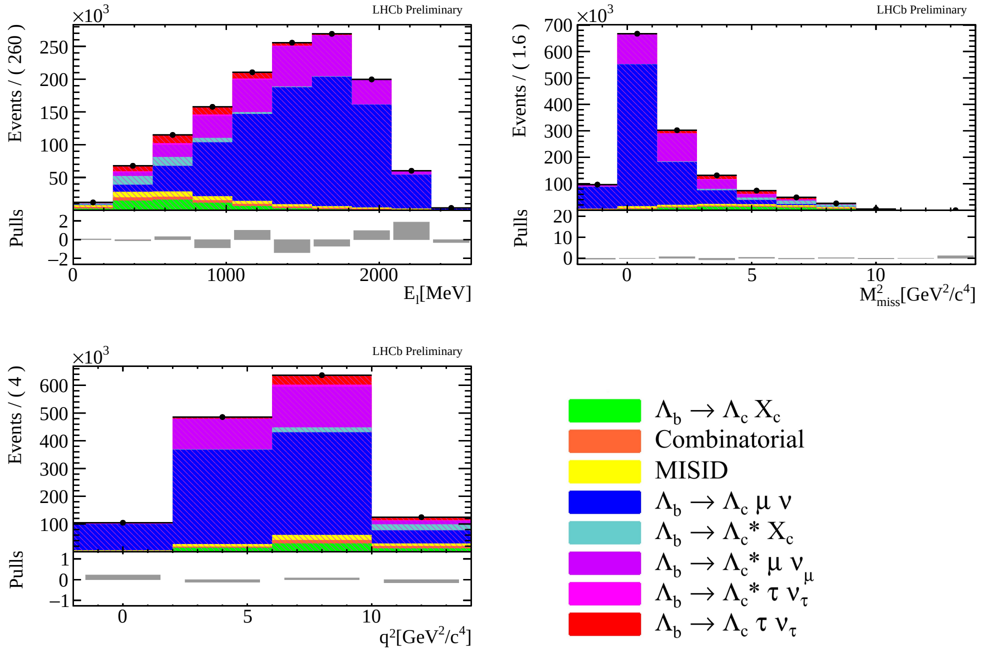

FIGURE 3.8: Example of the template fit of three kinematic observables using HistFactory.

3.4 Simulated samples

3.4.1 Trigger emulations

The difficulty of selecting semileptonic decays is caused by neutrinos in the final state which requires to have very large Monte-Carlo (MC) samples to precisely model distributions. Ideally, we wish to have MC samples of near infinite size, but this cannot be achieved due to the computing limitations. Hence, the goal is to find a balance between computer power consumption and keeping the statistical uncertainties from simulation lower than those from data.

A sample of full simulation was initially generated for this analysis corresponding to 10^8 events. In order to check the impact of MC uncertainties and validate the fit, we generated pseudodata sample consisting of the combination of templates according to expected contributions. An example of the fit to pseudodata with the details of the components discussed later is shown in Figure 3.9.

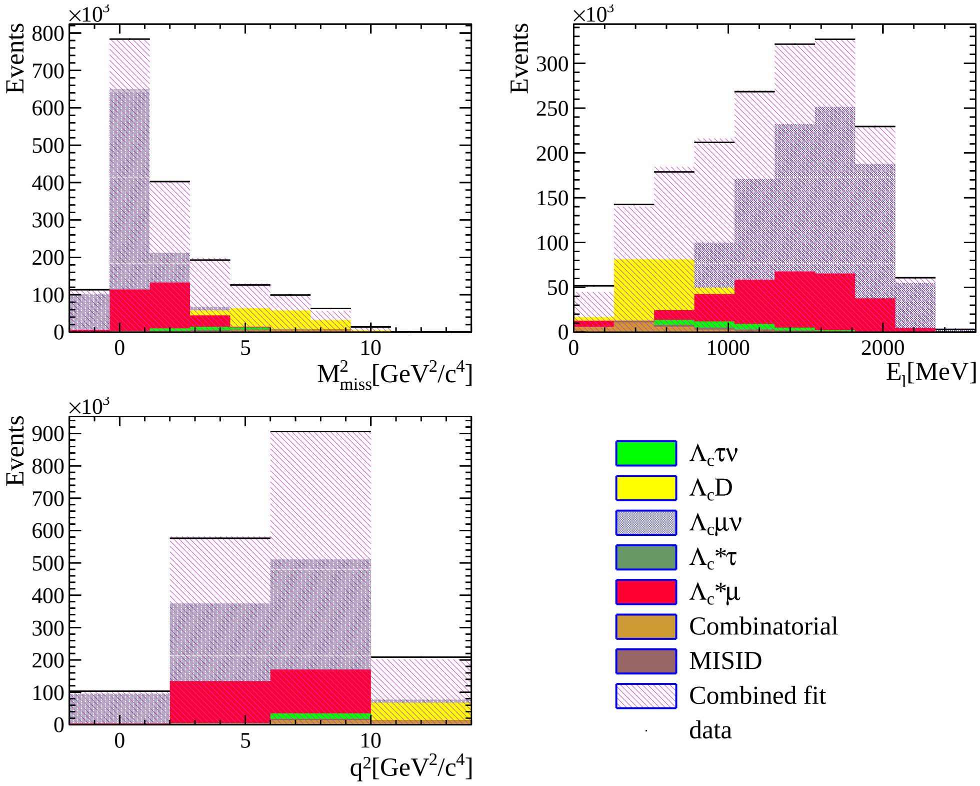

FIGURE 3.9: Applying the fit to the signal region using the pseudodata.

The standard fitting procedure only considers statistical uncertainties arising from the data. We applied the Barlow-Beeston method [80] to include the uncertainties of each template. The difference in uncertainties given by the two methods will show the MC contribution to the uncertainty. $R(\Lambda_c^+)$ and $R(\Lambda_c^+\pi^+\pi^-)$ are anti-correlated and, as we fit them simultaneously, we need to look on uncertainties in the 2D plane. The sensitivity ellipse is depicted in Figure 3.10. The Barlow-Beeston method of the uncertainties evaluation results in $\approx$ 35% higher value of $\sigma_{R(\Lambda_c^+)}$ compared to the standard fitting procedure.

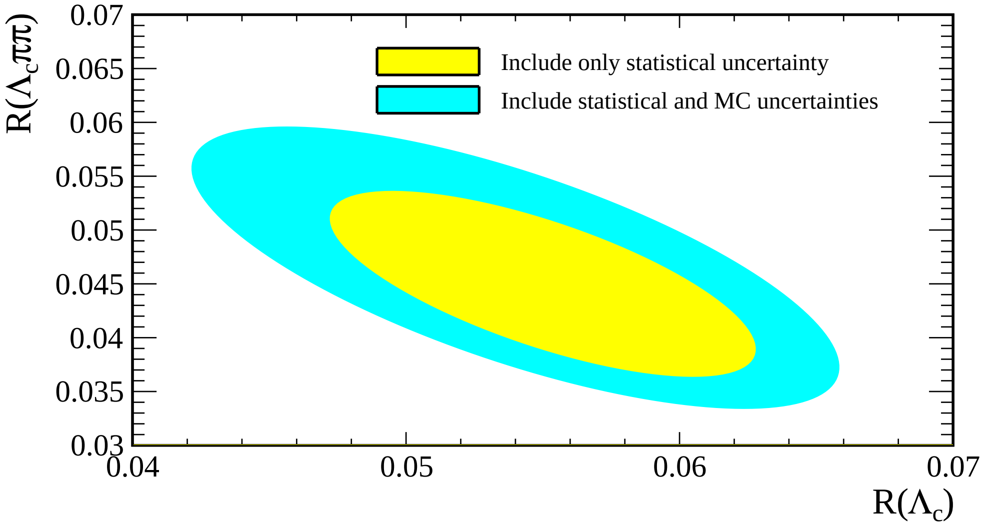

FIGURE 3.10: Sensitivity ellipses of the $R(\Lambda_c^+)$ and $R(\Lambda_c^+\pi^+\pi^-)$ decays using the pseudodata. The yellow colour illustrates results that comprise only statistical uncertainties, the blue - the statistical and MC uncertainties.

We studied the uncertainties on the simulation by generating and fitting 1000 pseudodata samples. $R(\Lambda_c^+)$ distributions for both methods are shown in Figure 3.11. The width of the Gaussian agrees with the uncertainty estimates using the standard fitting. However, it gives $\approx$ 40% higher value for the Barlow-Beeston method. This is a known issue related to bins with small numbers of events [81].

To estimate the uncertainty from the finite size of the simulation we use the following formula for the combination $(\sigma^{WMC})^2 = (\sigma^{MC})^2 + (\sigma^{stat})^2$. From this, we evaluate that the uncertainty from simulation is twice as big as the statistical one in the data. In order to reduce it to the same

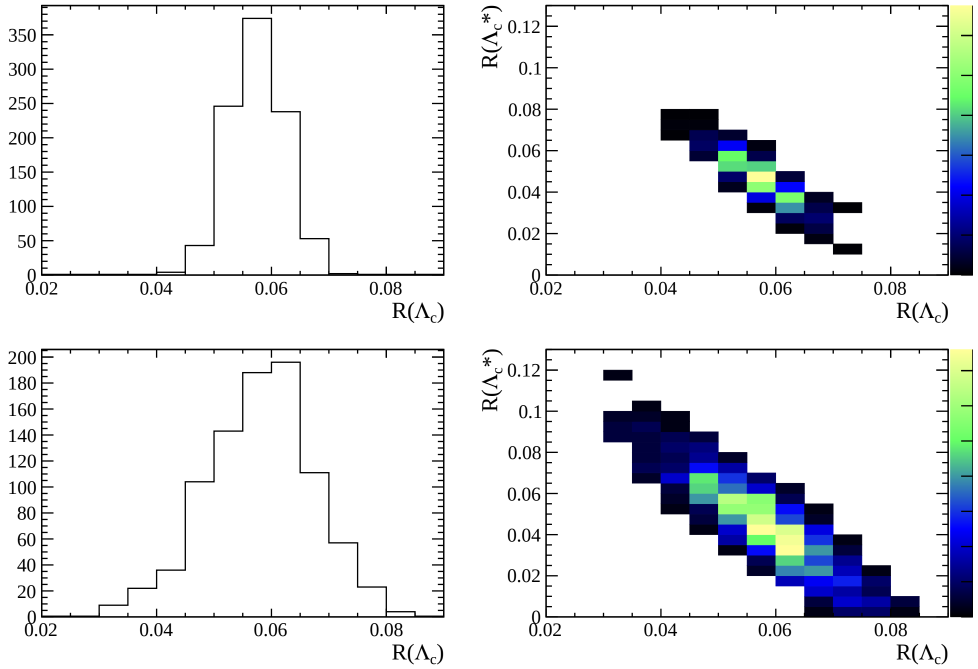

FIGURE 3.11: Distribution of the $R(\Lambda_c^+)$ value for 1000 pseudodata samples using standard fitting (top) and including simulation uncertainties (bottom).

size we need to have an order of magnitude more simulation generated which cannot be achieved with realistic CPU time for the full simulation. We chose to use a fast simulation technique of TrackerOnly simulation as the solution.

TrackerOnly MC is the special fast simulation option of the LHCb software where all systems after the tracker are switched to passive material. It avoids developing showers in the calorimeters and Cherenkov emission in the RICH detector. With TrackerOnly MC, we can generate the same number of events eight times faster and save up to $\approx$ 40% of the disk space compared to full simulation. The disadvantage of the method is that we are missing information from certain detectors. In particular, we don't have a particle identification (PID) or trigger information. While PID can be studied with dedicated control samples, the trigger response must be emulated. We followed the algorithm developed by the ongoing $R(D^+)$ analysis to emulate the first level hadronic trigger and the first level of the software trigger [82].

First level hadronic trigger

The first level (L0) trigger is implemented in hardware [83]. Its main goal is to select particles with high transverse energy and transverse momentum using partial detector information. It can use information from two different systems, depending on which particle we trigger on, either the muon stations or calorimeter systems. However, we cannot use the muon to trigger our events because transverse momentum distribution for muons from signal and normalisation differs and, therefore, we may introduce a bias to our measurements this way. In particular, the softer muon for the tauonic channel implies the triggering on muons would enrich the sample in normalisation mode, rejecting the signal. Instead, we require one of the hadrons in the Λ_c^+ decay (p, K^-, π^+) to fire the L0 trigger. In the case of the full simulation, we select particles with a high transverse energy deposits in the hadron calorimeter (HCAL). Hadronic showers are large meaning that there are overlaps between different clusters which is relatively large compare to HCAL. Therefore, the region of 2×2 cells, that is used, do not contain all the deposited energy and it needs to be accounted in the emulation.

The emulation of the trigger response is done in three sequential steps:

- A simple particle gun method is used to simulate the single pion that provide the response from the HCAL, as a $P - P_T$ function of the pion. The strategy is to look at the difference in the momentum and then to smear the tracker response using that distribution.
- Another particle gun simulation of $D^0 \to K^-\pi^+$ is performed to measure the probability that two HCAL clusters overlap based on their projected positions using the tracking information. Studies

have shown that the overlap probability is higher in the outer region due to the larger cells that exist there.

- A regression BDT is used to correct a disagreement between emulation and full simulation in the low P_T region.
- As the last step, clusters that do not cross the P_T threshold are thrown away.

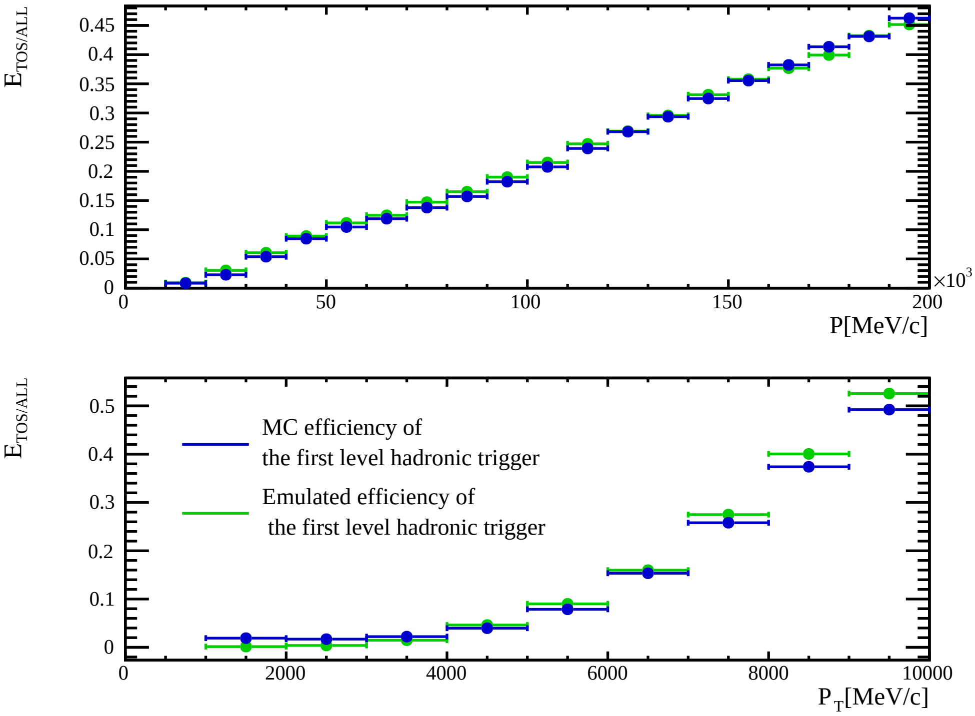

FIGURE 3.12: First level hadronic trigger efficiency as a function of Λ_c^+ momentum (top) and P_T (bottom) for the full simulation (blue) and emulated (green) responses.

The result of the emulation is shown in Figure 3.12. Overall, the emulation shows a good agreement with a full simulation except for the slight difference in the region of low P_T, which is acceptable, as data/simulation agreement is worse in this region anyway.

Independent trigger pathway

The hadron trigger can fire on decay products of the signal (trigger on signal: TOS). Another way to trigger an event is to trigger independently from the signal (TIS) method. In order for an event to be TIS, there must be at least one trigger object which does not have any overlap with the signal. In LHCb, more than 50% of our signal events are normally triggered by TIS [84]. In our analysis, for event to be TIS it can be triggered by any pathway independent of signal. We take this efficiency directly from data, unlike hadronic trigger where we emulate with simulation.

The $B^+ \to J/\Psi K^+$ decay was chosen to calculate TIS efficiency due to the high purity of the channel. An example of the mass peak is shown in Figure 3.13.

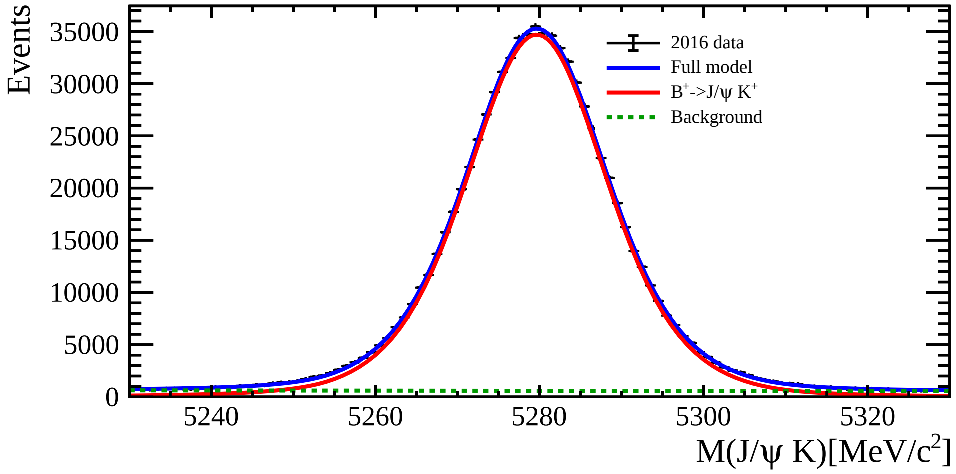

FIGURE 3.13: Fit to the $B^+ \to J/\Psi K^+$ distribution.

The main idea is to transport the TIS efficiency in the bins of the transverse momentum (P_T) and the component of momentum along the beam axis (P_Z) from $B^+ \to J/\Psi K^+$ to our decay.

We build the efficiency of the trigger from the number of events which pass it. However, this can be applied only to MC sample. The reason is that we do not know the initial number of signal events in the data. A generally accepted approach to calculate efficiency in this case is called TISTOS method. The strategy of the method is to apply TIS on events that already have been triggered by TOS. Events that pass this selection are called TISTOS. To estimate the efficiency of the method we need to compare them to events that pass only TOS selection ($\frac{TISTOS}{TOS}$). This efficiency for $B^+ \to J/\Psi K^+$ is shown in Figure 3.14.

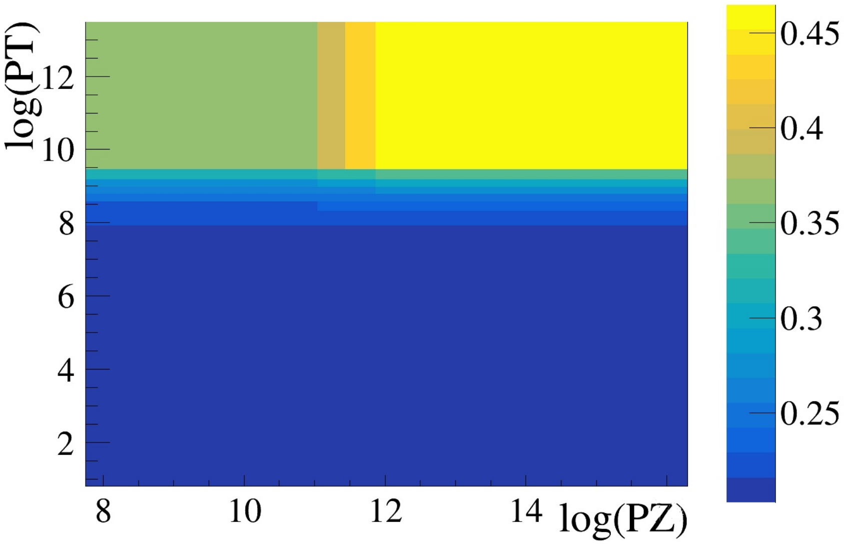

FIGURE 3.14: TIS efficiency for $B^+ \to J/\Psi K^+$ decay from the data in bins of P_Z/P_T using the TISTOS method.

In order to prove that we can apply such approach, we have checked the goodness of the TISTOS method, the portability of the TIS efficiency across different decays and the reproduction quality of TIS efficiency in the simulation.

Assuming that TIS and TOS triggers are independent we can consider that $\varepsilon(\frac{TIS}{ALL}) \approx \varepsilon(\frac{TISTOS}{TOS})$ and, therefore, use $\frac{TISTOS}{TOS}$ efficiency from the data. To validate this approach we compare both methods using J/Ψ simulation sample. The results are depicted in Figure 3.15.

The next aspect we want to verify is the portability between different decays. We compare $\varepsilon(\frac{TIS}{ALL})$ for two simulation samples (Figure 3.16): $B^+ \to J/\Psi K^+$ and $\Lambda_b^0 \to \Lambda_c^+ \mu^- \overline{\nu}_\mu$

As a last step, we want to see how well the TIS trigger is reproduced in MC simulations. For that we compare $\varepsilon(\frac{TISTOS}{TOS})$ of $B^+ \to J/\Psi K^+$ for data and MC samples. Results are shown in Figure 3.17.

We have seen that disagreements between methods, $\varepsilon(\frac{TIS}{ALL})$ and $\varepsilon(\frac{TISTOS}{TOS})$, and two decays,$B^+ \to J/\Psi K^+$ and $\Lambda_b^0 \to \Lambda_c^+ \mu^- \overline{\nu}_\mu$, are much smaller than the difference caused by the mismodelling of MC in comparison to data. The systematic uncertainty associated with the data-simulation disagreement will therefore dominate that arising from the imperfections of the emulation. Hence, the approach can be used for the emulation of TIS trigger in TrackerOnly MC.

The high level trigger

The last trigger that must be emulated is the first part of the High Level Trigger (HLT1) [85]. The trigger consists of a software application which runs on every CPU of the Event Filter Farm (EFF). The HLT1 stage performs a partial event reconstruction and selection, and aims to reduce the input rate of ≈ 1 MHz by a factor of around 20. It selects b-hadron decays by looking for a single high transverse momentum track with a good track fit quality which is well displaced from all primary interactions.

Two selection lines are used in the analysis: HLT1TrackMVA, which fires if one of the tracks in the signal satisfies the selection criteria, and HLT1TwoTrackMVA, which fires if a combination of the two tracks in the signal satisfies the selection criteria

The HLT1TrackMVA line requires a track to have non-linear combination of P_T and of the χ^2 distance of the track to the primary vertex ($IP\chi^2$) above a certain threshold. In addition, the HLT1TrackMVA line requires a set of global cuts to be satisfied, such as the minimum-maximum amount

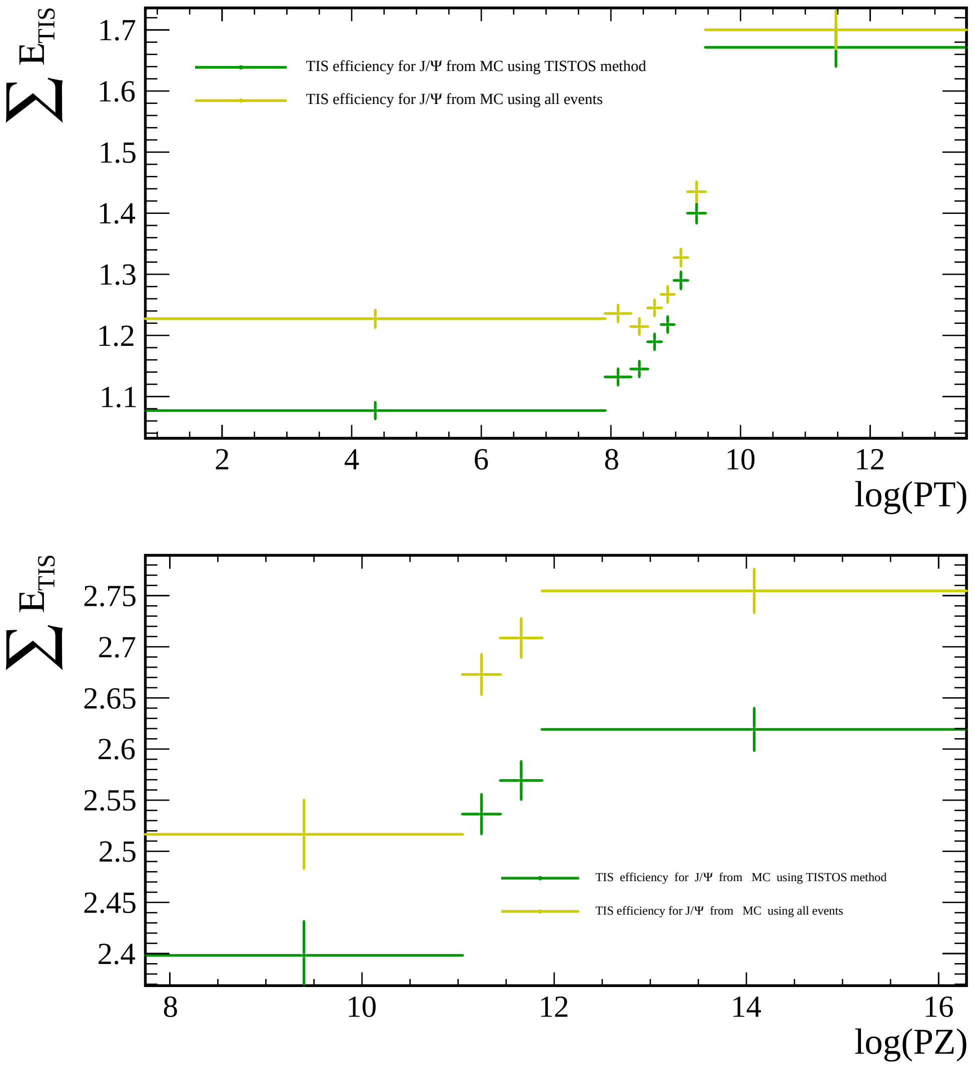

FIGURE 3.15: Validation of TISTOS method for $B^+ \rightarrow J/\Psi K^+$ decay using MC sample.

of clusters in different systems. All cuts demanded by HLT1TrackMVA are shown in the Table 3.4.

variable	requirement
P_T	> 500 MeV$/c$
P	> 3 GeV$/c$
$\chi^2_{track}/N_{d.o.f}$	< 4.0
$\chi^2_{vertex}/N_{d.o.f}$	< 2.5
$log(IP\chi^2)$	$> (\frac{1}{p_T-1})^2 + (\frac{1.1}{25\ \text{GeV}/c - p_T}) + log(7.4)$, where $P_T \leq 25$ GeV$/c$ and $IP\chi^2 \leq 7.4$

TABLE 3.4: HLT1TrackMVA requirements used in the 2016 conditions.

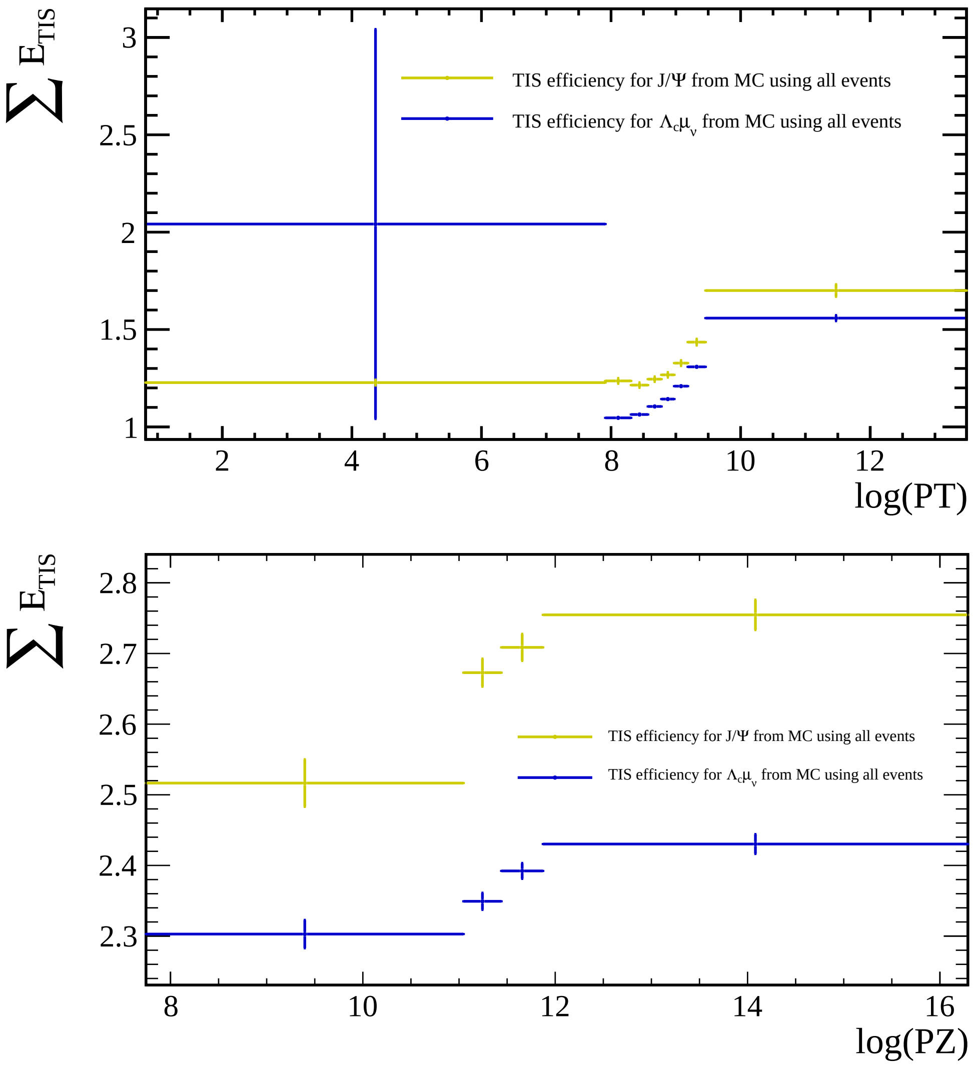

FIGURE 3.16: Validation of the compatibility of TIS efficiencies for $B^+ \to J/\Psi K^+$ and $\Lambda_b^0 \to \Lambda_c^+ \mu^- \nu_\mu$ decays using MC samples.

We also applied a supplementary correction to the final emulation due to the difference of track reconstruction efficiency for offline and online tracks [86]. We used the relative efficiency to real L0 trigger response, in order to estimate the pure performance of HLT1Track emulation, which shows a good agreement (see Figure 3.4).

A similar procedure is applied to emulate the HLT1TwoTrackMVA response. The difference here is that in addition to the selection on each track we introduce a complementary selection on the combination of

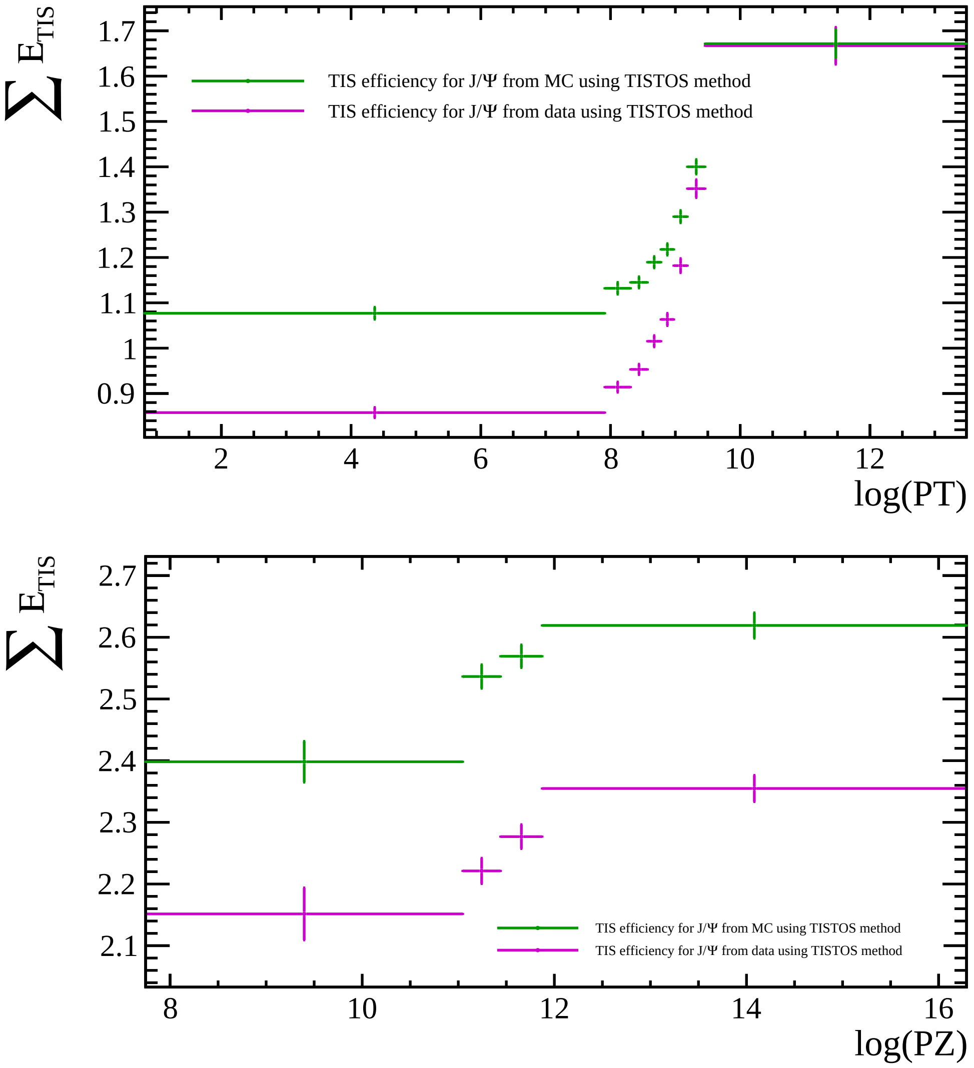

FIGURE 3.17: Comparison of $\varepsilon(\frac{TISTOS}{TOS})$ of the $B^+ \to J/\Psi K^+$ decay for the data vs. MC samples.

two tracks in the event. The HLT1TwoTrackMVA trigger selects events using MatrixNet, a machine learning algorithm based on gradient boosting [87]. Input variables for classifier are the scalar sum of the P_T of the two tracks and $IP\chi^2$. Emulation cuts for the HLT1TwoTrackMVA trigger are listed in table 3.5, where the variables are defined as:

- M_{corr} is a corrected mass of the two tracks combination using the primary vertex and the missing momentum transverse to the direction of flight.

- χ^2_{DOCA} is the χ^2 of the distance of closest approach of two tracks.

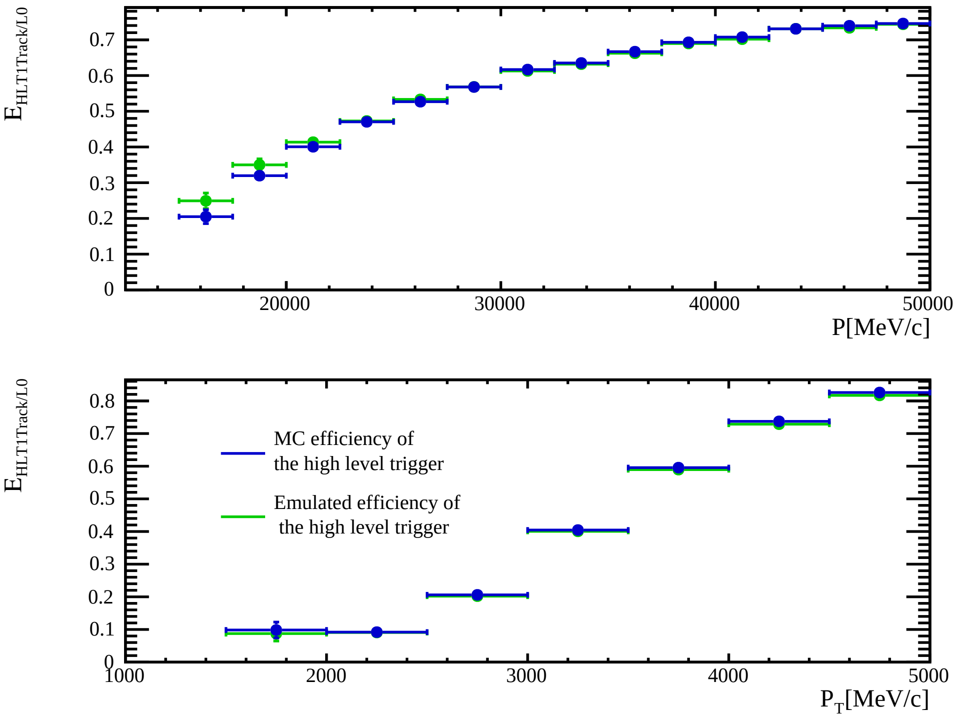

FIGURE 3.18: HLT1TackMVA efficiency as a function of the Λ_c^+ transverse momentum in $\Lambda_b^0 \to \Lambda_c^+ \mu^- \overline{\nu}_\mu$ decays. Emulation is illustrated in green, with the full simulation response in blue.

- *MVA* is an output of the MatrixNet classifier.

Single track requirements	$P_T > 0.6\ \mathrm{GeV}/c$ $P > 5.0\ \mathrm{GeV}/c$ $\chi^2_{track}/N_{d.o.f} < 2.5$
Track pair requirements	$(p_1 + p_2)_T > 2\ \mathrm{GeV}/c$ $\chi^2_{DOCA} < 10$ $\chi^2_{vertex} < 10$ $M_{corr} > 1\ \mathrm{GeV}/c^2$ $2 < \eta < 5$ $DIRA > 0$ $MVA > 0.95$

TABLE 3.5: HLT1TwoTrackMVA requirements used in the 2016 conditions.

The emulation efficiency of HLT1TwoTrackMVA is calculated with respect to the L0 trigger response and is depicted in Figure 3.19.

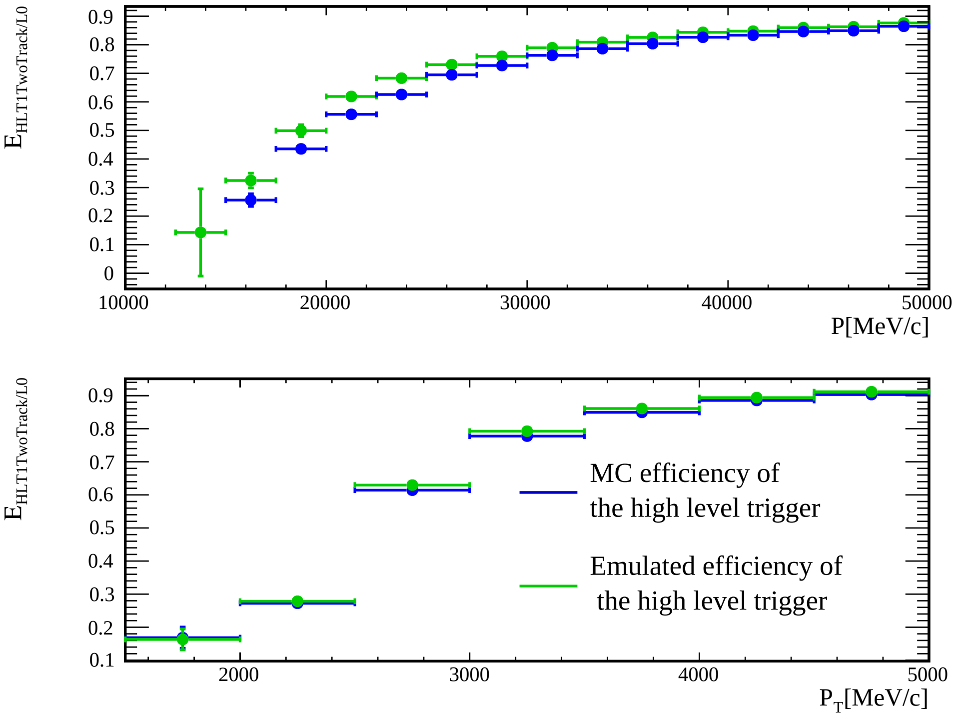

FIGURE 3.19: HLT1TwoTrackMVA efficiency as a function of the Λ_c^+ transverse momentum (bottom) and momentum (top) in $\Lambda_b^0 \to \Lambda_c^+ \mu^- \overline{\nu}$ decays. Emulation is illustrated in green, with the full simulation response in blue.

3.4.2 Corrections to simulation

The measurement of $R(\Lambda_c^+)$ relies heavily on the simulated distributions for different components. However, simulation is extremely time consuming and are based only on our current knowledge. They must be corrected according to known mismatches with real data and updated with the newest calculations. In case of the $\Lambda_b^0 \to \Lambda_c^+ \ell^- \overline{\nu}_\ell$ decay, the following issues must be accentuated for:

- Usage of outdated form-factor predictions.
- Inaccurate distributions of the Λ_b^0 production kinematics.
- Mismodelling of the PID response.

Form-factor correction from Lattice QCD

In the SM, the decay rate to the different channels can be expressed with the effective weak Hamiltonian for $b \to q\ell\nu_\ell$ transitions ($q = c$),

$$\mathcal{H}_{eff} = \frac{G_F}{\sqrt{2}} V_{qb} \left(\bar{q}\gamma^\mu b - \bar{q}\gamma^\mu\gamma_5 b\right) \bar{\ell}\gamma_\mu(1-\gamma_5)\nu,$$

where the hadronic matrix elements of the vector ($\bar{q}\gamma^\mu b$) and axial ($\bar{q}\gamma^\mu\gamma_5 b$) vector currents can be expressed through six form-factors.

The G_F denotes the Fermi coupling constant and V_{qb} is the Cabibbo-Kobayashi-Maskawa (CKM) matrix element amplitude that is needed to calculate form-factors.

The most precise form-factors calculations for $\Lambda_b^0 \to \Lambda_c^+\ell^-\bar{\nu}_\ell$ decays are performed using lattice gauge theory [88]. Lattice QCD is a well-established non-perturbative approach to solving the quantum chromodynamics theory of quarks and gluons. It is a lattice gauge theory formulated on a grid or lattice of points in space-time. The finite size of the momentum grid means that hadrons with large momentum are statistically limited. This means that the calculations are more precise for higher q^2 regions.

The form-factor predictions affect the kinematic distributions of the decay including both, q^2 and helicity angle. However, the largest effect seen in the analysis is in the q^2 distribution, therefore for simplicity we perform 1D corrections in q^2. The q^2 predictions for signal and normalisation channels is shown in Figure 3.20.

A comparison of the q^2 distributions between the latest lattice QCD predictions and the model used in the simulation is shown in Figure 3.21. While the signal is mostly not affected by the new form-factor calculations, the normalisation channel has a slight energy shift to higher q^2

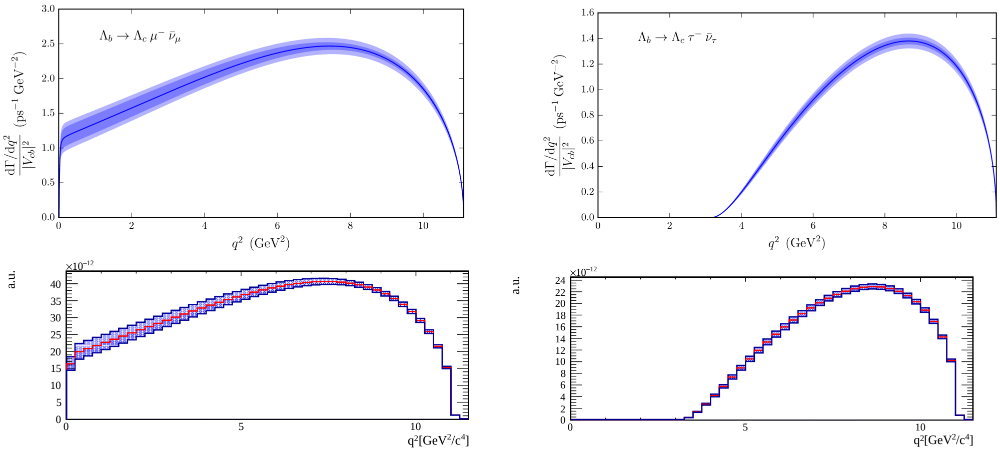

FIGURE 3.20: Predictions for the q^2 distributions for $\Lambda_b^0 \to \Lambda_c^+ \mu^- \overline{\nu}_\mu$ (left) and $\Lambda_b^0 \to \Lambda_c^+ \tau^- \overline{\nu}_\tau$ (right) in the Standard Model using form-factors from lattice QCD with relativistic heavy quarks. Top is taken from Ref. [88], bottom - reproduced using paper calculations.

with respect to the simulated sample.

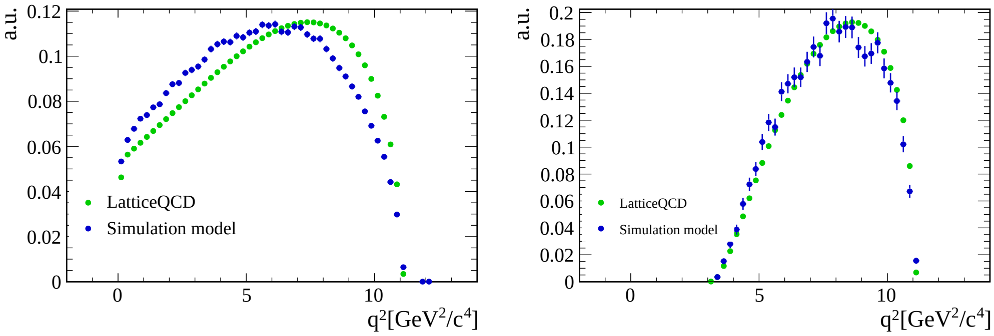

FIGURE 3.21: Comparison of the q^2 distributions for $\Lambda_b^0 \to \Lambda_c^+ \mu^- \overline{\nu}_\mu$ (left) and $\Lambda_b^0 \to \Lambda_c^+ \tau^- \overline{\nu}_\tau$ (right) predicted by lattice QCD and those of the simulated samples.

The fit variables $M^2_{missing}$,E^*_μ and q^2 must be corrected based on the difference we observe in the underlying true q^2 distribution. The fit variables are reweighted to the form-factor predictions and are shown in Figure 3.22. As expected, q^2 is most affected by the correction, the other two fit variables remain almost unchanged. The corrections are added to the fit and also include uncertainties on the form-factors represented with a shape variation.

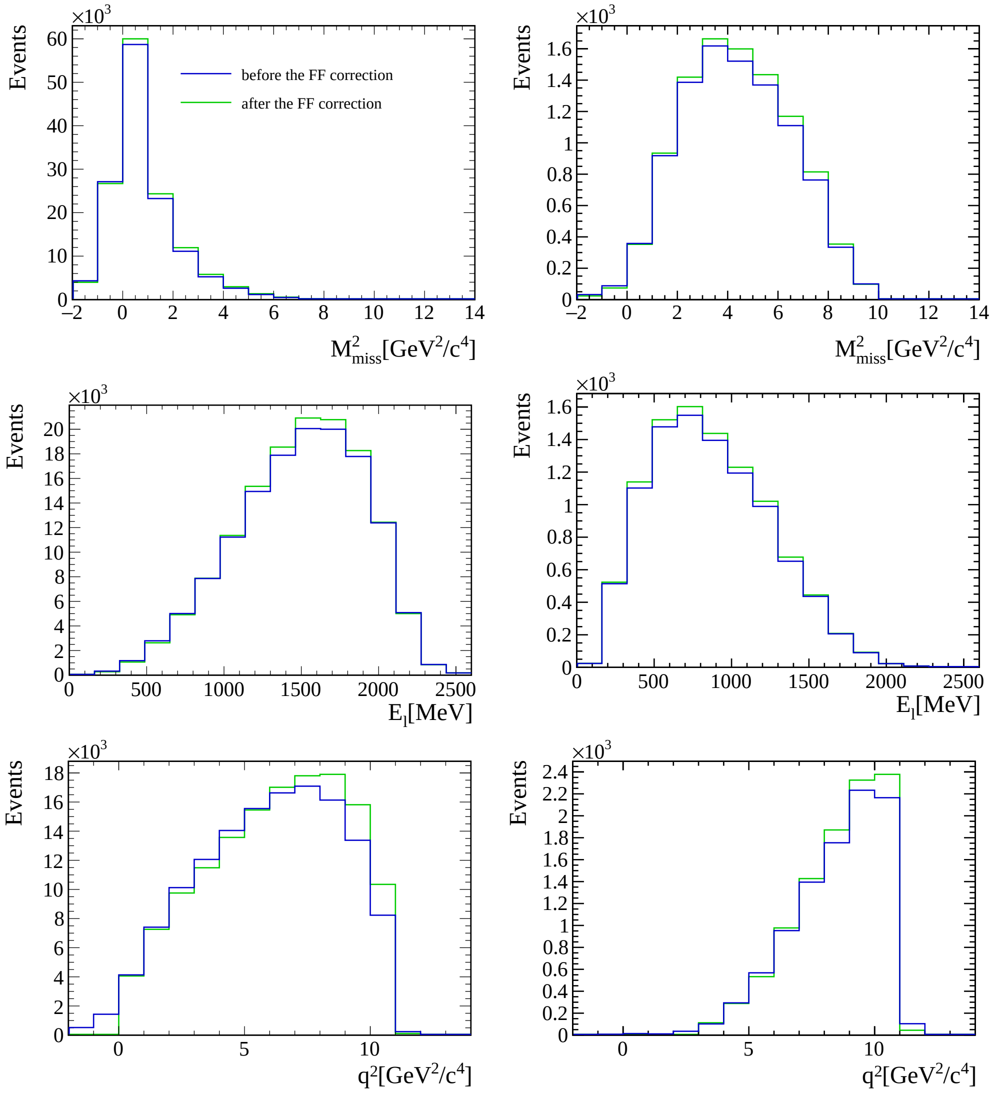

FIGURE 3.22: Fit variables before and after the reweighting to the latest form factor predictions for $\Lambda_b^0 \to \Lambda_c^+ \mu^- \overline{\nu}_\mu$ (left) and $\Lambda_b^0 \to \Lambda_c^+ \tau^- \overline{\nu}_\tau$ (right).

Correction of the Λ_b^0 production kinematics

It was seen in previous studies that the measured momentum and transverse momentum distribution of Λ_b^0 production doesn't agree with simulation in LHCb [89]. The correction is done in bins of P_T and pseudorapidity η. The correction scheme is taken from Ref. [90] using $\Lambda_b^0 \to pK^- J/\Psi(\to \mu^+\mu^-)$ candidates passing the L0Muon trigger requirement, meaning that tracks must pass five muon stations and have a transverse momentum above a predefined threshold of 1.7 GeV$/c^2$ for 2016 data.

The correction scheme is shown in Figure 3.23. The momentum distributions of the Λ_b^0 for the muonic sample before and after the correction are shown in Figure 3.24. Even after the production corrections, the transverse momentum and momentum agreement is poor. This can be explained by a mismodelling of the trigger between data and simulation. For example, the hadronic trigger is known to not be well reproduced in the simulation and strongly depends on the kinematics of the Λ_c particle. For this reason, a further correction is applied in Section 3.4.3.

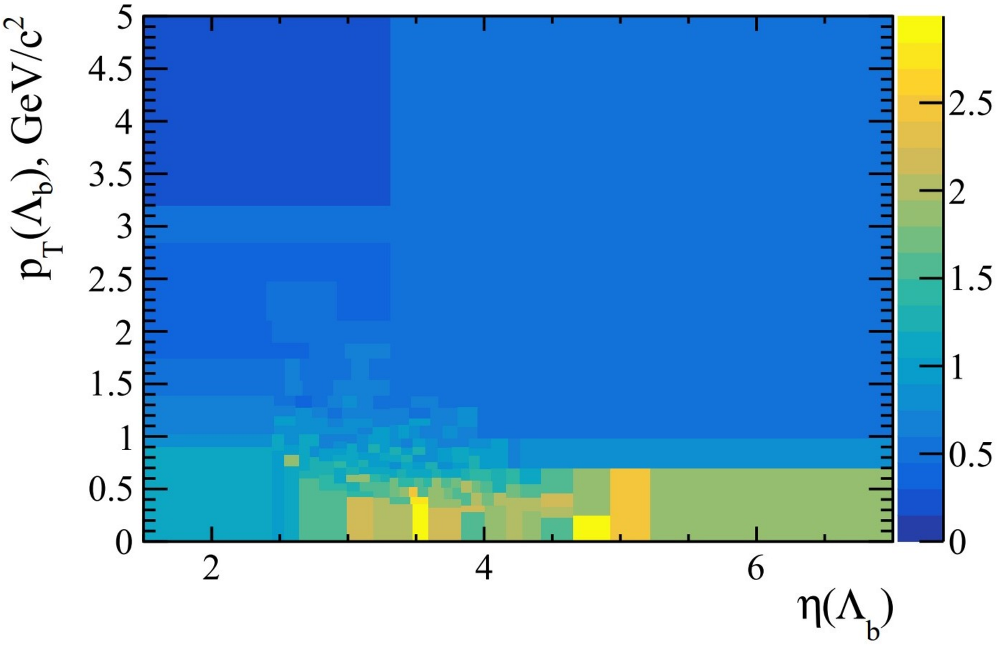

FIGURE 3.23: Ratio of kinematic distributions between data and simulation for the Λ_b^0 production correction [90].

PID response

An excellent particle identification (PID) performance is crucial for the analysis, in particular for the $h \to \mu$ misid background estimation. However, it is not trivial to simulate the PID algorithm and it was seen in previous measurements that PID is badly modelled in the simulation [91]. At LHCb, a data-driven technique is performed to correct for the disagreement of the PID efficiencies between data and simulation. The idea

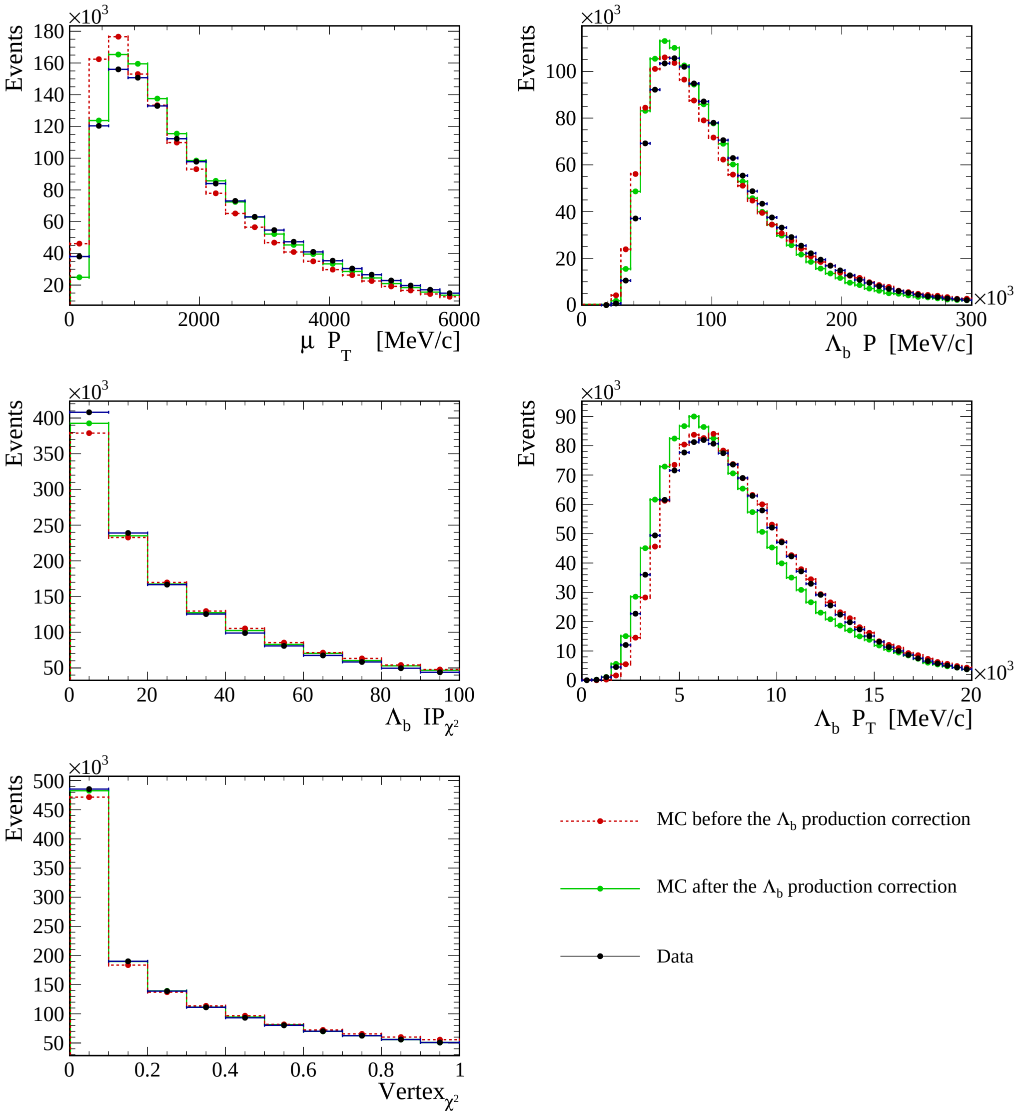

FIGURE 3.24: Effect on the different kinematic distributions after the Λ_b^0 production kinematic correction.

is to use calibration samples of K, π, p and μ without using any PID selection. The PIDCalib package was used to compute the efficiency of particle identification selection requirements [92]. K, p, π and μ candidates are selected with high purity from high yield samples using only kinematic information to estimate the PID performance from data. The $J/\Psi \to \mu^+\mu^-$ decay was used for the muon calibration sample, which is selected by requiring the muon candidates to have a high impact parameter (IP) with respect to the primary vertex and the reconstructed J/ψ

to have a large flight distance significance and good decay vertex quality [93]. The $D^{*+} \to D^0(\to K^-\pi^+)\pi^+$ decay was used for the pion and kaon calibration samples, while the $\Lambda_c^+ \to pK^-\pi^+$ decay was used for the proton calibration sample[94]. The residual background in all samples are removed through the use of the sPlot technique [95].

The PIDCalib package provides the PID response as a function of the track multiplicity, the pseudorapidity of the track and its momentum. This response is applied to our simulation in bins of these variables to account for kinematic and multiplicity differences between the calibration sample and our decays of interest.

3.4.3 Multidimensional correction to simulation based on data

Ideally, the simulation would perfectly reproduce real data. Unfortunately, there are still residual data-simulation discrepancies which must be corrected for. To this end, we compare a mixture of our simulation samples with their fractions determined from an initial fit to data. The kinematic and geometrical variables of this mixture are then compared between data and MC. We perform all comparisons in the low missing mass square region ($M_{miss}^2 < 3\ \text{GeV}^2/(c^4)$) to minimise the contribution from the signal in this comparison. The list of variables and particles used is presented in Table 3.6. An example of such a comparison for the pion candidate is shown in Figure 3.25 and the Λ_b^0 candidate in Figure 3.26. The distributions for other particles can be found in the Appendix.

Overall, the MC and data distributions agree with each other which indicates that the simulation is well-modelled. Variables that have the biggest disagreement are used as input to a multivariate reweighter [96]

Particle	Variables
μ^-	$P, P_T, IP\chi^2, IP, \eta$
p	$P, P_T, IP\chi^2, IP, \eta$
K^-	$P, P_T, IP\chi^2, IP, \eta$
π^+	$P, P_T, IP\chi^2, IP, \eta$
Λ_c^+	$P, P_T, IP\chi^2, IP, \eta$
Λ_b^0	$DIRA, \chi^2_{vertex}$

TABLE 3.6: List of variables and particles used to compare MC samples with the data.

in order to correct these disagreements. These are momentum, transverse momentum and $IP\chi^2$ of the Λ_c^+ particle, and $DIRA$ of the Λ_b particle. The distributions of variables before and after the reweightening are shown in Figure 3.27. A residual discrepancy between the simulation model and data is still observed. This will be tuned with the fit results at the final stage of the analysis. Figure 3.28 shows the effect of the MC correction on the fit kinematic variables.

3.5 Estimation of backgrounds

As mentioned previously, three fit variables are chosen to separate the signal and normalisation decays and to determine the parameters of interest $R(\Lambda_c^+)$ and $R(\Lambda_c^+\pi^+\pi^-)$. When fitting the kinematic variables, it is necessary to account for the presence of background contributions, in addition to the signal and normalisation processes. Background contributions can originate from different reasons, but mostly they originate from missing or the misidentification of particles.

3.5.1 Combinatorial background

In our case, combinatorial background mostly arises when we correctly reconstruct the Λ_c^+, but mistakenly combine a muon from an unrelated process. A schematic is shown in Figure 3.29.

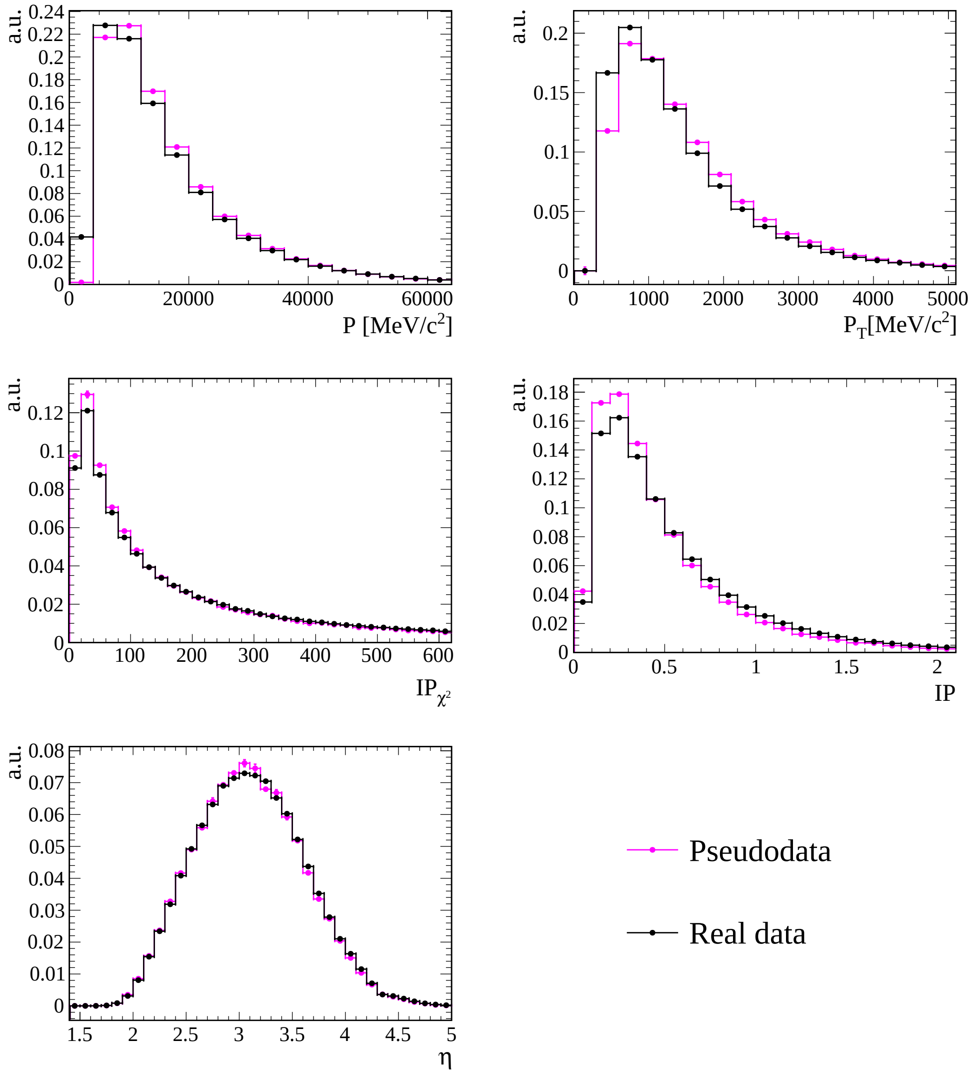

FIGURE 3.25: Simulation - data comparison for the pion distributions.

This type of background cannot be modelled with simulation samples and therefore must be taken from data. The technique used to estimate the contribution of the combinatorial background is based on the assumption that this background should occur independently from the particle charge. Therefore, we can assume that combinatorial background will be similar to the the $\Lambda_c^+ \mu^+$ pairs contribution in data. We take template shapes for our fit from these "same sign" combinations. As the last step, we compare the shapes for the same sign and opposite sign contributions in the Λ_b^0 mass sideband region to prove the validity of the

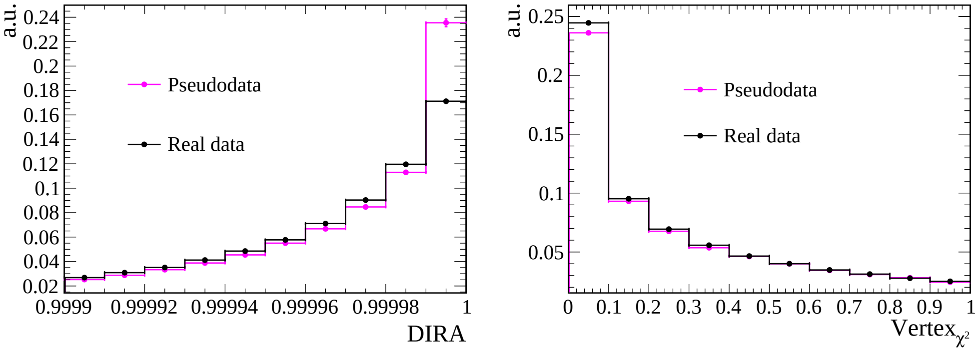

FIGURE 3.26: Simulation - data comparison for the Λ_b^0 distributions.

method, which show a good agreement. The template shapes for the combinatorial background are shown in Figure 3.30. The estimated contribution to the fit is 3.2% with respect to all $\Lambda_b^0 \to \Lambda_c^+ \mu^- \overline{\nu}_\mu X$ decays.

3.5.2 Misidentification background

Misidentification background occurs when a pion or a kaon is wrongly identified as a muon (see Figure 3.31).

The misidentification background cannot be taken from simulation since PID is not well simulated and is estimated, similarly to the combinatorial background, from data. For this we use a sample where we do not require a positive muon identification in the reconstruction and trigger levels. After the selection of this sample, the procedure can be split into 3 steps:

- First of all, we split the misid sample into two datasets: a $\Lambda_c^+ K^-$ sample, where we require a Λ_c^+ candidate to be combined with a kaon, and a $\Lambda_c^+ \pi^-$ sample, where we require a Λ_c^+ candidate to be combined with a pion. All events are weighted according to their properties (number of tracks, pseudorapidity, momentum).
- The kaon and pion samples are first assumed to consist of pure

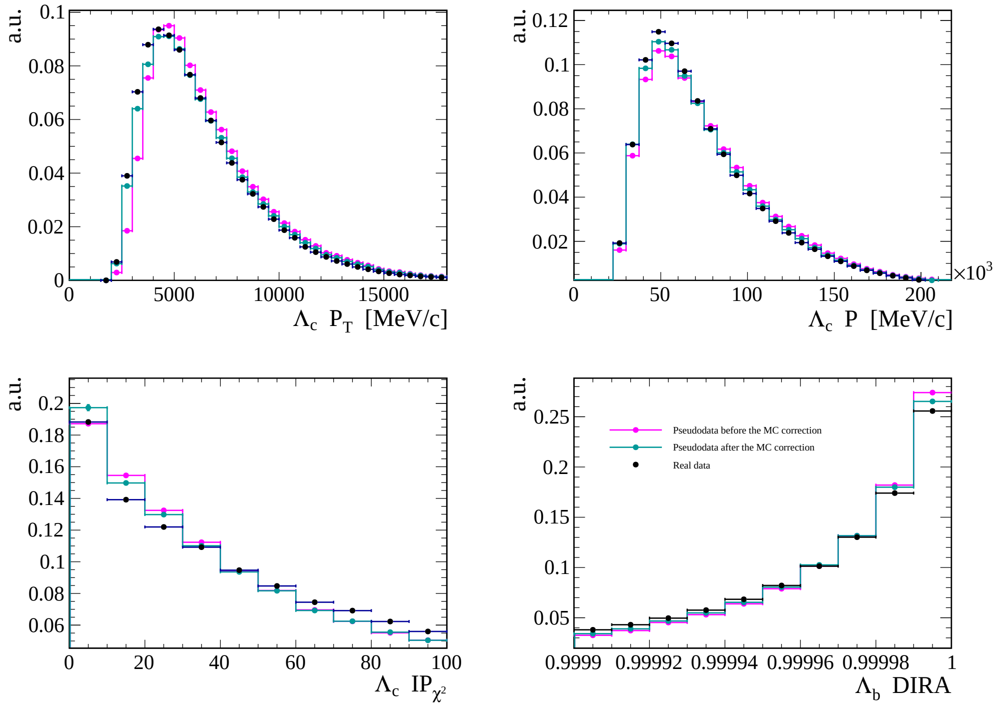

FIGURE 3.27: Kinematic and geometrical distributions before and after the correction of the simulation model with data distributions.

kaons and pure pions. We then use this assumption to take into account the imperfect K^--π^- identification and calculate the cross-feed from the pion (kaon) sample into the kaon (pion) sample: In bins of kinematics, we use dedicated PID calibration samples which estimate misidentification rate for a given pion (kaon) to leak into the kaon (pion) sample.

- We create fit templates for the misid background from these samples taking into account the cross-feed of $\pi^- \longleftrightarrow K^-$.

The contribution due to the misid of decays of the type $\Lambda_b^0 \to \Lambda_c^+ K^-$ is estimated to be 0.33% with respect to the inclusive sample, whereas background contributions from $\Lambda_b^0 \to \Lambda_c^+\pi^-$ decays is estimated to be 2.6% with respect to the full sample. The shapes of these backgrounds as a function of the fit variables are shown in Figure 3.32.

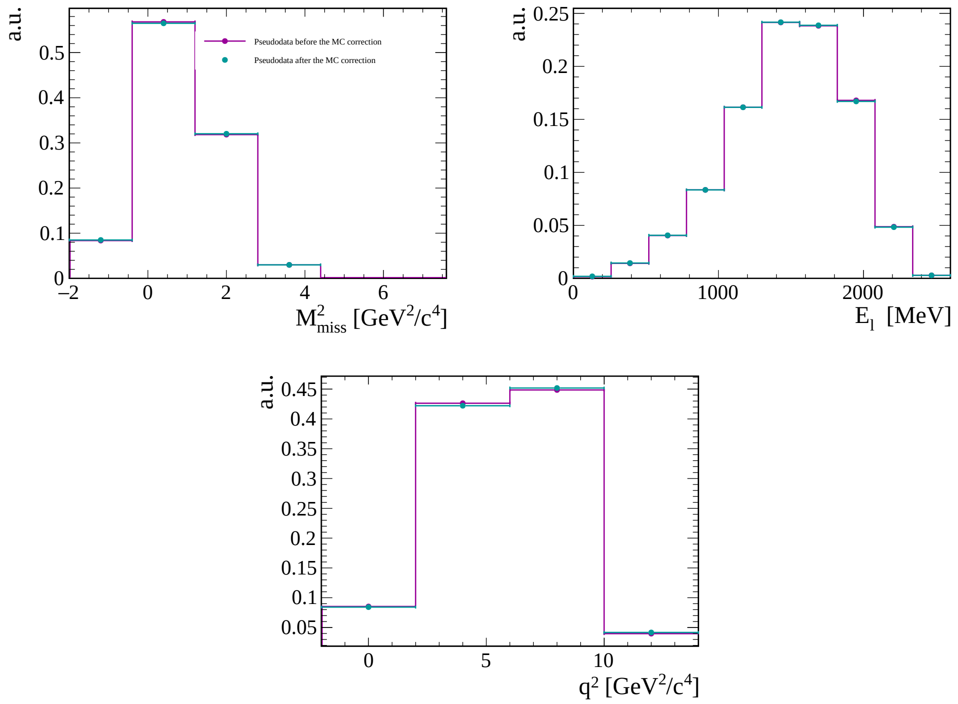

FIGURE 3.28: Fit variables distributions before and after the correction of the simulation model with data distributions.

3.5.3 Double-charm background

Another source of dangerous background originates from decays of the type $\Lambda_b^0 \to \Lambda_c^+ X_c$, where X_c is a charmed hadron that decays in a final state with a muon mimicking that from a τ^- decay. This is referred to as double-charm background due to the fact that these decays contain at least two hadrons containing a charm quark. We can see the distribution of particles from the simulation sample that mimic a signal in Table 3.7.

We utilise a multivariate algorithm (MVA) isolation tool that was developed for the $R(D^{*+})$ analysis [77] to select this double-charm background. The feature of this background exploited by this tool is the presence of at least one additional reconstructible particle in the proximity of the b vertex. The algorithm evaluates the likelihood for each track in the event originates from the reconstructed Λ_b^0 vertex. An output of the isolation BDT distribution for the signal and the double-charm background

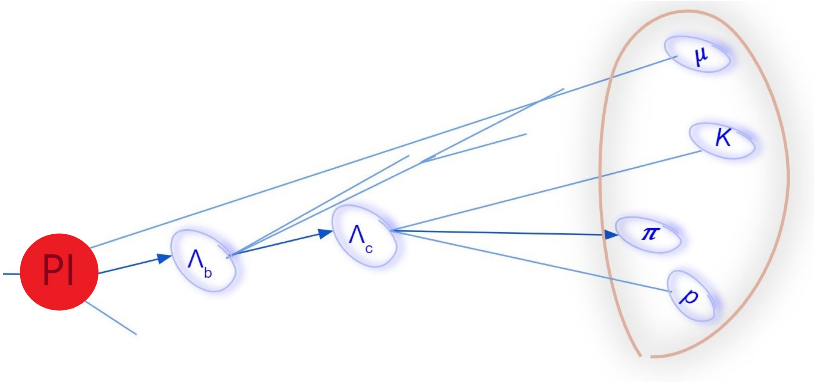

FIGURE 3.29: Schematic of the process that causes combinatorial background. PI indicates the primary interaction.

	Two body decay, %	Three body decay, %
$D^*(2007)^0$	$4.4 \cdot 10^{-3}$	33.3
$D^*(2010)^+$	$6.9 \cdot 10^{-3}$	23
D_s^{*+}	16.5	$16.6 \cdot 10^{-3}$
$D_{s1}(2460)^+$	9.8	0
D_s^+	7.9	$17.8 \cdot 10^{-3}$
D^0	$6.6 \cdot 10^{-3}$	6.4
D^+	$7.5 \cdot 10^{-3}$	3
$D_{s0}(2317)^+$	$3.7 \cdot 10^{-3}$	0
$D_{s1}(2356)^+$	$0.4 \cdot 10^{-3}$	0
$D_{s2}(2460)^+$	0	10^{-5}
Total	≈ 66	≈ 34

TABLE 3.7: List of particles that produce the $\Lambda_c^+ X_c$ background.

is depicted in Figure 3.33. We use this isolation variable later to define control samples.

3.5.4 Background originating from excited states

The final background class we consider arises from excited states of Λ_c^+. Instead of the signal decay $\Lambda_b^0 \to \Lambda_c^+ \tau^-(\mu^-)\overline{\nu}_{\tau(\mu)}$, we detect the decay to the excited state $\Lambda_b^0 \to \Lambda_c^{*+} \tau^-(\mu^-)\overline{\nu}_{\tau(\mu)}$, where $\Lambda_c^* \to \Lambda_c \pi^+ \pi^-$. We estimate this background contribution using simulated samples for the most common excited states. The list of excited states used is shown in Table 3.8. The combination of this feeddown background corresponds to $\sim 26\%$ of the yield in the inclusive $\Lambda_b^0 \to \Lambda_c^+ \mu^- X$ peak.

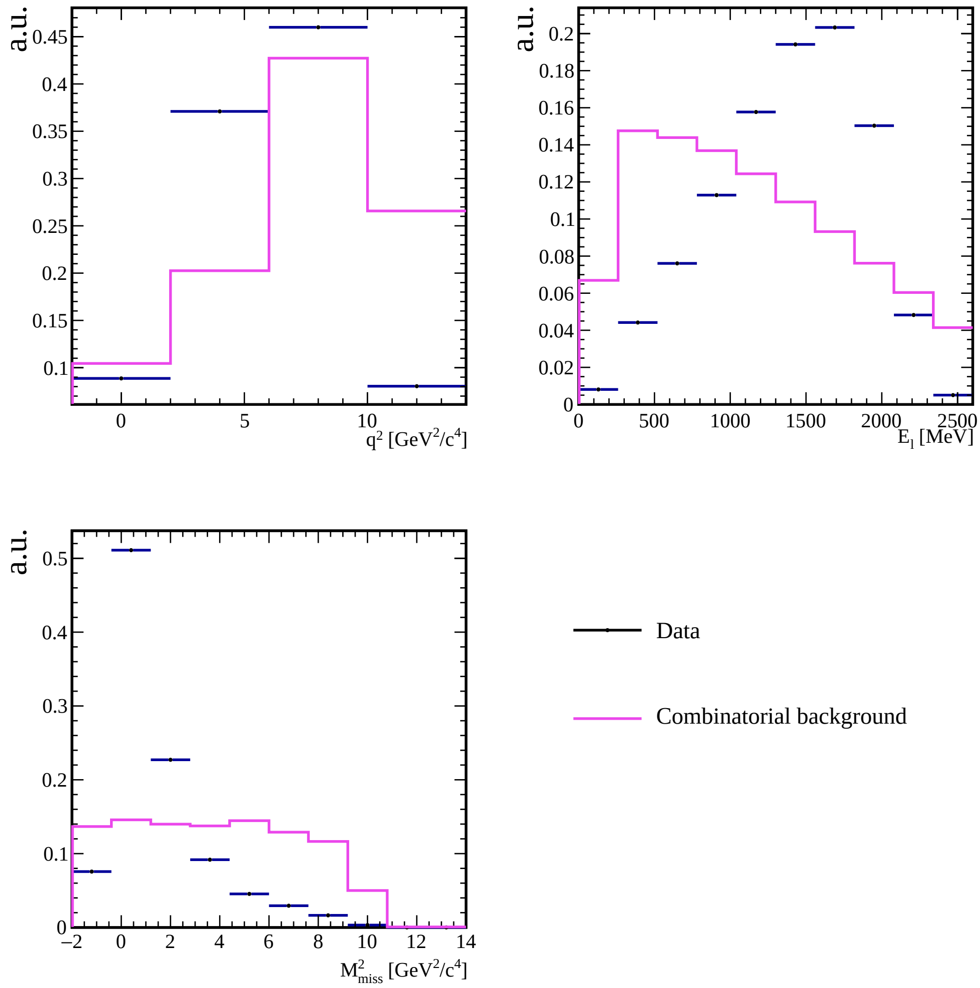

FIGURE 3.30: Template shapes of kinematic variables for the combinatorial background overlaid with the full data template.

Types of the decay	$\Lambda_b^0 \to \Lambda_c^{*+}\tau^-\overline{\nu}_\tau$ $\Lambda_b^0 \to \Lambda_c^{*+}\mu^-\overline{\nu}_\mu$
Excited states	$\Lambda_c^{*+}(2595) \to \Lambda_c^+\pi^+\pi^-$ $\Lambda_c^{*+}(2625) \to \Lambda_c^+\pi^+\pi^-$ $\Lambda_c^{*+}(2765) \to \Lambda_c^+\pi^+\pi^-$ $\Lambda_c^{*+}(2880) \to \Lambda_c^+\pi^+\pi^-$

TABLE 3.8: List of highest branching fraction rates excited states of Λ_c^+ that were used to estimate the contribution of background from excited Λ_c^+ states.

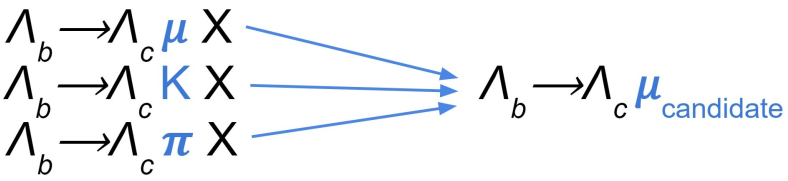

FIGURE 3.31: Diagram illustrating the various contributions including real muons and misid background to our data sample.

3.6 Blinding strategy

The value of $R(\Lambda_c^+)$ and $R(\Lambda_c^+\pi^+\pi^-)$, is blinded in order to avoid any human factors and subconscious biases in the final fit result. The blinding is implemented in the following way:

$$(-1)^\alpha \cdot \beta \cdot R(\Lambda_c^{(*)+}) + \gamma,$$

where α, β, γ are randomly generated values within the range of 0 to 100. This ansatz is chosen to avoid the sign of $R(\Lambda_c^+)$ to be known.

3.7 Likelihood fits

We use multidimensional binned maximum likelihood fit to the three fit variables to determine the parameters of interest $R(\Lambda_c^+)$ and $R(\Lambda_c^+\pi^+\pi^-)$. The fit is performed in three different regions:

- Isolated region

  - No tracks pass the isolation criteria, which means that there is no additional track with an isolation BDT value higher than 0.35.

- Double-charm region

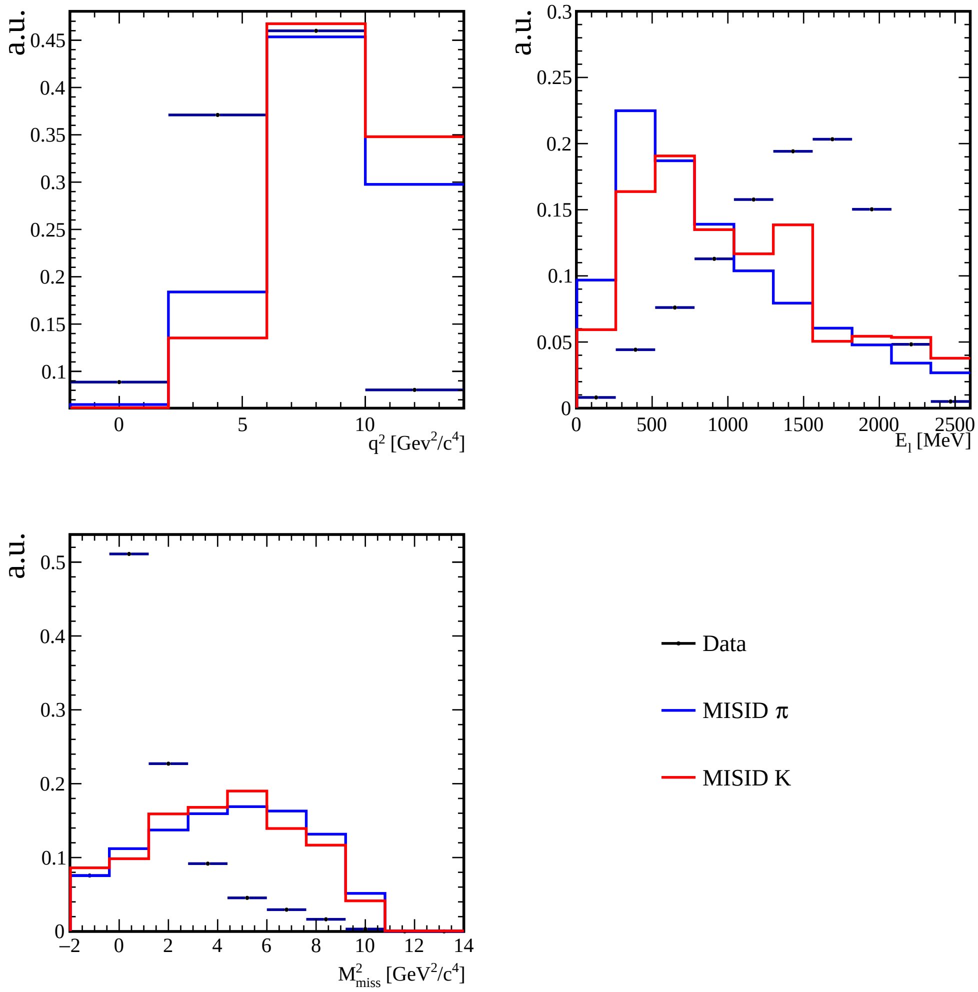

FIGURE 3.32: Shape in the fit variables for the background originating from $(h \to \mu)$ misid.

- Two additional tracks are compatible with the Λ_b^0 decay vertex due to decay chain $\Lambda_b^0 \to \Lambda_c^+ X_c (X_c \to K\mu^-\overline{\nu}_\mu X)$.
- Both tracks are long tracks.
- Both tracks have ProbNNghost<0.2, where ProbNNghost is a special variable used in LHCb to estimate the probability of the track being fake (consisting of hits that do no belong to the same track). It is obtained as an output of neural network-based classifiers that take into account the track kinematics and the tracking performance [92].
- At least one out of two tracks identified as a kaon by

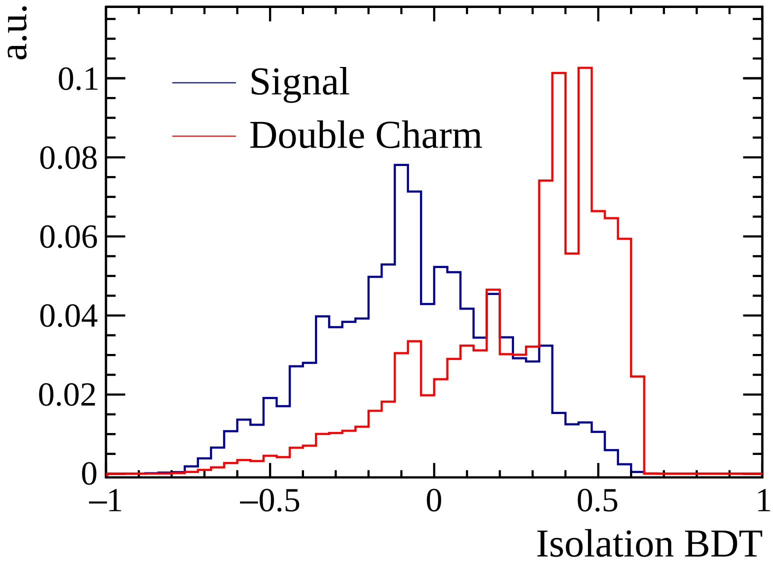

FIGURE 3.33: Comparison of isolation BDT variable for the signal ($\Lambda_b^0 \to \Lambda_c^+ \tau^- \overline{\nu}_\tau$) and double-charm ($\Lambda_b \to \Lambda_c X_c$) decays.

the particle identification system.

- Events that satisfy $\Lambda_c^+ \pi^+ \pi^-$ region requirements are excluded.

- $\Lambda_c^+ \pi^+ \pi^-$ region

  - Two additional tracks are compatible with the Λ_b^0 decay vertex due to the decay chain $\Lambda_b^0 \to \Lambda_c^{*+} \mu^- \overline{\nu}_\mu (\Lambda_c^{*+} \to \Lambda_c^+ \pi^+ \pi^-)$.

  - Both tracks are long tracks.

  - Both tracks have ProbNNghost<0.2.

  - Two tracks have opposite charges.

  - The invariant mass of two tracks together with the Λ_c^+ candidate should be less than 2700 MeV.

A summary of the fit templates used in the fit are shown in Table 3.9.

Monte-Carlo derived templates	Data derived templates
$\Lambda_b^0 \to \Lambda_c^+ \tau^- \overline{\nu}_\tau$	combinatorial misid
$\Lambda_b^0 \to \Lambda_c^+ \mu^- \overline{\nu}_\mu$	
$\Lambda_b^0 \to \Lambda_c^{*+}(2595, 2625, 2765, 2880)\tau^- \overline{\nu}_\tau$	
$\Lambda_b^0 \to \Lambda_c^{*+}(2595, 2625, 2765, 2880)\mu^- \overline{\nu}_\mu$	
$\Lambda_b^0 \to \Lambda_c^{(*)+} X_c$	

TABLE 3.9: List of background and signal templates used in the fit.

The fit is done simultaneously to all three regions. The fit nuisance parameters are summarised in Table 3.10. Parameters of interest are $R(\Lambda_c^+)$ and $R(\Lambda_c^+ \pi^+ \pi^-)$.

Fixed
N($\Lambda_b^0 \to \Lambda_c^+ \mu^- \overline{\nu}_\mu$)
N($\Lambda_b^0 \to \Lambda_c^{*+}(2595, 2625, 2765, 2880)\tau^- \overline{\nu}_\tau$)
N($\Lambda_b^0 \to \Lambda_c^{*+}(2595, 2625, 2765, 2880)\mu^- \overline{\nu}_\mu$)
N($\Lambda_b^0 \to \Lambda_c^{(*)+} X_c 2body$)
N($\Lambda_b^0 \to \Lambda_c^{(*)+} X_c mbody$)
N(combinatorial)
N(misid)

Varied in the fit
N($\Lambda_b^0 \to \Lambda_c^+ \mu^- \overline{\nu}_\mu$)
N($\Lambda_b^0 \to \Lambda_c^{*+}(2595, 2625, 2765, 2880)\mu^- \overline{\nu}_\mu$)
N($\Lambda b^0 \to \Lambda_c^{(*)+} X_c 2body$)
N($\Lambda b^0 \to \Lambda_c^{(*)+} X_c mbody$)
N(Combinatorial)
N(misid)
α_{linear}
$\alpha_{quadritic}$

TABLE 3.10: List of parameters used in the fit to data. α_{linear} and $\alpha_{quadritic}$ are defined in 3.7.2

3.7.1 Isolated region

The isolated region is the signal region, where we expect to have sensitivity to $R(\Lambda_c^+)$ and $R(\Lambda_c^+ \pi^+ \pi^-)$. The region is defined as the one which selects the data where no additional tracks pass the isolation criteria of having the isolation BDT value higher than 0.35. The dominant contributions here are the normalisation mode $\Lambda_b^0 \to \Lambda_c^+ \mu^- \overline{\nu}_\mu$, and the decay to the muonic excited states $\Lambda_b^0 \to \Lambda_c^{*+} \mu^- \overline{\nu}_\mu$. An example of a fit to isolated region is illustrated in Figure 3.34. No signal is plotted as the result is blind.

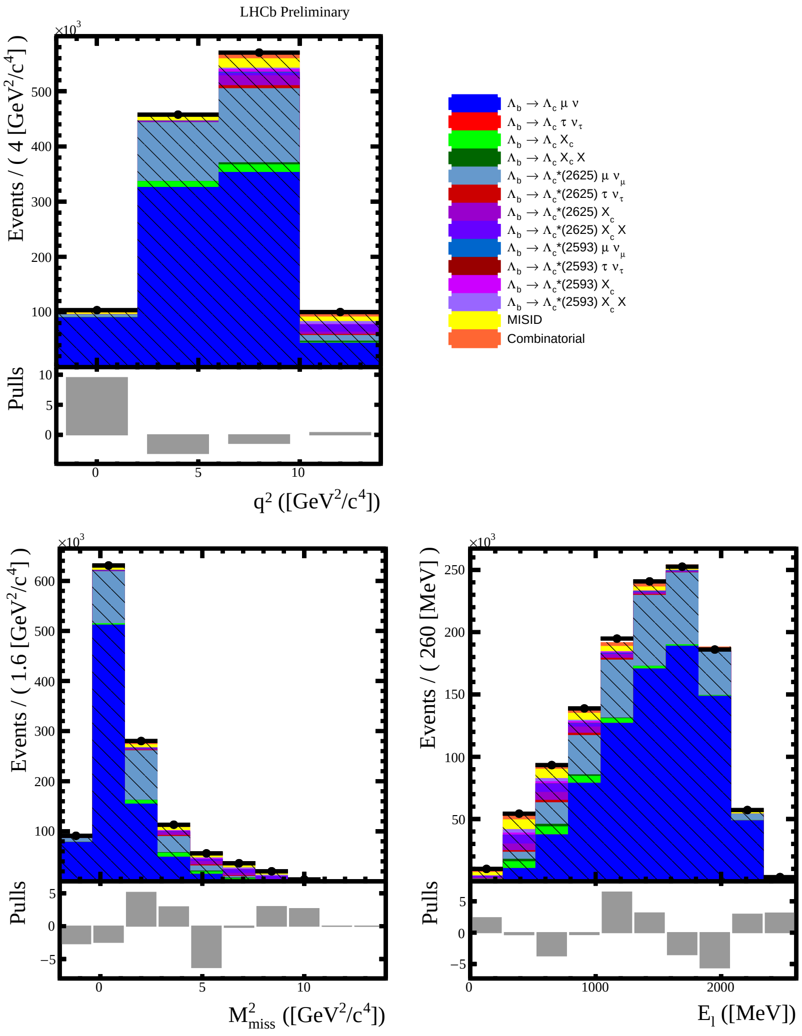

FIGURE 3.34: Multidimensional fit to isolated region.

3.7.2 Double-charm region

The double-charm region is the region where the dominant contribution is represented by misidentification and decays containing two charm hadrons ($\Lambda_b^0 \to \Lambda_c^+ X_c, X_c \to K\mu^-\overline{\nu}_\mu X$). We define this region by requiring two anti-isolated particles with the isolation BDT value less than 0.35, where at least one of them is identified as a kaon. An example of the fit to the double-charm region is shown in Figure 3.35.

Comparing the double-charm region in data and simulation reveals an obvious systematic mismodelling of the background from $\Lambda_b^0 \to \Lambda_c^+ X_c$ decays. To fix this we apply a multiplicative deformation following the $R(D^{*+})$ analysis method [76]. The deformation is implemented as $\pm 1\sigma$ variations to the double-charm template. The $\pm 1\sigma$ variations are constructed by reweighting $\Lambda_b^0 \to \Lambda_c^+ X_c$ events to correct the kinematics of the multi-body double-charm decays with two weight functions:

$$w(\alpha_{linear}) = 1 + 2\alpha_{linear}\left(\sqrt{\frac{m^2_{\Lambda_c^+ X_c} - (m_{\Lambda_c^+} + m_{X_c})^2}{(m_{\Lambda_b^0} - m_K)^2 - (m_{\Lambda_c} + m_{X_c})^2}} - \frac{1}{2}\right),$$

$$w(\alpha_{quadratic}) = (1 - \alpha_{quadratic}) + 8\alpha_{quadratic}\left(\sqrt{\frac{m^2_{\Lambda_c^+ X_c} - (m_{\Lambda_c^+} + m_{X_c})^2}{(m_{\Lambda_b^0} - m_K)^2 - (m_{\Lambda_c^+} + m_{X_c})^2}} - \frac{1}{2}\right)^2,$$

where $\alpha_i = \pm 1$.

3.7.3 The $\Lambda_c\pi\pi$ region

The $\Lambda_c^+\pi^+\pi^-$ region is the region where the dominant contribution is represented by decays to excited states Λ_c^{*+}. We define this region by requiring two anti-isolated particles that have opposite charges. In addition, the sum of their invariant mass in the combination with Λ_c^+ should not exceed 2700 MeV. An example of the fit to the $\Lambda_c^+\pi^+\pi^-$ region is shown in Figure 3.36. The fit shows a nice agreement, but some discrepancies are still observed. However, additional corrections are yet to be applied, such as the Λ_c^{*+} form-factors and MC corrections, which have a

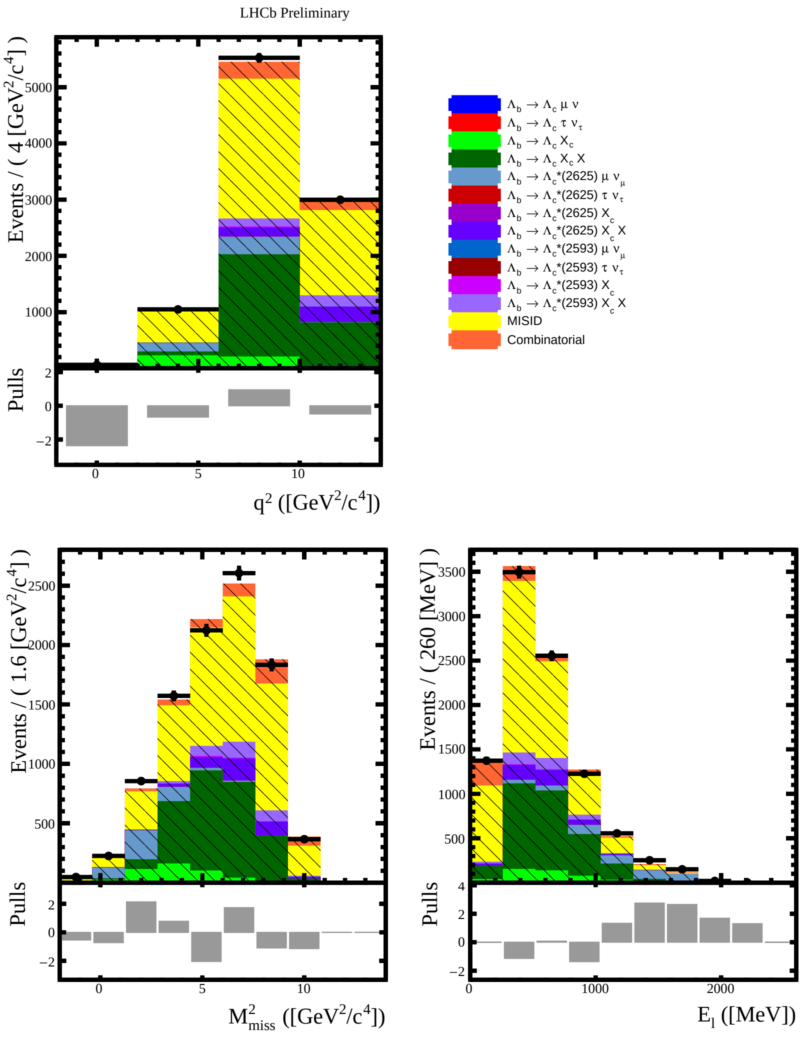

FIGURE 3.35: Multidimensional fit to the double-charm region.

potential to improve these discrepancies.

3.7.4 Fit validation

The fit validation was mentioned in subsection 3.4.1. In that case, the validation was performed in the isolated region only to estimate the statistical uncertainty on the fit. Below Figure 3.37 shows a simultaneous fit of the pseudodata to isolated and double-charm regions. Pseudodata corresponds to the mix of all templates with relative contribution taken from the fit to real data and varied according to the expected statistical uncertainties. The validation procedure was applied to the simultaneous

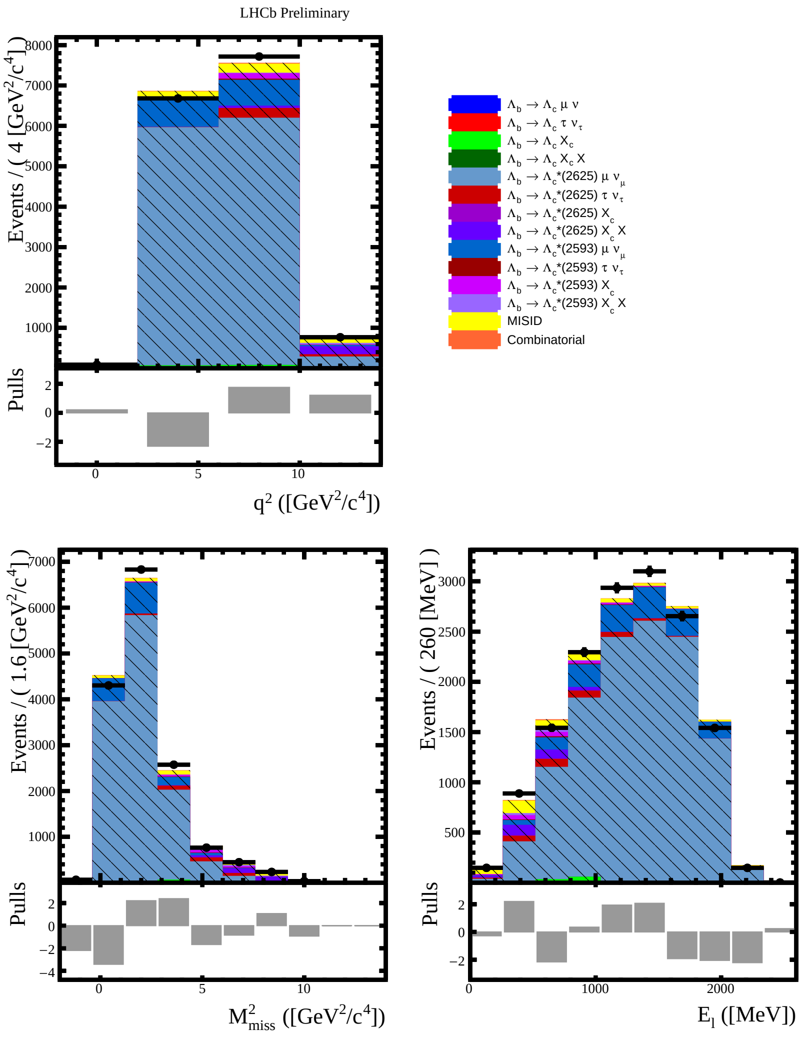

FIGURE 3.36: Multidimensional fit to the $\Lambda_c^+\pi^+\pi^-$ region.

fit, as well as to single fits separately. Good fit results are obtained which reinforce confidence in the fit.

3.8 Summary and outlook

This chapter has presented the semileptonic analysis of the lepton universality ratios $R(\Lambda_c^+) = \frac{\Lambda_b^0 \to \Lambda_c^+ \tau^- \overline{\nu}_\tau}{\Lambda_b^0 \to \Lambda_c^+ \mu^- \overline{\nu}_\mu}$ and $R(\Lambda_c^+\pi^+\pi^-) = \frac{\Lambda_b^0 \to \Lambda_c^{*+}(\to \Lambda_c^+\pi^+\pi^-)\tau^-\overline{\nu}_\tau}{\Lambda_b^0 \to \Lambda_c^{*+}(\to \Lambda_c^+\pi^+\pi^-)\mu^-\overline{\nu}_\mu}$, which will constitute the first measurement of the $\Lambda_b^0 \to \Lambda_c^+\tau^-\overline{\nu}_\tau$ and $\Lambda_b^0 \to \Lambda_c^+\pi^+\pi^-\tau^-\overline{\nu}_\tau$ decays, and also will help to shed light on the $R(D^{*+})$ anomaly. Unblinded results are not shown in this thesis because the analysis is still in progress

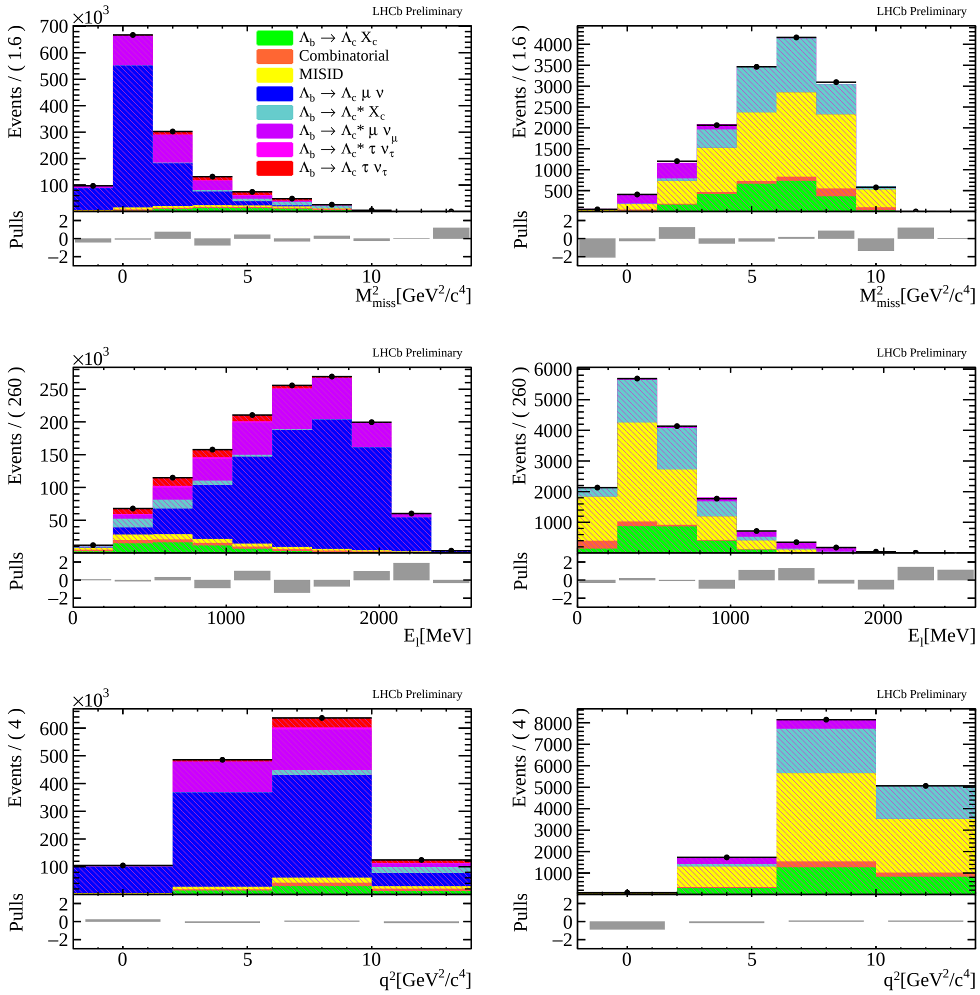

FIGURE 3.37: Simultaneous multidimensional fit of pseudodata to isolated (left) and double-charm (right) regions.

and results will remain blinded until the last moment. However, the analysis is well advanced and the only remaining task is to implement form-factor corrections for the $\Lambda_b^0 \to \Lambda_c^{*+} \tau^- \overline{\nu}_\tau$ decays, finalise data/MC corrections and expand the form factor correction to 2D, including the helicity angle ($\cos(\theta)$). In order to compute systematic uncertainties, the fit to the data must be finalised. The systematic uncertainties are likely to be dominated by the modelling of backgrounds. For this, many of the uncertainties will be taken into account with nuisance parameters, such as shape parameters for the double-charm background. For the data-simulation agreement and trigger emulation, the effects on $R(\Lambda_c^+)$

and $R(\Lambda_c^+\pi^+\pi^-)$ have to be studied using the final fit to the data. This will affect both, the efficiency ratios and signal yields. The analysis is expected to be finalised and published in the near future.

Chapter 4

Neutrino background studies and muon-shield optimisation for the SHiP experiment

4.1 Introduction

The discovery of the Higgs boson at the LHC confirmed that the SM is self-consistent and a valid effective field theory up to the Planck scale, which accounts for all elementary particles that have been found so far. However, there are several phenomena that indicate that the SM is not complete yet. Examples include the presence of non-zero neutrino mass, their flavour oscillations and the existence of dark matter. These observations suggest that there must be other particles in addition to those predicted by the SM. In recent years, many theories have been proposed that address these issues by the existence of new particles in a range of several orders of magnitude in mass. They are presented in Chapter 1. Therefore, while it is accepted that the SM is not complete we have no indication of the scale at which it resides.

The naturalness principle [97] predicted the existence of particles at the electroweak scale, in order to stabilize the Higgs mass. The non-observation of such particles in the first two runs of the LHC has led physicists to question naturalness as a guiding principle. In this situation, we can use three complementary strategies to search for new physics:

- The energy frontier:

  > The region of high energy may contain new, yet to be discovered particles with high masses. The reason we have not seen them is that we do not have an accelerator that can reach enough energy to produce these "heavy" particles.

- The precision frontier:

  > We will not directly observe any new particles at the high energy frontier, but a discrepancy appears between a measurement and SM predictions. This kind of search is called indirect and is performed in high-precision measurements at any energy scale. The $R(\Lambda_c^+)$ analysis presented in Chapter 3 belongs to this category of searches.

- The intensity frontier:

  > There is a region of higher intensities that holds new still undiscovered particles that interact extremely weakly with SM particles. The reason we have not seen them is that we cannot distinguish these rare events in the huge background of SM interactions.

Most experiments up to now have concentrated their searches on the energy (ATLAS, CMS) and precision (LHCb, BABAR, BELLE) frontiers.

However, recent searches for the weakly interacting particles are attracting more attention. This has led to several new proposals for experiments at the intensity frontier. The **S**earch for **Hi**dden **P**articles (SHiP) experiment belongs to this class of proposals and is described more in detail in this chapter. One of the peculiarities of the SHiP experiment is its unique ability to identify displaced vertices with the ability to measure the invariant mass and good particle identification (PID).

The concept of the experiment was first described in Ref. [98]. Subsequently, the SHiP Technical Proposal (TP) [99] and SHiP Physics Paper (PP) [29] were submitted to the CERN scientific communities. Since then it has received much interest within the high energy physics community. SHiP was also discussed in the context of the European Strategy for Particle Physics Update which took place in 2020 [100, 101].

4.2 Experimental overview

4.2.1 Overall concept

SHiP is a new general-purpose fixed target facility proposed at the CERN SPS accelerator to search for particles predicted by Hidden Portals. These particles are expected to be predominantly accessible through the decays of heavy flavour hadrons. The facility is therefore designed to maximise the production and detector acceptance for charm and beauty mesons, while providing the cleanest possible environment for the detection of hidden sector (HS) decays. The 400 GeV/c proton beam extracted from the SPS will be dumped on a high-density target to accumulate 2×10^{20} protons on target during five years of operation. The charm production at SHiP exceeds that of any existing or planned facility.

The basic concept of the experiment is shown in the Figure 4.1. The main idea is to dump a high-intensity beam into the heavy target, which allows to produce heavy flavour particles.

The layout of the experiment is optimised to have the best sensitivity to hidden sector particles, while minimising the flux of SM particles. The heavy target followed by an iron absorber is used to absorb rest light hadrons (π,K) that are produced in the primary interaction. Muons which cannot be efficiently stopped by the hadron absorber are deflected away from the detector area by a specially designed muon sweeper.

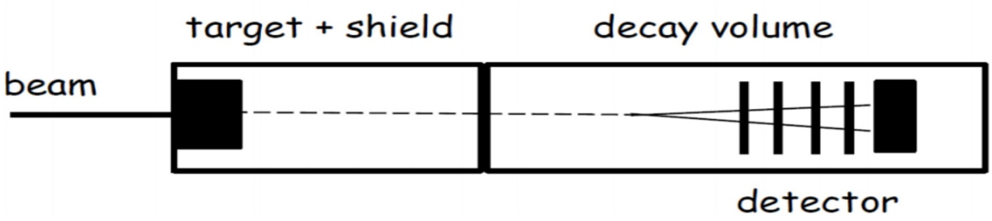

FIGURE 4.1: Conceptual scheme of the SHiP experiment.

A dedicated detector, based on a long vacuum tank, followed by a spectrometer and particle identification detectors, will allow to be sensitive to a variety of models with long-lived exotic particles with masses below $\mathcal{O}(10)$ GeV/c^2. Since hidden sector particles originating from charm and beauty hadrons are produced with a significant transverse momentum with respect to the beam axis, the detector should be placed as close as possible to the target.

A critical component of SHiP is the muon shield, which deflects the high flux of muons. These muons would represent a very serious background for new particle searches.

The detector is designed to fully reconstruct the exclusive decays of hidden particles and to reject the background down to below 0.1 events in the sample of 2×10^{20} protons on target. The detector consists of a large magnetic spectrometer located downstream of a 50 m-long and 5 × 10 m-wide decay volume. The decay volume is maintained under a vacuum to suppress the background from neutrinos interacting in the fiducial volume, as a neutrino interactions in the air could cause irreducible background for the experiment.

The spectrometer is designed to precisely reconstruct the decay vertex, mass and impact parameter of the decaying particle. A set of calorimeters followed by muon chambers provide identification of electrons, photons, muons and charged hadrons. A dedicated timing detector measures the coincidence of the decay products, which allows the rejection of combinatorial backgrounds. The decay volume is surrounded by background taggers to tag neutrino and muon inelastic scattering in the surrounding structures, which may produce long-lived SM "V^0 particles", such as K_L mesons, that have similar topologies to the expected signals.

The experimental facility is also ideally suited for studying interactions of tau neutrinos. It will, therefore, host an emulsion cloud chamber based on the OPERA concept [102], upstream of the hidden particle decay volume, followed by a muon spectrometer.

The experiment layout as modelled in simulation is depicted in Figure 4.2.

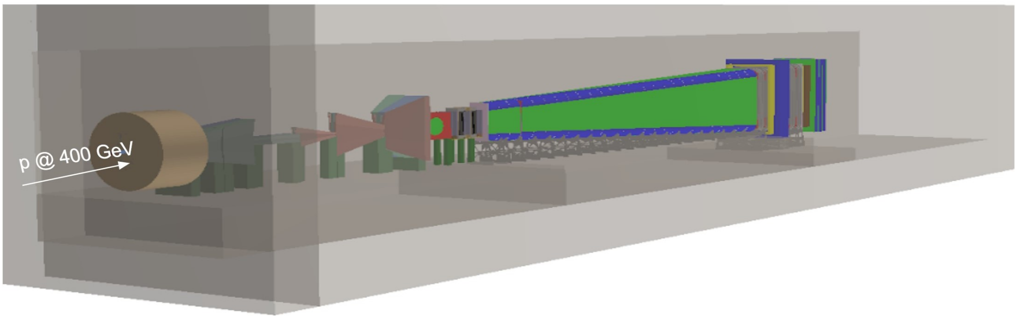

FIGURE 4.2: Depiction of the SHiP experiment taken from simulation.

In simulation, proton fixed-target collisions are generated by Pythia8 [103], inelastic neutrino interactions by GENIE [104] and inelastic muon interactions by Pythia6 [105]. The heavy flavour cascade production is also taken into account [106]. The SHiP detector response is simulated in the GEANT4 [107] framework. The simulation is done within the FairRoot package [108].

4.2.2 Beam-dump facility

A new dedicated beamline will service the SHiP experiment, branching off from the splitter section on the North Area of the Super Proton Synchrotron (SPS) [109].

The new beamline from the SPS will deliver the annual yield of $4 \cdot 10^{19}$ protons on target with a beam momentum of 400 GeV/c without compromising the beam requirements of the High Luminosity LHC or the operation of the existing SPS beam facilities. The length of one cycle is expected to be 7.2 s, while the duration of the actual spill (time length of bunch interaction) is 1.2 s. The combination of the intensity and the energy of the SPS proton beam allows the production of $\mathcal{O}(10^{18})$ charmed hadrons and more than 10^{21} photons above 100 MeV. At the same time, the feature of slow beam extraction grants a control on the combinatorial background, as it allows to use timing information to reject the random combination of tracks.

In addition, the Beam Dump Facility (BDF) will allow for the study of physics with tau neutrinos with unprecedented sensitivity. Five years of operation on the BDF target at 400 GeV/c would yield $\mathcal{O}(10^{16})$ tau and anti-tau neutrinos, so the first direct observation of the anti-tau neutrino and the measurement of tau neutrino and anti-tau neutrino cross-sections is one of the experiment's goals.

A new dedicated transfer line will deflect the beam from the SPS after the TT20 transfer line using a new splitter magnet system. Afterwards, the beam will be dumped on a high-power target that will be protected by a heavily shielded target complex. The new transfer line will keep the compatibility with the existing North Area operation, at the same time. The layout of the BDF is shown in Figure 4.3.

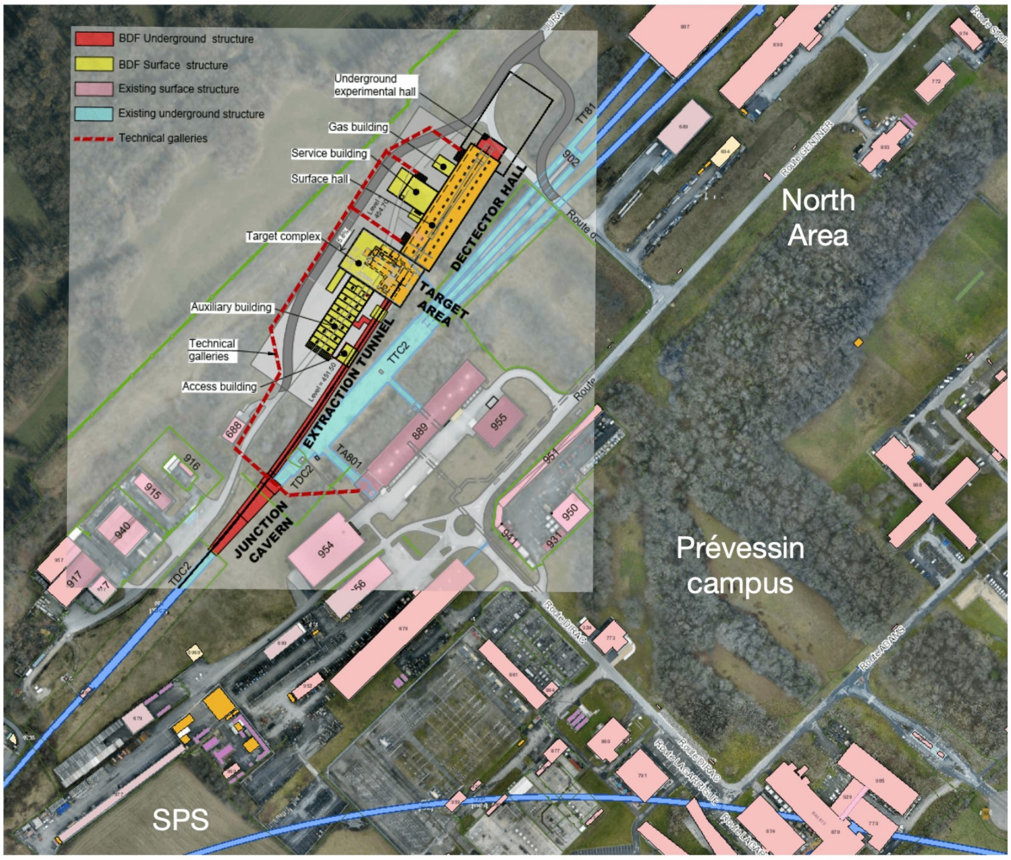

FIGURE 4.3: Proposed location of the BDF in the SPS North Area [99].

Studies of using the BDF for other flavour experiments are ongoing. For instance, it was proposed in Ref. [110] that the BDF could has an experimental searching for lepton flavour violation and rare decays.

4.2.3 The target bunker

The BDF will consist of the SHiP beamline and target complex. The target complex includes the target itself, part of the muon-shield and the target bunker. The purpose of the target bunker is to reduce the prompt dose rate during operation and the residual dose rate around the target during the shutdown, while the downstream proximity shielding also serves as a hadron absorber which incorporates part of the muon-shield. The purpose of the hadron absorber is to stop the secondary hadrons and the residual non-interacting protons, while protecting the downstream parts from the radiation. The layout of the target complex is shown in Figure 4.4.

The shielding will consist of 3700 t of water-cooled cast iron and steel shielding with outer dimensions of $6.8 \times 7.9 \times 11.2$ m^3 placed in a vessel filled with a gaseous helium to prevent the production of high mass isotopes generated by the interaction of secondary neutrons with air and to reduce the radiation-accelerated corrosion of the target and surrounding equipment.

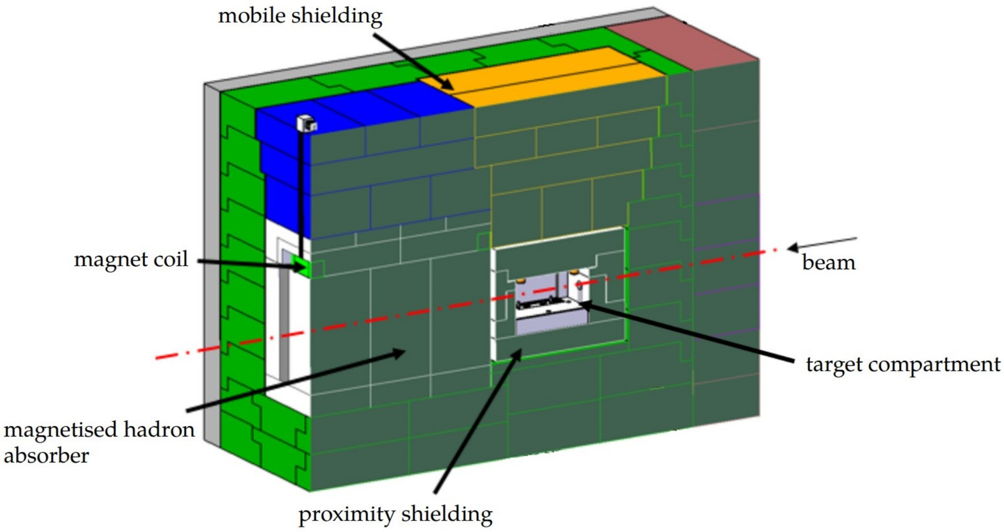

FIGURE 4.4: Layout of the SHiP target complex [111].

4.2.4 Target

The SHiP target aims to maximise both the production of charm and beauty hadrons and absorb pions and kaons produced in the target to reduce the background. This can be achieved using a high density material with a short nuclear interaction length. The challenge, in this case, is to deal with a high level of deposited power in the target, which amounts to 2.56 MW per spill. A possible way to handle it is to dilute the energy density in the target by spreading a beam spot and having a slow beam extraction. The chosen design for this purpose is a longitudinally segmented hybrid target consisting of blocks of four nuclear interaction lengths of a titanium-zirconium-doped molybdenum alloy followed by twelve nuclear interaction lengths of tungsten interleaved with 5 mm wide slots for water cooling. A schematic view of the SHiP target is shown in Figure 4.5

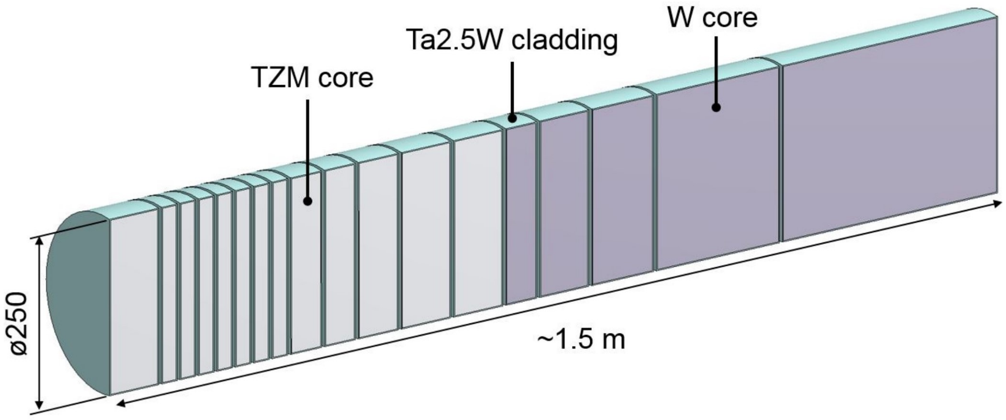

FIGURE 4.5: Layout of the SHiP target [112].

4.2.5 Muon-shield

While most of secondary SM particles will be absorbed inside the target and the hadron stopper following it, most muons will pass through. That is incompatible with the goals of the experiment, as it will create an undistinguishable background for hidden sector detector and damage the neutrino scattering detector.

The expected flux of muons emerging from the proton target amounts to $\mathcal{O}(10^{11})$ muons per spill of $4 \cdot 10^{13}$ protons. The background induced by muons can mimic new physics signals in the detectors through random combinations, as well as scatter inelastically in its material producing long-lived neutral particle vertices. The muon flux must be reduced by at least six orders of magnitude to keep both backgrounds under control. The design of the muon shield aims to allow the experiment to be as close as possible. This can be achieved by using a specially developed muon sweeping system based on magnets which will deflect muons from the vicinity of the detector acceptance. The first part of the muon-shield will start inside the target bunker, with a magnetic coil which magnetises the hadron stopper, made of US1010 steel, with a field of 1.7 T. The optimisation of the muon-shield was performed as part of this thesis and will be discussed in Section 4.5.

4.2.6 Scattering and Neutrino Detector

The design of the BDF also makes it the ideal place to investigate tau and anti-tau neutrinos. D_s mesons, which are produced in the target, are a great source of tau neutrinos through their fully leptonic decay. In addition, if dark matter is light enough it can be produced in the target and subsequently can be directly detected. For these reasons, a detector will be placed immediately after the muon-shield within the muon-free area. The main idea of the scattering and neutrino detector (SND) is based on the Emulsion Cloud Chamber (ECC) technique, which was previously successfully used in the OPERA experiment [102].

The first observation of tau neutrinos was reported by the DONUT experiment in 2008 with the detection of nine candidates [113]. Afterwards, the OPERA experiment [102] discovered tau neutrino appearance from muon neutrino oscillations, detecting ten tau neutrino candidates. Nevertheless, so far, there is no direct measurement of the tau anti-neutrino. The SHiP experiment will be the perfect ν_τ factory producing $6.6 \cdot 10^{15}$ tau neutrinos in the primary collision, that will be divided approximately equally between neutrinos and anti-neutrinos. This will lead to 10^4 interactions of tau neutrinos and anti-neutrinos within the SND target.

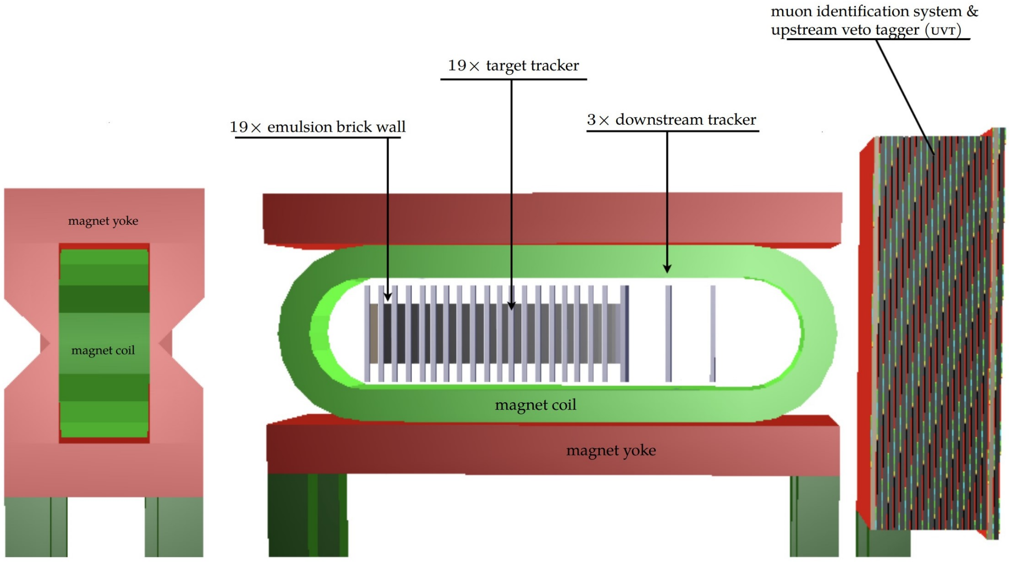

FIGURE 4.6: Scattering and Neutrino Detector in front (left) and side (right) views [112].

The SND detector consists of a magnetised region which is made up of the neutrino target and a particle spectrometer, followed by a muon identification system. A view of the detector is illustrated in Figure 4.6. The distinctive shape seen in the front view is explained by the spatial distribution of muons coming out the muon-shield (see Figure 4.7).

The spectrometer will be made of a sequence of low-density material and emulsion films to measure the charge and the momentum of hadrons in

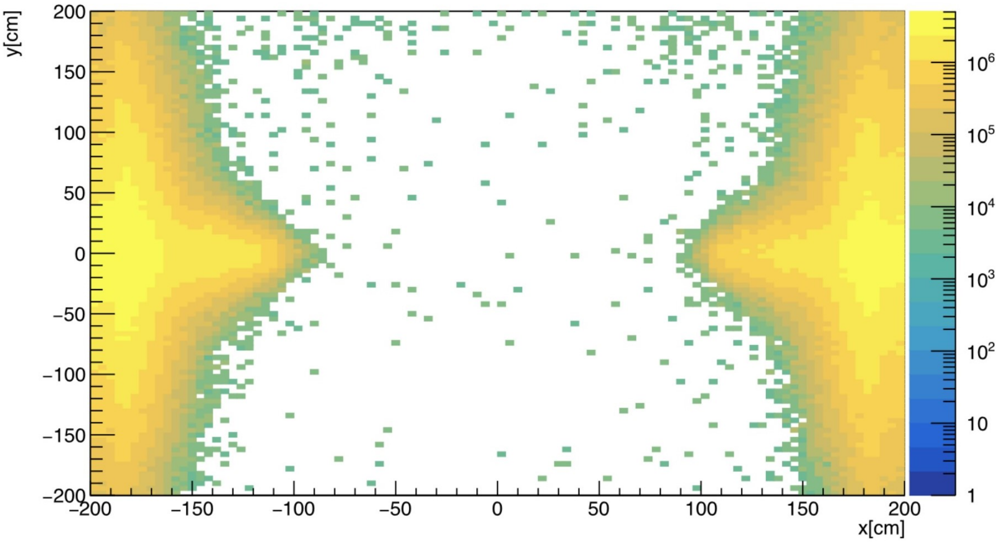

FIGURE 4.7: Muon flux distribution in the transverse plane immediately downstream of the last sweeper magnet [111].

the magnetic field. This emulsion target is followed by high resolution tracking stations to provide the time measurement of the event, measure the charge and momentum for particles with momenta above 10 GeV/c and to connect tracks from the emulsion target to the muon system. The detector will finish with a muon system consisting of iron slabs, alternated with RPCs to provide the tracking within slabs. The muon system will also be used as an upstream veto tagger for the background to the Hidden Sector Detector [114].

4.2.7 Vacuum vessel

The Hidden Sector detector follows the SND detector. It consists of two crucial parts: a decay volume and a spectrometer. The new physics signature of hidden sector particles consists of a displaced vertex in the fiducial volume. Since we expect NP particles to be long-lived, we need a long decay volume. The signal acceptance depends linearly on the length of the decay volume.

The discovery potential of the SHiP experiment depends drastically on how well we can suppress SM particles. Since we stop all hadrons before the decay volume thanks to a heavy target and hadron absorber, and we reduce the muon flux substantially with a muon-shield, the remaining background is induced by neutrinos.

Deep-inelastic neutrino-nucleon scattering in the detector volume can produce long-lived neutral particles, which are backgrounds. These particles may decay inside the decay volume and mimic the topology of the hidden sector particle decays. We expect to have a flux of $4.5 \cdot 10^{18}$ neutrinos and $3 \cdot 10^{18}$ anti-neutrinos in the acceptance in five nominal years running.

The vacuum vessel needs to be kept at a pressure of 1 mbar to suppress neutrino-induced backgrounds inside the fiducial decay volume. My studies have shown that with this requirement, all neutrino interactions will mainly happen in the decay volume walls and can be rejected using basic selection criteria based on directional requirement. Residual neutrino interactions, as well as muon deep-inelastic interactions with the vessel material, will be vetoed by the Surrounding Background Tagger (SBT) system, which covers the entire decay volume.

The decay volume will have a length of 50 m with a pyramidal frustum shape and will be located directly downstream of the SND. The shape and length of the detector has been optimised taking into account two main factors: maximising the acceptance to the different HS decay channels given the transverse aperture of the spectrometer, while staying within the region cleared from the muon flux. The decay volume is shown in the Figure 4.8.

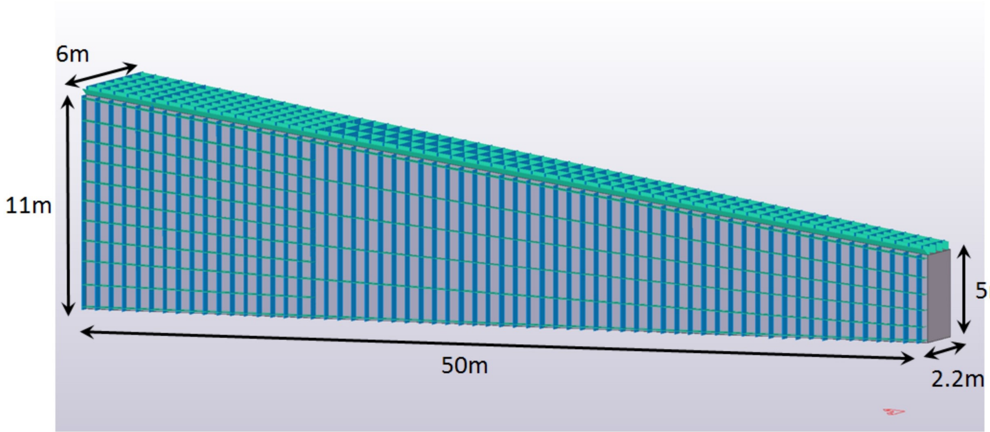

FIGURE 4.8: Illustration of the decay volume structure [111].

4.2.8 Tracking stations

The spectrometer will be located inside the decay volume and will also be kept under vacuum. It will consist of four tracking stations which will run through the spectrometer magnet, with two stations upstream and two stations downstream of the magnet.

The purpose of the spectrometer is to reconstruct the tracks of charged particles coming from the new physics (NP) particles decay with high efficiency and distinguish these from the background events. At the same time, the spectrometer must take care of the reconstruction of the flight direction within the fiducial volume and perform an accurate determination of the track momentum. Tracks reconstructed in the spectrometer must also be well-matched with a segment of the timing detector. We rely on these systems to reconstruct the invariant mass, the vertex, the timing and impact parameter to the target, which are crucial qualities for the rejection of the background originating from neutral meson decays or combinatorial combinations.

The layout of the spectrometer system is depicted in Figure 4.9. All four tracking sections have the same spatial parameters, which is dictated by the dipole magnet size and decay volume aperture. The nominal acceptance of the tracking stations is 5 m in the X-axis and 10 m in the Y-axis. Each station contains four views, in a Y-U-V-Y arrangement, where U and V are stereoviews with straws rotated by a small angle $\pm\theta_{STEREO}$ around the Z-axis.

The design of the spectrometer stations will be based on an ultra-thin straw-tube technology, oriented horizontally with a straw diameter of 20 mm [115].

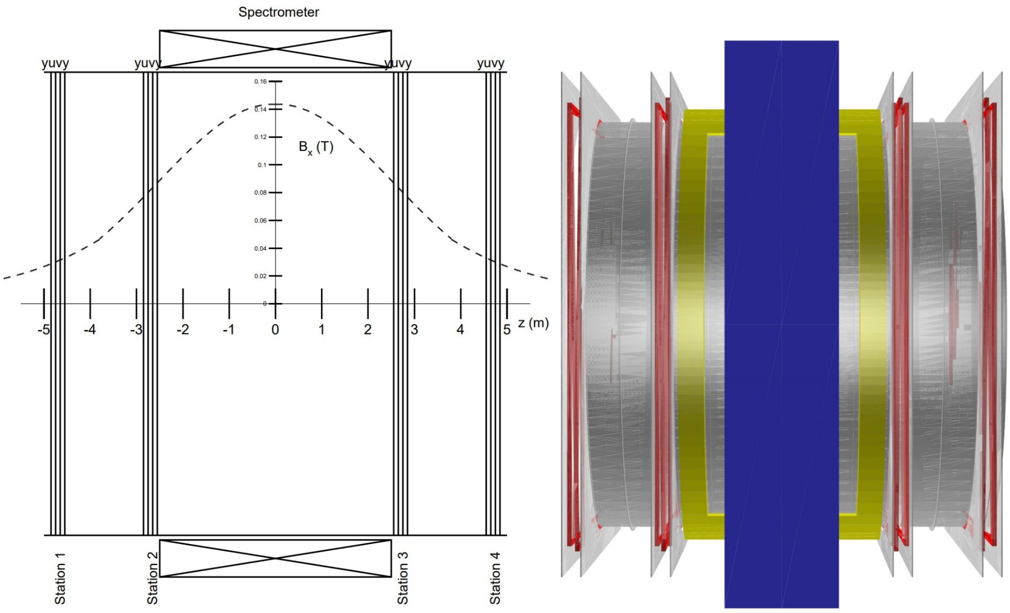

FIGURE 4.9: Illustration of the spectrometer system [116].

4.2.9 Spectrometer magnet

The spectrometer magnet is located in the middle of the tracking system and enables the determination of particle charge and momentum. It is a dipole with an aperture of 5.1×10.35 m^2 with a horizontal field providing a vertical bending plane for the horizontally oriented straw tracker. The magnet consists of two coils surrounded by a window-frame yoke structure to provide a uniform magnetic field inside the magnet aperture and to minimise power consumption. The magnet has been designed for a maximum field induction of 1.75 T at a nominal bending strength of 0.65 Tm. A schematic view of the spectrometer magnet, together with its field map, is shown in Figure 4.10.

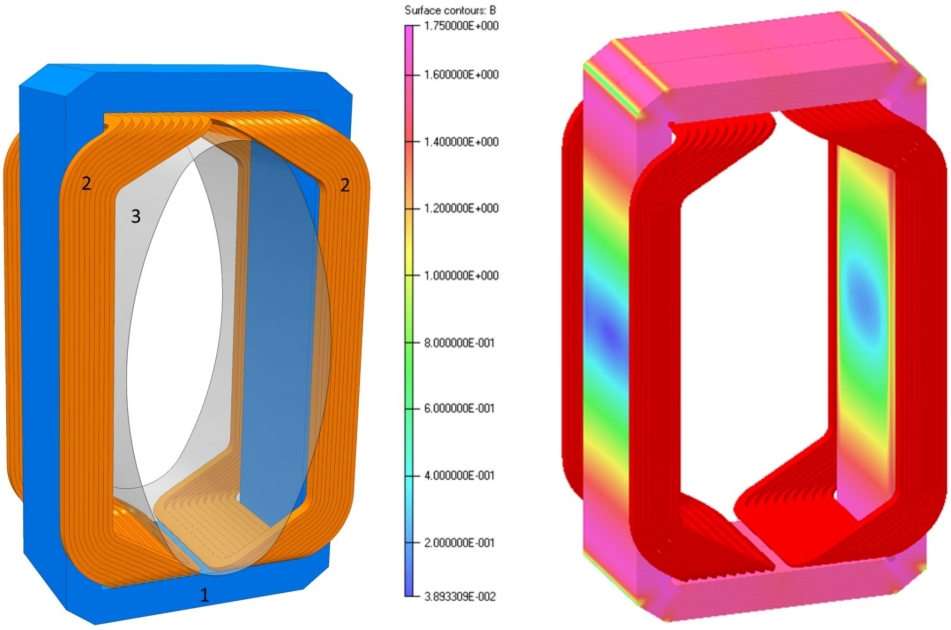

FIGURE 4.10: Illustration of the spectrometer magnet and its field amplitude map inside the iron yoke [116].

4.2.10 Timing detector

The experiment requires a timing detector to combat combinatorial background. To suppress this type of background, we need a detector with a timing resolution of 100 ps or less. The main option consists of a plastic scintillator-based technology consisting of three columns of bars instrumented by arrays of large-area SiPMs. The bars will be arranged in three columns and 182 rows with a 0.5 cm overlap between bars for a total area of 5 m × 10 m. Each bar will be read out on both sides by an array of eight 6 mm × 6 mm SiPMs. The signals from the eight SiPMs are summed by an ASIC based on the MUSIC chip [117] to form a single channel (see Figure 4.11).

An alternative technology of the multi gap resistive plate chambers (MRPC) for the timing detector is under investigation [118].

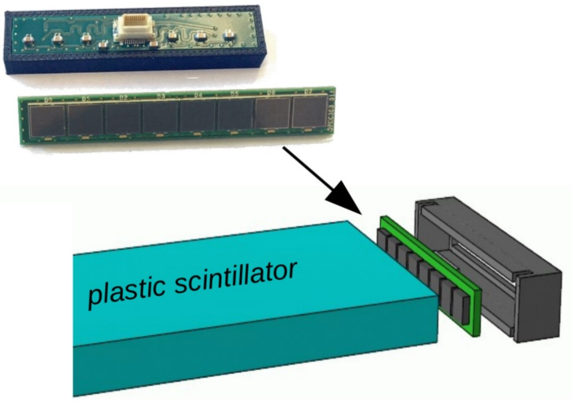

FIGURE 4.11: Array of eight SiPMs integrated into a PCB with a parallel connection and applied directly to the bar surface [111].

4.2.11 Calorimeter

In the SHiP experiment, particle identification is needed to discriminate between different HS models. This goal can be achieved by having a segmented calorimeter called the SplitCal. The SHiP calorimeter is also able to reconstruct Axion-Like-Particles (ALP) decaying to two-photon final states. For these purposes, we will use a longitudinally segmented lead sampling calorimeter consisting of two parts. Each part will be equipped with high spatial resolution layers in order to provide pointing with a resolution of 5 mrad for photons originating from ALP decays.

4.2.12 Muon detector

The muon system identifies the muons from the signal channels and separates them from those produced in neutrino and muon-induced backgrounds. The muon detector will be located downstream of the electromagnetic calorimeter. It will consist of four stations of active layers interleaved by three muon filters. The active layers will consist of scintillating tiles with direct SiPM readout technology.

4.3 Physics sensitivity

4.3.1 Signal strategy

The remarkable feature of SHiP is that it can not only validate (or disprove) the wide range of different theoretical models for the new feebly-interacting particles, but also distinguish different new physics channels and measure their properties. The detectors are designed to be sensitive to as many decay modes as possible to ensure a model-independent search for hidden particles [119]. A set of models have been implemented in the SHiP software framework, the sensitivities to which will be discussed later.

The typical signature for all benchmark hidden sector models, described in Chapter 1, is an isolated vertex in the decay volume. Therefore, signal candidates are required to form an isolated vertex in the fiducial volume. Decay modes can also be split into two categories: fully reconstructed, meaning that all daughters coming from the decay are reconstructible in the spectrometer (for instance, $HNL \to \mu\pi$); and partially reconstructed, meaning that one or more daughters coming from the decay cannot be reconstructed in the spectrometer (for instance, $HNL \to \mu\mu\nu_\mu$).

The single most discriminating requirement for signal selection is the pointing back to the target; *i.e.* requiring that it’s impact parameter must be less than 10 cm. Unfortunately, while this selection is very efficient for fully reconstructed events, partially reconstructed final states are more challenging to select. Since we are missing some signal state particles, the reconstructed event will loosely point to the target. Therefore, for these searches the signal candidates are required to have an impact parameter less than 250 cm. To isolate them better, we also require to have no activity in the detectors surrounding the decay volume. Selections on the track and vertex quality, as well as on the distance from any material are also applied. The basic signal selection based on the topology of events is summarised in Table 4.1, where the variables defined as follows:

- $N_{candidates}$ is a number of reconstructed candidates per event.
- $N_{d.o.f}$ is the number of degrees of freedom for a track.
- $DOCA$ is the distance of closest approach between two charged tracks forming the vertex.
- $\chi^2/N_{d.o.f}$ is the χ^2 per a number of degrees of freedom of the track fit.
- P_{track} is the track momentum of the candidate's daughters.
- IP is the impact parameter of the reconstructed candidate to the target.

	Fully reconstructed	Partially reconstructed
$N_{candidates}$	1	1
Vertex is inside the fiducial volume	✓	✓
Tracks traverse all tracking stations	✓	✓
$N_{d.o.f}$	>25	>25
$DOCA$	< 1 cm	< 1 cm
$\chi^2/N_{d.o.f}$	<5	<5
P_{track}	> 1.5 GeV/c	> 1.5 GeV/c
IP	< 10 cm	< 2.5 m

TABLE 4.1: Basic signal selection for the fully ($HNL \rightarrow \mu\pi$) and partially ($HNL \rightarrow \mu\mu\nu_\mu$) reconstructed events.

4.3.2 Signals

A benchmark channel for the SHiP experiment is the decay of a Heavy Neutral Lepton (HNL) predicted by several models, including the neutrino minimal Standard Model. The dominant production channel for HNL in the SHiP experiment is through weak decays of flavoured mesons. In the case of HNLs with masses $M \leq 500\ \mathrm{MeV}/c^2$, kaon decays are the dominant production channel. However, the limits on HNL production from kaon decays are already set by the $NA62$ experiment [120]. For these reason, in SHiP most of kaons will be stopped in the target or hadron absorber before decaying for background suppression purposes. Therefore, only HNL originated from charm and beauty mesons decays are considered in the sensitivity estimations. The production rates are shown in Figure 4.12.

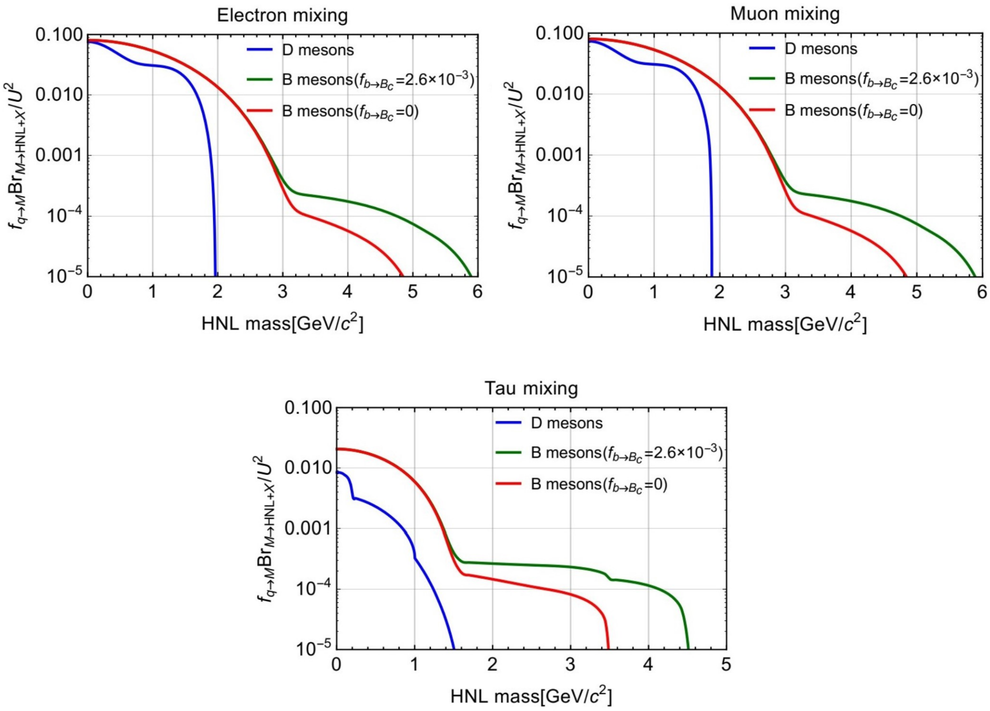

FIGURE 4.12: Meson fragmentation fraction times branching fraction of meson decays to HNL as a function of the HNL mass [111].

The study of the HNL sensitivities were done for different ratios between the three mixing angles (Chapter 1) and different decay channels. It is described in detail in [98, 111]. As an example, the sensitivity curve for HNLs with three couplings $U_e^2 : U_\mu^2 : U_\tau^2 = 0 : 1 : 0$ is shown in Figure 4.13. The signal yield depends on the fourth power of the HNL-neutrino mixing, U^4, as the same mixing gives rise to the decay of the HNL to SM, as to HNL production.

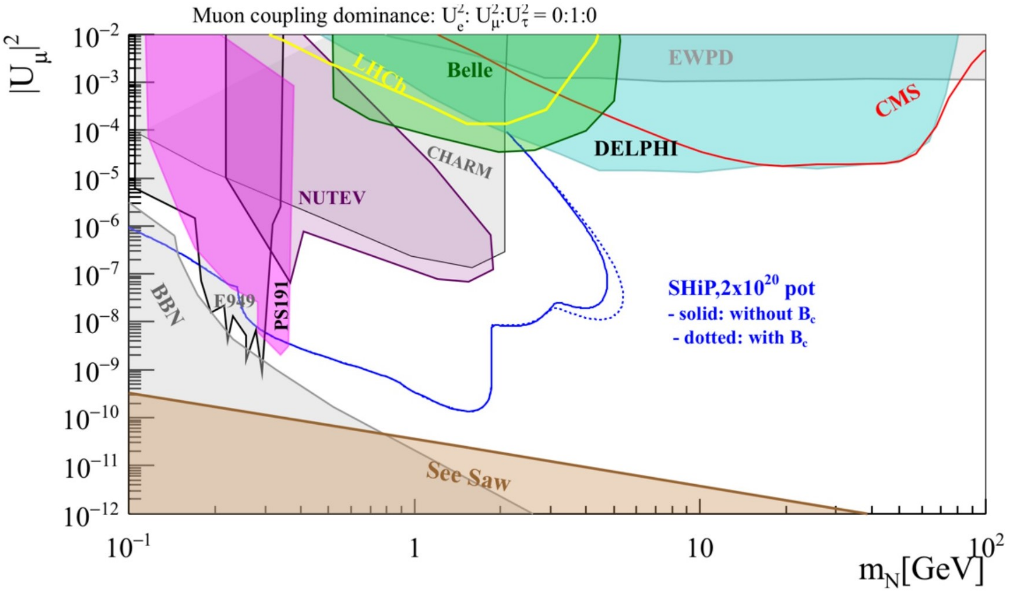

FIGURE 4.13: Sensitivity curve for HNLs with the benchmark assumption [111].

Dark photons are predicted by a range of models [33, 121]. There are different production mechanisms at a fixed-target experiment. Dark photons with masses below 0.9 GeV/c^2 can mix with photons from neutral meson decays that are produced in non-diffractive interactions. The proton-proton interaction can also produce the radiation of a dark photon via a bremsstrahlung process, which is dominant for dark photon masses in the range $0.4 - 1.3$ GeV/c^2. For masses higher than 1.3 GeV/c^2 the dominant production mechanism is through quark-quark annihilation into the dark photon, analogous to Drell-Yan process.

The combined sensitivities of SHiP to dark photons is shown in Figure 4.14.

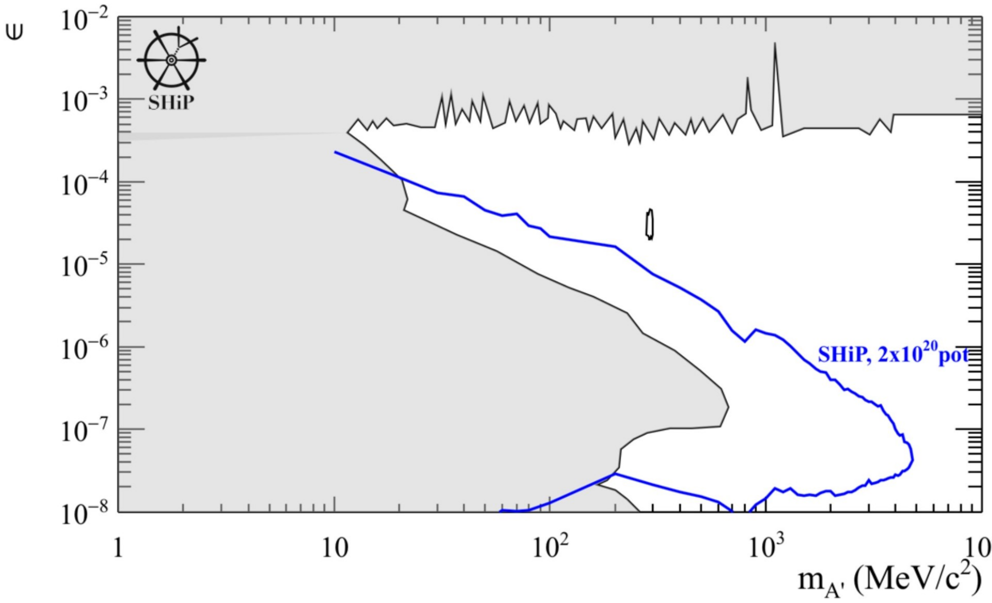

FIGURE 4.14: Sensitivity curve for the dark photon as function of its mass and of the kinetic mixing parameter for the three production modes [111].

The SHiP experiment is also very well suited for searches of axion-like particles (ALPs). Two cases are considered in the sensitivity estimations: the coupling of ALP with photons and with fermions. A model with an exclusive coupling to two photons was used as a benchmark model. The SplitCal will be used to reconstruct these decays, providing a unique sensitivity in the mass range 200 MeV/c^2 – 1 GeV/c^2. The comparison of the sensitivity for ALP decaying to two photons for different experiments is shown in Figure 4.15.

SHiP is also sensitive as well to dark scalars which can be produced through meson decays. The CKM contribution to the amplitude depending on the meson:

$$\Gamma(K \to \pi S) \propto m_t^4 \lambda^5,$$

$$\Gamma(D \to \pi S) \propto m_b^4 \lambda^5,$$

$$\Gamma(B \to KS) \propto m_b^4 \lambda^2,$$

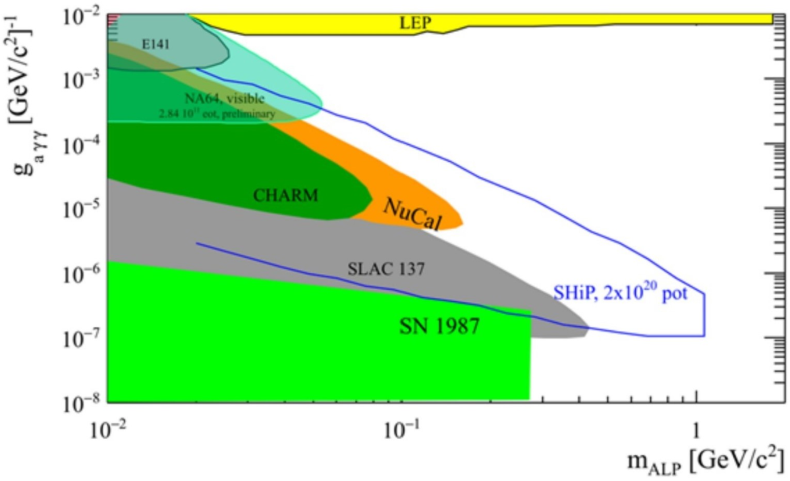

FIGURE 4.15: Sensitivity curve for ALP decaying to two photons [110].

where $\lambda \approx 0.225$ is a parameter of CKM matrix in Wolfenstein form [122]. Therefore, the production of dark scalar through D meson decays is highly suppressed in comparison to B and K mesons. SHiP is only sensitive to B mesons decay mode, as most of the kaons will be absorbed. The sensitivity to Dark Scalars is shown in Figure 4.16 [39].

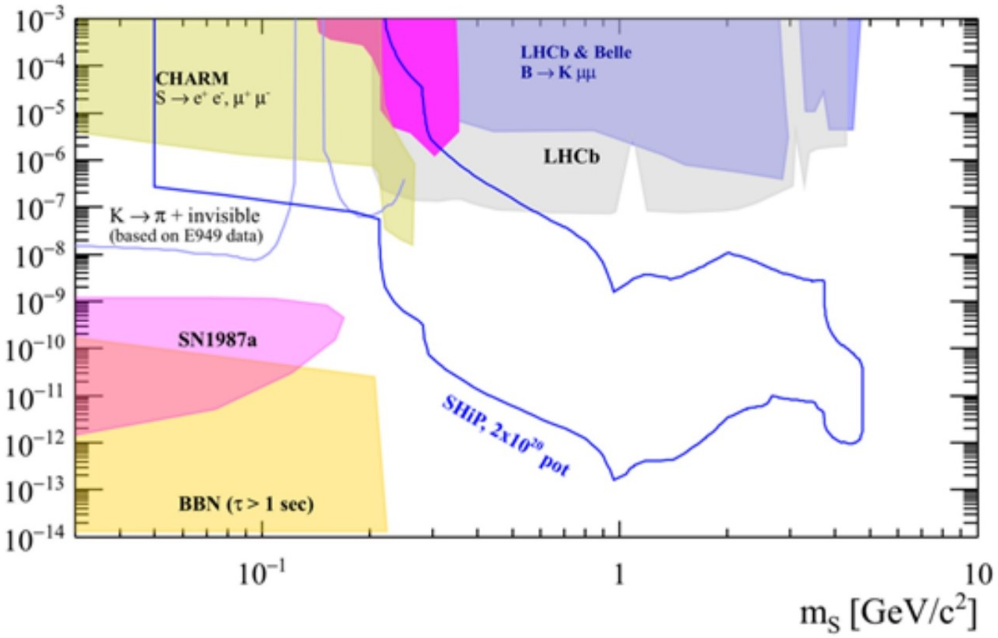

FIGURE 4.16: Sensitivity curve for dark scalar [110].

4.4 Backgrounds

All sensitivities so far discussed require redundant background suppression. The aim of the SHiP experiment is to achieve less than 0.1 background events in five years of running. There are three primary sources of background which can mimic the HS particle signal: neutrino-induced backgrounds from inelastic interactions in the detector material and the cavern walls, muon-induced backgrounds from inelastic interactions and combinatorial background produced by a random combination of residual muons. Background from cosmic muons can be neglected [99].

4.4.1 Muon combinatorial

There are two types of muons which can reach the detector spectrometer: the ones which penetrate the muon-shield and those which backscatter from the surrounding cavern walls. Any such muons can create a charged-particle track in the tracking stations, and therefore a random combination of them can mimic the signal. To estimate this background, a sample of simulated muons which survive the muon-shield was analysed and unique pairs of tracks were formed from these events. The basic selection is based on the pointing and track and vertex qualities, which were before discussed already, allowing the combinatorial background to be reduced by six orders of magnitude.

To further reduce the combinatorial background we use timing. We expect to have 8.5×10^{15} pairs of tracks in five years of running. The suppression factor of timing detector is 10^{-11}, even with the assumption of 340 ps resolution that is three times worse than expected. The factor was estimated considering the probability to find two muons in a time interval $\delta T = 340$ ps as a Poisson distribution with mean p_μ, where

$p_\mu = F \cdot \delta T$ is the probability to find a muon in δT having a flux of $F = 10^5$ Hz muons [116].

Together with basic selection cuts, it will reduce the background to the level of 10^{-2} events over the lifetime of the experiment. Further rejection not included in this estimation can be reached by using the information from the surrounding taggers and upstream muon system of the SND. This will provide an additional suppression up to 10^{-4}.

4.4.2 Muon deep-inelastic scattering

Muons can also interact inelastically in the cavern walls, floor, SND detector or material upstream the decay vessel. We expect to have 2.1×10^8 muon deep-inelastic interactions in the decay volume in five nominal years of running. The particular feature of these events is that they are mostly located in the entrance of the decay volume (see Figure 4.17) and have high multiplicity. Therefore, the combination of basic selection cuts (see Table 4.1) together with activity information from the SBT or veto taggers brings down this background to the 10^{-4} level over the lifetime of the experiment.

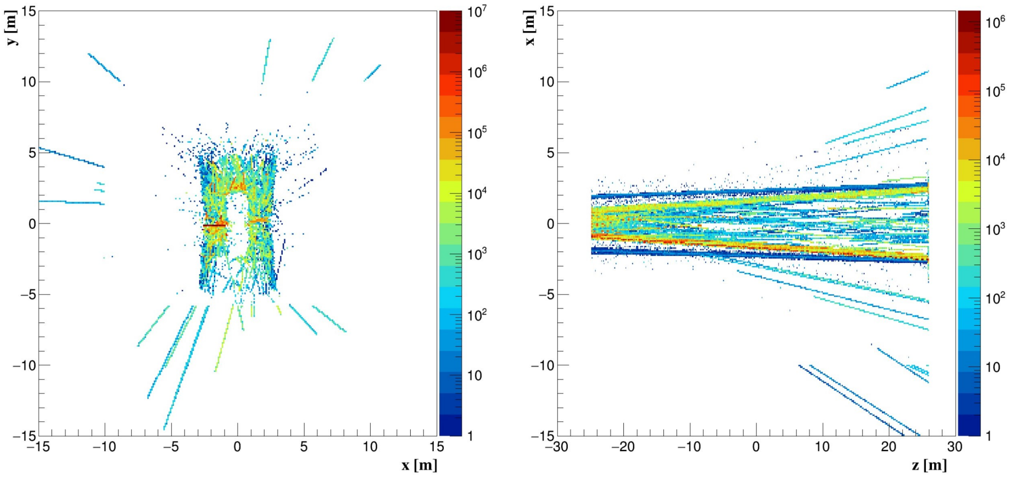

FIGURE 4.17: Interaction points of generated muon deep-inelastic scattering events before the selection [112].

4.4.3 Neutrino induced

The main background for the SHiP experiment consists of neutrino induced background. First of all, the yield of neutrino interaction is comparable to that of muons, since neutrinos cannot be deflected. Secondly, neutrino are much more difficult to veto. Particularly dangerous are neutrino interactions producing long-lived SM particles such, as K_L, which can closely mimic the signal. The estimation of neutrino background was carried out in the context of this thesis and is discussed in Chapter 4.6.

4.5 Muon-shield optimisation

The concept of the muon-shield was introduced before and presented in its final design. The optimisation procedure of this muon-shield was part of this thesis work and described below. This work was carried out for the technical proposal. At that time, the decay volume was a cylinder of dimensions $(x, y) = (5, 10)$ m. Later on , SHIP evolved to a pyramidal frustum, which relaxes the requirement of the shield, having to clear only 5×10 m^2 at the position of the last tracking station.

While muons of a given energy can easily be deflected out of the acceptance of the spectrometer by a magnetic field, the problem is the large spread in the phase space of muons, as shown in Figure 4.18, with the consequence that the return field of the magnets tend to bend muons back towards the spectrometer. The DONUT [113] experiment employed a combination of active and passive shielding to clear muons from their emulsion target, which was located 36 m downstream of the target.

SHiP will accumulate three orders of magnitude more protons on target, and hence requires a much larger reduction in muon flux for both the emulsion and the hidden sector particles search.

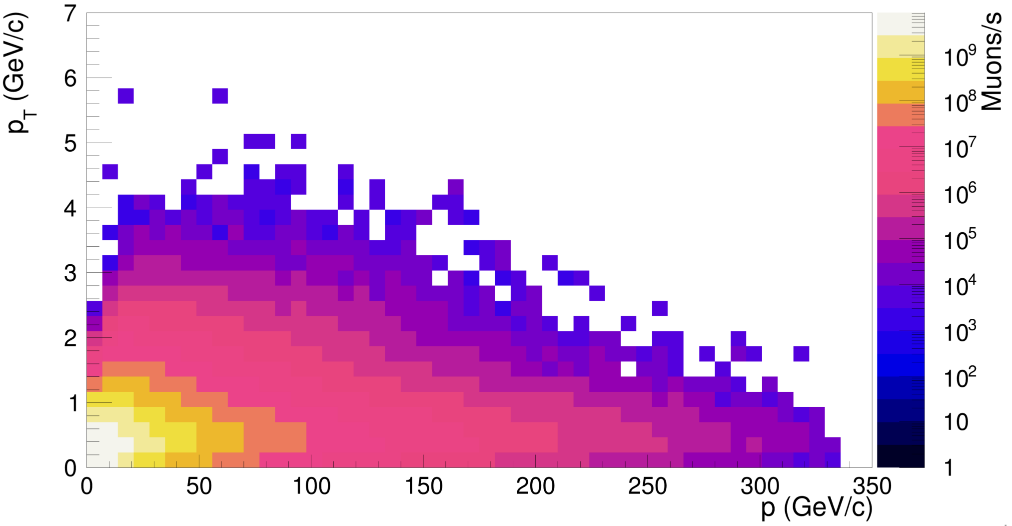

FIGURE 4.18: Transverse momentum versus momentum distribution of muons, as generated by Pythia8.

4.5.1 The basic principle of magnet based muon-shielding

The principle of the magnet based shielding is shown in 2D in Figure 4.19. The first part of the shield should be long enough, *i.e.* provide sufficient $\int B\partial l$, to separate both muon polarities to either side of the z-axis. For a 350 GeV/c muon, taking into account the P_T distribution at its production point, this requires a $\sim$ 18 m long magnet with a field[1] in the iron of 1.8 T.

Lower momentum muons, which traverse the return field of this magnet, will be bent back in the direction of the spectrometer as is shown in Figure 4.19 for a 50 GeV/c muon. To shield the spectrometer from these muons, an additional magnet is added with opposite polarity field close to the z-axis, and hence the lower momentum muons will be swept out again. At the start of this second magnet, the two field polarities should be as close in x as possible . A magnet design study [123] shows that an air gap as small as 2 cm between the two field polarities can be used

---

[1] When using a high permeability material such as grain-oriented steel a 1.8 T flux density could be obtained while the coils would dissipate low-enough power so that they could still be cooled with air [123].

without distorting the 1.8 T field in the iron.

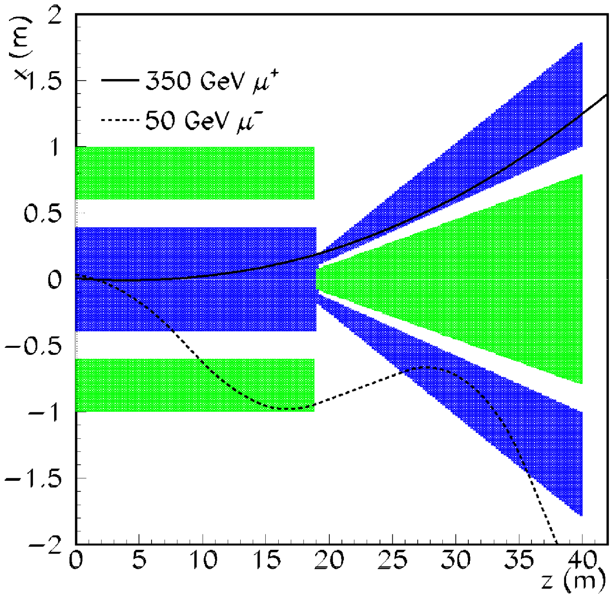

FIGURE 4.19: Cross section at y=0 shows the principle of magnetic shielding. The magnetic field is along the y-axis, and its polarity is indicated by the blue/green color of the iron poles of the magnets. The trajectories of a 350 GeV/c muon and 50 GeV/c muon are shown with a full and dashed line, respectively.

4.5.2 Simulations and optimization

To test the basic principle of the muon-shielding concept described in Section 4.5.1 and optimize its layout, a fast simulation was written which traces the muons through the magnets. Each magnet is described by the following seven parameters: length and, at either end, width, height, and air-gap width between field and return field. Muons are traced through a setup with a step size of 5 cm, and only the following physics processes are taken into account: bending in a 1.8 T magnetic field, specific energy loss ($\partial E/\partial x$) and Gaussian smeared multiple Coulomb scattering.

The aim is to design the shortest possible shield which allows no muons to reach the spectrometer, while at the same time containing costs and hence using as little iron as possible. These requirements are combined into a single penalty function which is then minimized. The penalty function is given by

$$\frac{W \times (1 + \Sigma\chi_{\mu})}{A} \tag{4.1}$$

where:

- All muons are given the same charge. The transverse (x,y) position of muons is obtained at the last tracking station, which has a sensitive area of 5×10 m^2, by tracing their trajectory 64 m downstream of the shield. For muons with $|y| < 5$ m, their x-position is converted into $\chi_{\mu} = \sqrt{(5.6 - (x + 3.))/5.6}$ for $-3 < x < 2.6$ m, else $\chi_{\mu} = 0$. In this way we are independent from a muon polarity in the penalty function by positioning all of them in the positive region (3 m shift) and looking then on the center of the plane, where the acceptance for muons is 5.6 m. The χ_{μ} is higher as closer we are to the center;
- $A = 1. - L/100$: Approximately the relative acceptance of a new long lived particle in a benchmark scenario, where L is the length of the shield in m;
- W: Weight of the shield in tonnes of iron;
- The sum is taken over all muons.

The optimization uses Minuit [124] to minimize the penalty function (3.1) by varying the size of the magnets. Only muons with $P > 1$ GeV$/c$ at the last tracking station are considered as background muons, since only high momentum tracks will be used in searches. Magnet transverse sizes are only allowed to vary in steps of 1 cm. Magnet length sizes are only allowed to vary in steps of 10 cm. The tracing of each muon is always started with the same random number, seeded by its momentum, to minimize statistical uncertainties of multiple scattering contributions between different geometry configurations. For simplicity, the optimization is made with seven magnets. The first two magnets after the beam dump are also required for radiation protection and their lengths are fixed to 1.4 and 3.4 m respectively, their gaps are fixed to 2 cm and they have the same height at either end of each magnet.

The muons were generated with Pythia [103, 105], corresponding to $\sim 10^{10}$ protons on target (POT), and the Minuit SIMPLEX algorithm varies 41 parameters to minimize the penalty function. After convergence, none of the muons traverse the last tracking station for a total shield length of 34 m. Its layout and performance is presented in the next section.

4.5.3 Active muon-shield performance

The SHiP experiment simulations are performed in the software package FairShip [99]. FairShip is a collection of libraries and scripts based on the FairRoot framework [125], which is fully based on the ROOT software framework [126]. In this framework, users can construct their detectors, and perform simulation and analysis without any code dependence on a specific Monte Carlo simulation software. FairRoot uses the ROOT geometry package TGeo to build, browse, track and visualize the detector geometry.

The muon-shield can be made of two different magnet types, which are depicted in Figure 4.20. When there is enough air-gap between the iron yokes with the opposite field direction to place a coil a magnet of type a) in Figure 4.20 is used. If the optimization requires an air-gap which is too small to accommodate a coil, a magnet of type b) in Figure 4.20, which has place for coils at the top and bottom, is used.

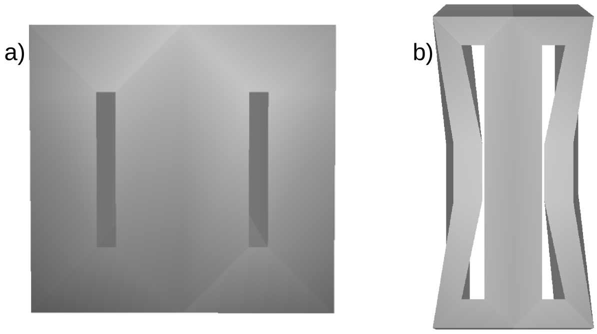

FIGURE 4.20: View in the x-y plane of the two magnet configurations. In configuration a) the air-gap is large enough anywhere along y to place a coil. Configuration b) has an air-gap close to 2 cm at y=0, and hence the program will create large enough air-gaps at the top and bottom of the magnet to accommodate the coils.

In addition, the following boundary conditions are imposed to assure a realistic implementation of the magnets:

- For every cross section in the xy-plane, the width of the iron is large enough everywhere to sustain the same magnetic flux;
- The minimum air-gap between opposite field directions is 2 cm;
- The minimum air-gap for accommodating coils in the plane perpendicular to the beam direction is 20 cm;
- The minimum air-gap between magnets along the beam direction is 10 cm;
- The mitred joints between volumes with horizontal and vertical fields are imposed to lower their magnetic reluctance [123].

The geometry optimization results in the shield layout shown in Figure 4.21, weighing 1845 tonnes, which does not include the supports.

To test the background with the prototype shielding in FairShip, only target, muon-shield, tracking stations and spectrometer magnet were included in the simulation. The last tracking station is located 64 m downstream of the last shielding magnet.

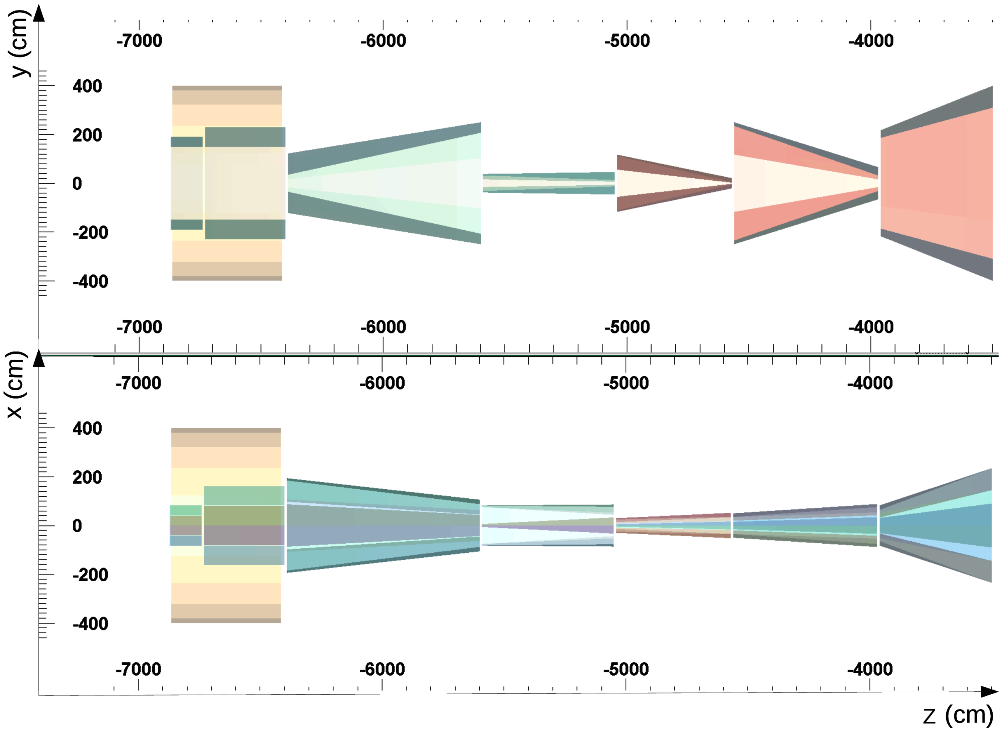

FIGURE 4.21: Geometric view of the optimized muon-shield, showing at the top, the z-y plane view, and at the bottom, the z-x plane view. SHiP software defines the origin of the coordinate system to be in the center of the decay vessel. Color shading is used to enhance the contrast between different magnetic field orientations.

The simulation is first run with all the material of the shield in place, but with the magnetic field switched off. This results in $\sim 3.1 \times 10^9$ muons which traverse the last tracking station during one SPS spill of 4×10^{13} POT. Switching on the magnetic field reduces this rate to $\sim 3.0 \times 10^5$ muons/s, of which $\sim 6.5 \times 10^4$ have momenta larger than 3 GeV/c. These muon rates are sufficiently low to cause insignificant background levels in the experiment.

Examining the muons reaching the last tracking station reveals that they are mainly due to two effects (which are not included in the optimization procedure), namely catastrophic energy loss and very large scattering angles.

4.6 Neutrino background estimation

All the sensitivities plots described in Section 4.3.2 are calculated under the assumption of having negligible background in 5 years of running. Therefore, the background rejection is key for the SHiP experiment. The neutrino background is the most dangerous one. The rejecting of neutrino induced background was studied in the context of this thesis.

A sketch of neutrino background, compared to signal is depicted in Figure 4.22. Neutrinos will originate mostly in the target immediately after the proton-proton collision. As they interact weakly, nearly all of them will reach the decay volume without being affected by the hadron absorber or the muon-shield. Neutrinos can interact inelastically in the vicinity of the decay volume and produce short and long-lived neutral particles which may enter the decay volume and mimic the signal. It is crucial for the experiment to be able to reject such background events based only on their topological difference compared to signal events.

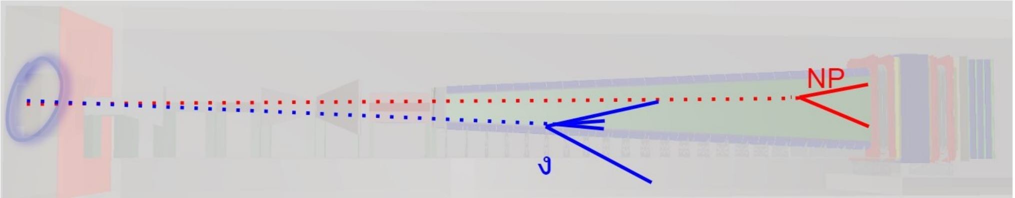

FIGURE 4.22: Illustration of neutrino interactions in the decay volume.

4.6.1 Neutrino background calculation

Neutrino backgrounds are simulated with the FairShip framework. The interaction of particles with the material is implemented with GEANT4. The initial proton-nucleon collision is modelled in the Pythia8 generator, and its output is transferred to GEANT4 to simulate detector response. Until recently, GEANT4 was not able to simulate neutrino interactions. Therefore, the software GENIE is used to simulate the neutrino charged current and neutral current interactions with the detector material. After that, the interaction products are further processed by GEANT4. So the whole neutrino simulation procedure can be split into four steps:

- The simulation of POT interactions is performed using Pythia8 and the momentum distribution of out-coming neutrinos is extracted. The momentum distribution for muon neutrinos is shown in Figure 4.23.
- The obtained spectrum of neutrinos is processed with GENIE to generate neutrino interactions with the material.
- As output of GENIE we have a set of particles produced in interactions which we pass to the geometry in GEANT4. We force our particles to interact in the z-region only between SND and second tracking station to maximise the background interactions in the area of interest.
- Using a P/P_T distribution, we position our event in the geometry

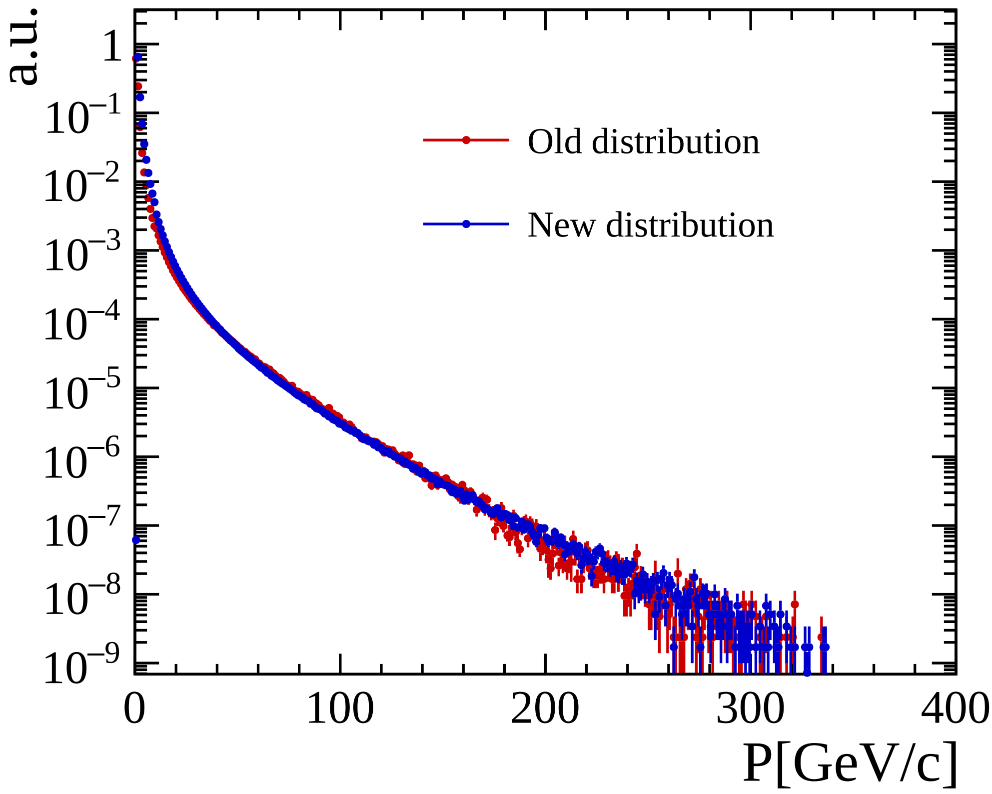

FIGURE 4.23: Momentum distribution of muon neutrino out of Pythia8 POT simulation. Old distribution corresponds to the POT emulations at TP time; new simulations have higher statistics and more data with two energy cuts of 1 GeV and 10 GeV

based on weighting events with the neutrino interaction probability. The weight of each event is given by $\sum \rho \cdot l$, where ρ is the density of the material in the neutrino path and l is path length. The geometrical distribution of neutrino interactions is shown in Figure 4.24.

The number of neutrino interactions can be calculated as:

$$N^{s}_{interactions} = \sum weight_i,$$

where

$$weight_i = \frac{\rho_i \cdot L_i \cdot N_A \cdot N_{nu} \cdot <\sigma> \cdot E_{\nu}}{N_{generated}}$$

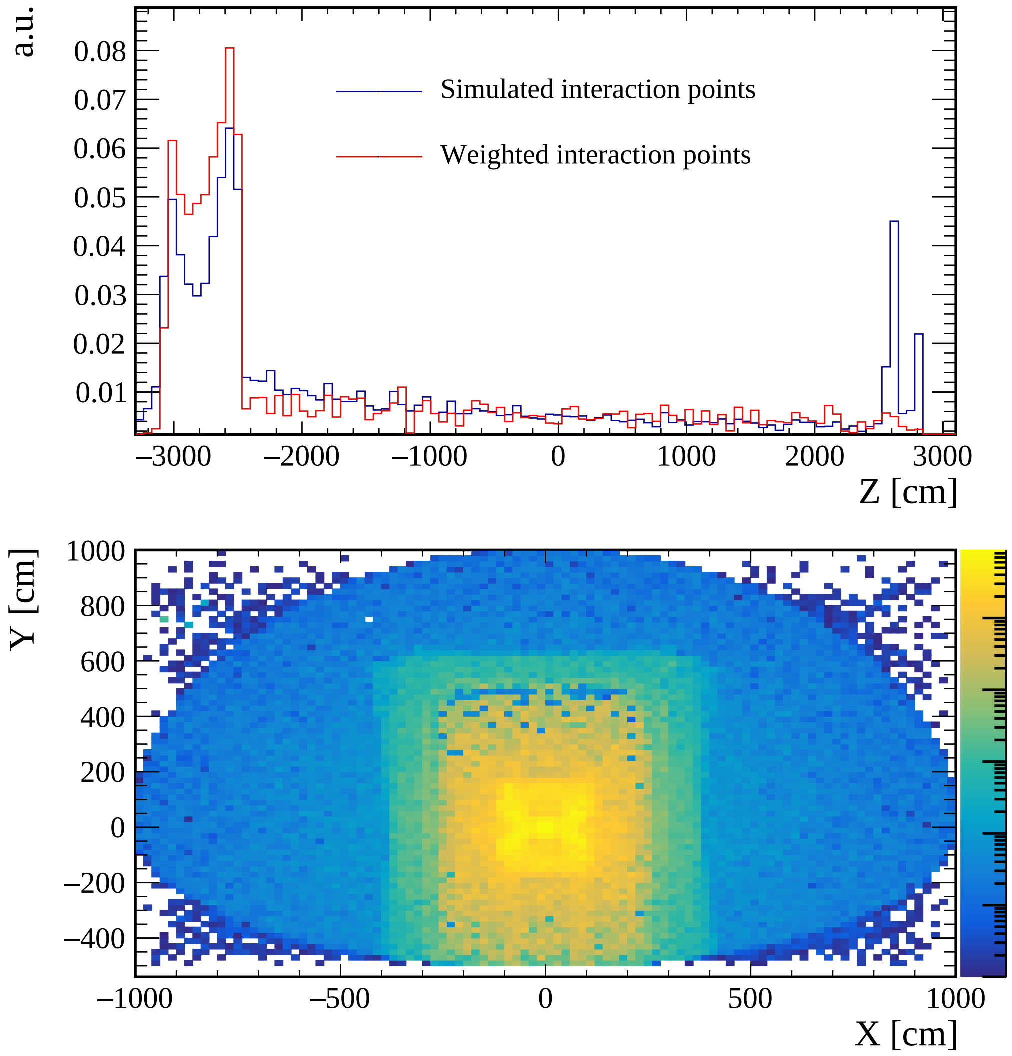

FIGURE 4.24: Spatial position of neutrino interaction points in Z dimension (top) and X-Y dimension (bottom).

Here,

- $N_A = 6.022 \cdot 10^{23}$ is an Avogadro constant.
- $N_{generated} = 1.5 \cdot 10^8$ is a number of simulated interactions.
- $N_{nu} = 4.51 \cdot 10^{11} \cdot \frac{2 \cdot 10^{20}}{5 \cdot 10^{13}}$ is a number of expected neutrinos in 5 years taken from the Pythia8 simulation.
- E_ν is a neutrino energy taken from the Pythia8 simulation.

- $< \sigma >$ is a neutrino cross-section at a given energy taken from the Particle Data Group.

In the technical proposal a conservative estimation of the vacuum requirement was used, since it was calculated that a pressure of 10^{-6} bar would lead to less than one neutrino scattering event in the air inside the vessel. Keeping this level of vacuum is challenging, therefore we studied the possibility to relax this requirement. We have generated and analysed a large sample of neutrino interactions in the air inside the vessel. We calculated the number of background candidates as function of the pressure, where a background candidate is defined as a vertex of two charged particles going through the spectrometer. We have found that the air pressure requirement can be relaxed to 10^{-3} bar.

The number of neutrino interactions in 5 years of running was estimated to be $2.2 \cdot 10^7$ using the formula presented before, which is seven times greater than the generated number of events. For this simulation, only the region up to the cavern walls was used, as it was shown in a previous simulation that neutrino induced background from cavern walls can be neglected.

The expected number of background candidates before the selection is $6.5 \cdot 10^4$. Most of these background events are produced in the SND detector, entrance window and wall elements of the decay volume. For this reason a significant fraction of background events can be rejected using veto systems.

Background events due to neutrino interactions have in general worse quality of reconstruction. Applying the basic selection from Table 4.1 together with vetoing results in zero background while keeping 65% of signal for both, fully and partially reconstructed events. Moreover, we

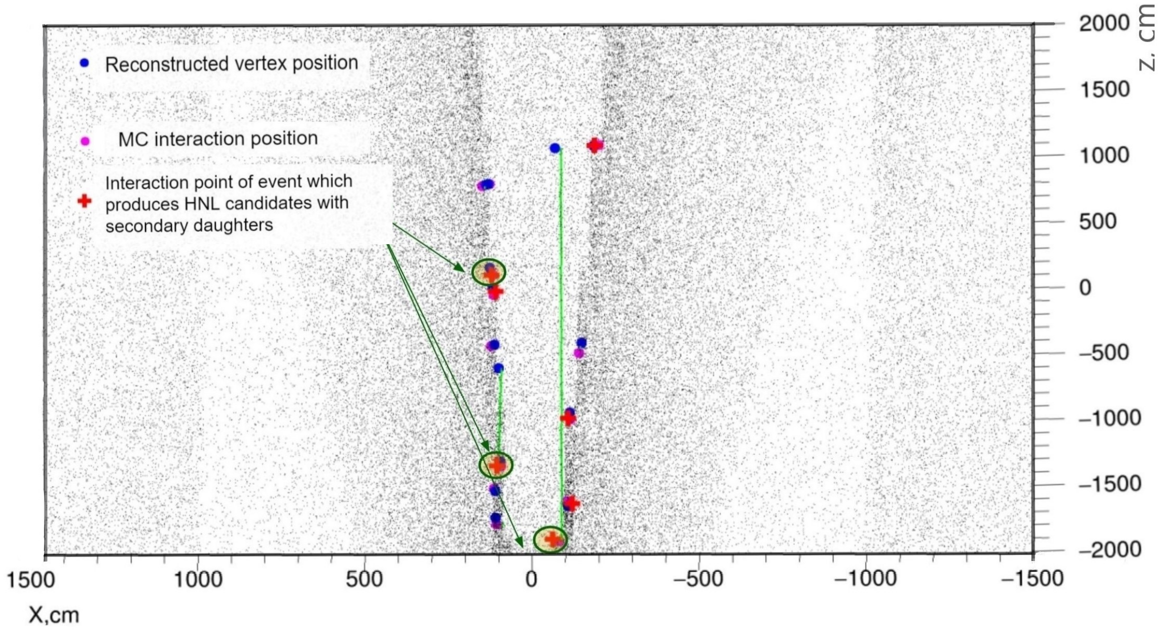

FIGURE 4.25: Position of reconstructed vertices and actual interaction point for events which survive basic selection.

can retain this performance with no use of the information from the SBT for fully reconstructed candidates.

In the case of partially reconstructed events, we cannot preserve a background of 0 using only the kinematic topology. However, reconstructed vertices of the remaining candidates tend to stay close to the decay volume walls, as they are caused by short-lived particles originated from neutrino interactions inside walls (see Figure 4.25). Therefore, we can apply an additional selection based on the position of reconstructed vertices inside the decay volume.

Long-lived particles with a high multiplicity form vertices which are located far away from walls. Since vetoing the full SBT is impractical, we studied the correlation between the Z-position of the closest hit in the SBT and the Z-position of the reconstructed vertex which is shown in Figure 4.26. Therefore, we can veto neutrino interaction events by looking on the activity in the proximity of the reconstructed vertex.

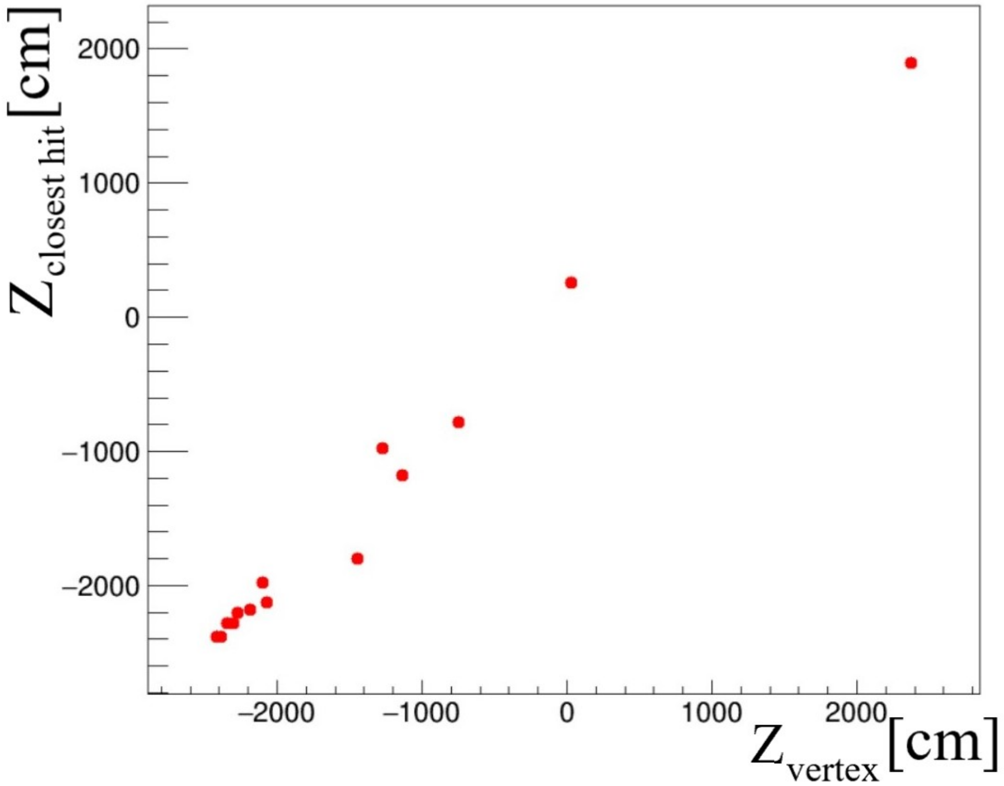

FIGURE 4.26: Correlation between the Z-position of the closest hit in SBT and Z-position of the reconstructed vertex.

The remaining background, in case of avoiding vetoing the full SBT, consists of the event type shown in Figure 4.27, *i.e.* photon conversions in the material. It can be easily eliminated by requiring the invariant mass of the pair to be larger than 100 MeV/c^2. The only background left is caused by misidentification of particles and depends on the efficiency of the particle identification system. Nevertheless, these studies have shown that we can keep the background at the level of less than 0.1 event. The summary of the suppression level of the different selection criteria is shown in Table 4.2.

Our studies have shown that even under these extreme conditions, we can achieve less than one neutrino event in 5 years, which allows us to increase the pressure to 1 mbar while keeping a background at a negligible level.

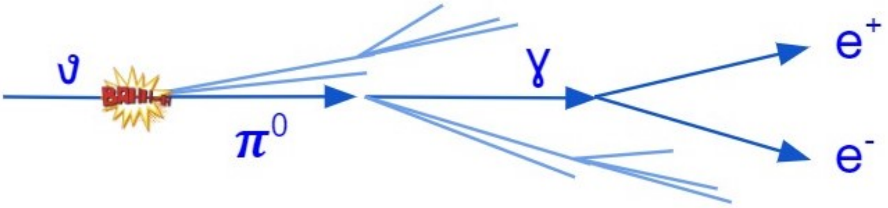

FIGURE 4.27: Category of neutrino induced background events which survive the basic selection + SBT around the vertex.

Selection Stage	$N_{candidates}$
Reconstructed candidates	65612
Basic selection	135
PID	12
Exclude area next to material	8
Invariant mass > 100 MeV/c^2	0.25
SBT signal around the vertex	0.05

TABLE 4.2: Neutrino background level in five years for different selection stages.

4.7 Summary and outlook

I have studied the important aspects regarding the SHiP experiment: the optimisation of the muon system and the estimation of the neutrino background. A magnetic deflecting system for muons has been presented, which provides the sufficient reduction of muons for the SHiP experiment. The design is optimized to reduce muon background while keeping the shield as short and light, as possible. The optimized geometry of the shield is 34 m long and its weight is 1845 tonnes not including its supports. It is found that a large flux of electrons and photons is produced by the muons traversing the magnets. Their momentum is typically below the 1 GeV/c, and hence they do not constitute a source of background directly. However, the SHiP decay vessel is surrounded by detectors to tag any charged particle entering the vessel. Moreover, the emulsion target upstream is also sensitive to low energy electrons that may spoil its reconstruction capability. Hence, the flux of these particles has to also be controlled to ensure an effective use of these surround taggers. The muons which do traverse the system are coming from physics processes which have not been included in the optimization program.

Since the work presented here was completed, the muon-shield design has been re-optimised. This re-optimisation resulted in 25% lighter configuration with a field of 1.7 T [112]. Further iterations of the optimisation will be required as the experimental R&D progresses.

The neutrino background studies showed that we expect to have around $2.2 \cdot 10^7$ neutrino interactions in 5 years of the experiment running which will lead to $6.5 \cdot 10^4$ background events. It was shown that this rate can be reduced to a negligible level using a set of selection criteria.

Conclusion

Several different projects have been studied within the framework of the thesis, the results of which were presented in this manuscript. All these projects, however, were united by one idea - the search for the new physics. There were two projects discussed concerning the existing LHCb experiment. The first project is more hardware based, and dedicated to the development of the system to test newly produced SALT128 ASICs designed for the LHCb Upgrade. The second project is the semileptonic measurement $R(\Lambda_c) = \frac{\mathcal{B}(\Lambda_b^0 \to \Lambda_c^+ \tau^- \overline{\nu}_\tau)}{\mathcal{B}(\Lambda_b^0 \to \Lambda_c^+ \mu^- \overline{\nu}_\mu)}$ that was done using the data collected by the LHCb experiment in 2016. The result is still blinded, however the analysis is well advanced and expected to be wrapped up in 2021 with a final fine tunings and calculation of systematics. The final project is a simulation study for the newly proposed SHiP experiment dedicated to search for the new physics in the high intensity region. The optimisation of the muon deflecting system and estimation of reduction abilities of neutrino background are the main topics of interest under the scope of the SHiP chapter.

As we do not know the mass/coupling of NP, it is important to search in every possible direction for it. This is one of the main conclusions of this thesis. Even if the flavour anomalies disappear with larger datasets, an important region of NP parameter space will be excluded, models of NP will have been improved and the orthodoxy of interesting future NP directions will have been challenged. This is by itself is a great motivation to continue the endeavour to search for NP in as many ways as possible and perhaps, if we are lucky, a revolution is around the corner.

Appendix

Simulation - data comparisons

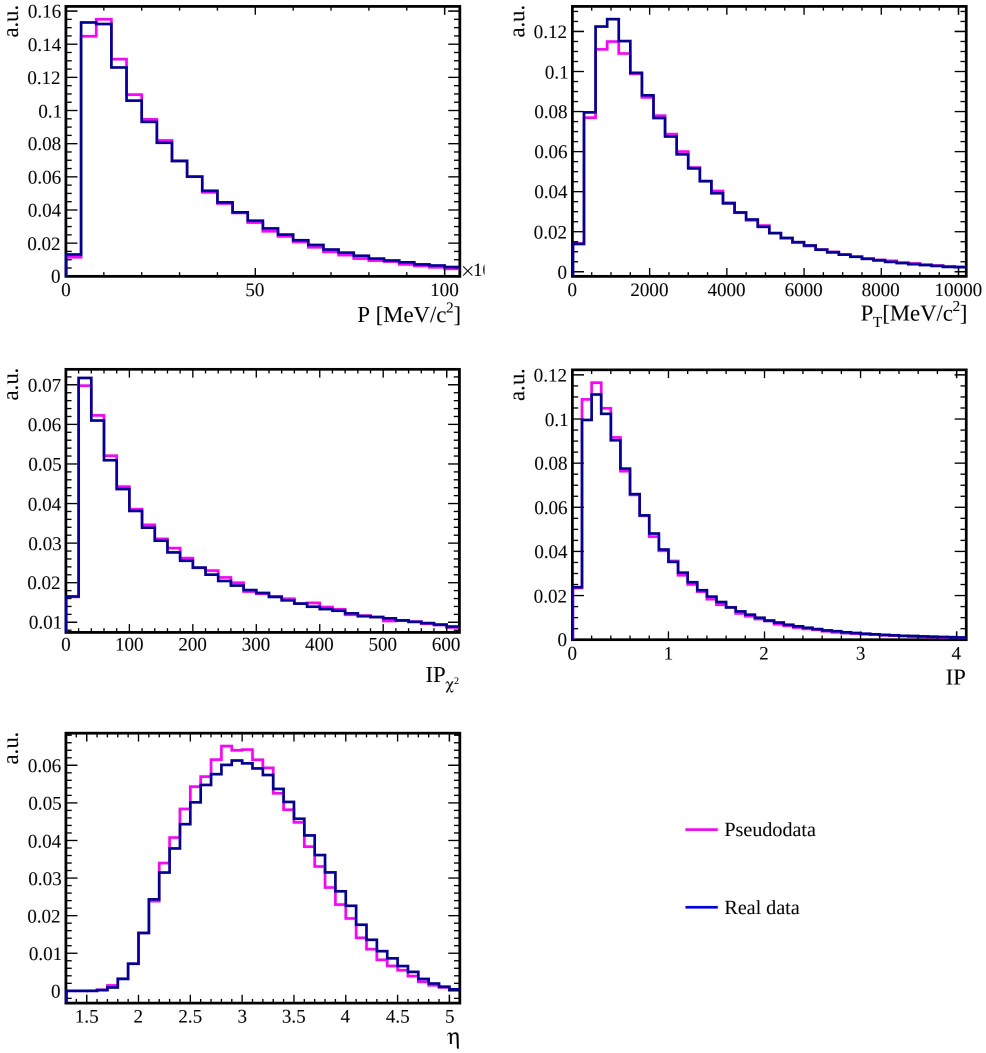

FIGURE 1: Simulation - data comparison for the muon distributions in $R(\Lambda_c)$ analysis.

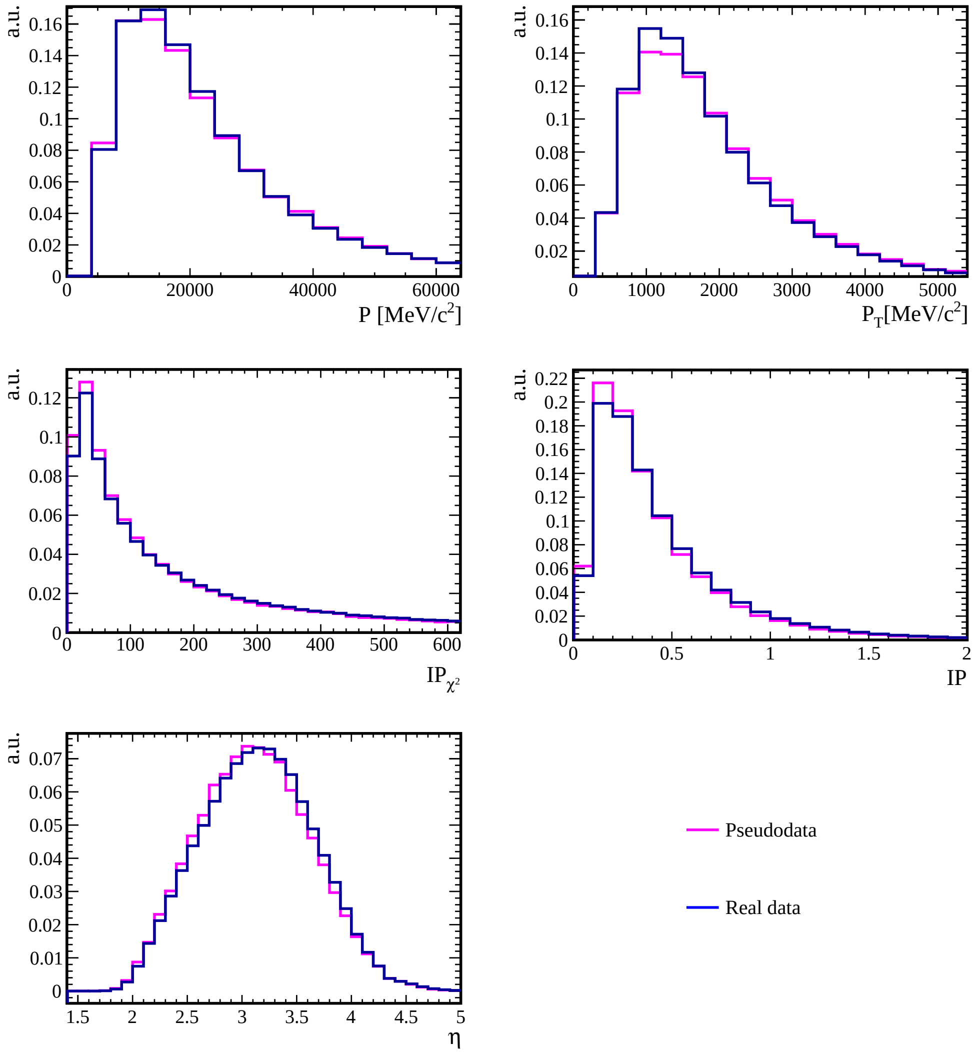

FIGURE 2: Simulation - data comparison for the kaon distributions in $R(\Lambda_c)$ analysis.

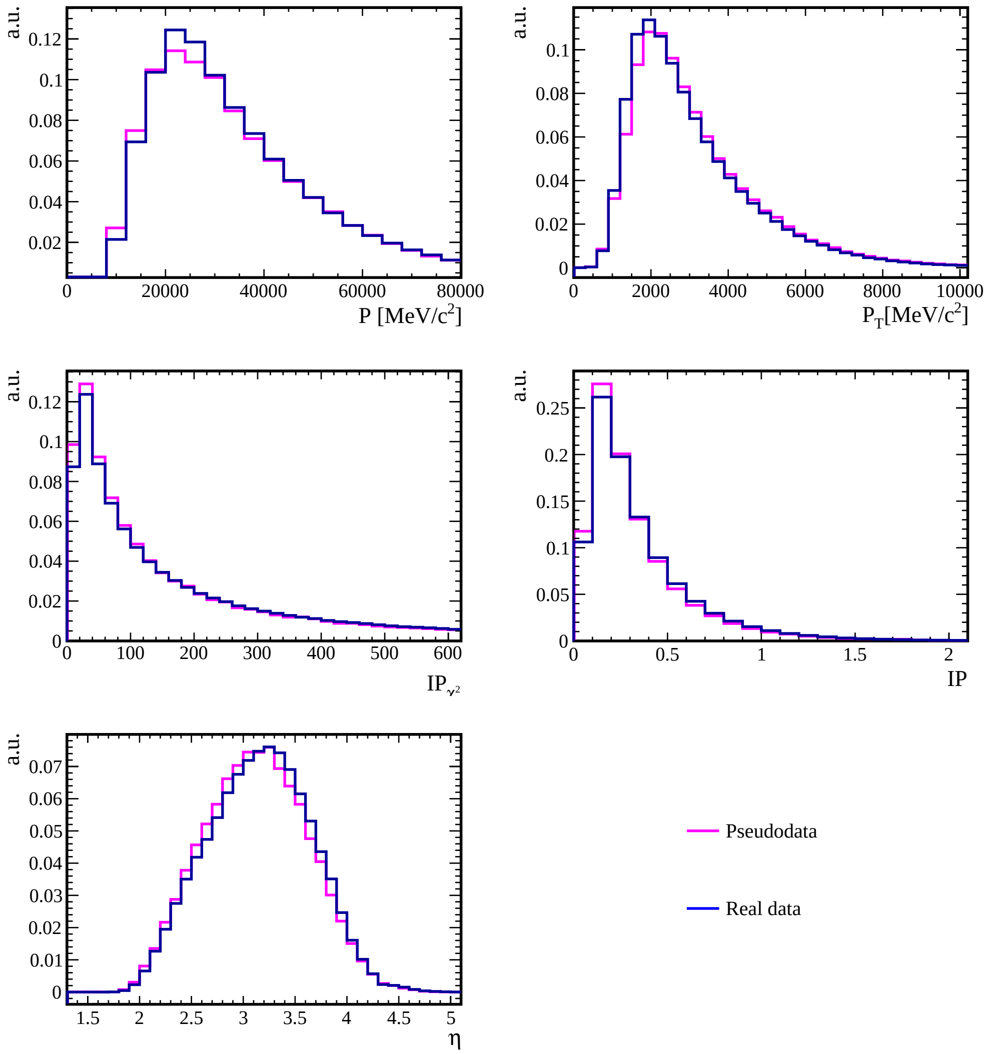

FIGURE 3: Simulation - data comparison for the proton distributions in $R(\Lambda_c)$ analysis.

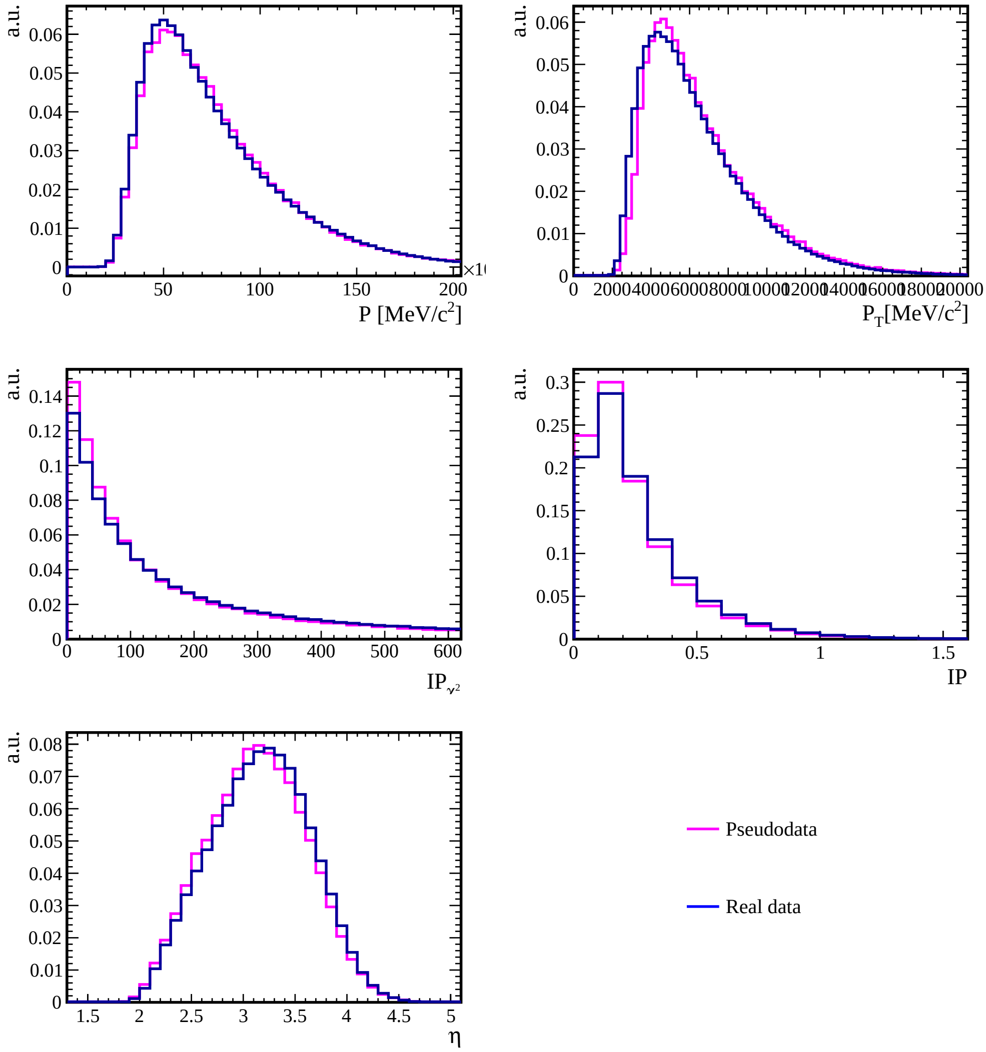

FIGURE 4: Simulation - data comparison for the Λ_c distributions in $R(\Lambda_c)$ analysis.

Aknowledgements

There are so many people I would like to thank. I am at this point thanks to all the great people who have taught me, helped me, encouraged me and supported me.

I want to express my deep gratitude to Prof. Dr. Nicola Serra for giving me the chance to work in this great group and for all the exciting topics. Your enthusiasm is contagious and inspiring. I have especially enjoyed the projects we have worked on closely together.

Thanks also to Dr. Patrick Owen for introducing me to the semileptonic world, for all the spontaneous blackboard discussions, insightful suggestions, and for co-founding a cycling club. I would like to thank PD Dr. Olaf Steinkamp for reading the SALT chapter of my dissertation and for all his advice. Special thanks to Dr. Oliver Lantwin for proofreading the SHiP chapter.

I would especially like to thank Dr. Carlos Abellan Beteta for introducing me to the hardware and FPGA world. I really appreciate your patience and everything I learned from you. And sorry for all the burnt resistors.

I am grateful for all the people I met during my PhD at the Physik-Institut, some of whom have become my really good friends. Knowing and having you made this time not only an amazing scientific journey, but also an enjoyable life.

I would also like to thank the people who did not contribute to my PhD directly, but without whom I would not have been here in the first place.

Prof. Dr. Ivan Kisel, thank you for giving me the opportunity to work in your group and for showing this scared, shy girl that she can achieve something greater. I am deeply in debt to Dr. Maksym Zyzak. I thank you for the time you spent with me during my internship. I consider it one of the most important turning points in my life. You taught me how to figure things out, even if it made me cry into my pillow for the first nights. I came back to Kyiv as a different person. I will always be incredibly grateful for that.

I would like to express my sincere gratitude to Dr. Hans Dijkstra. You have awakened in me a love for science. Not only have you been my mentor, but you have also supported me as a person. I am incredibly lucky to have had the opportunity to do my internship with you. The knowledge and guidances you have given me cannot be overstated.

Last but not least, I would like to thank my parents. For their support. For the way they raised me. For all the scientific discussions at the kitchen table. For sometimes pushing me beyond my limits.

Bibliography

[1] Hyun Min Lee. *Lectures on Physics Beyond the Standard Model*. 2019. arXiv: `1907.12409 [hep-ph]`.

[2] Julian Schwinger. "On Quantum-Electrodynamics and the Magnetic Moment of the Electron". In: *Phys. Rev.* 73 (4 1948), pp. 416–417. DOI: `10.1103/PhysRev.73.416`. URL: `https://link.aps.org/doi/10.1103/PhysRev.73.416`.

[3] G. Aad et al. "Observation of a new particle in the search for the Standard Model Higgs boson with the ATLAS detector at the LHC". In: *Physics Letters B* 716.1 (2012), 1–29. ISSN: 0370-2693. DOI: `10.1016/j.physletb.2012.08.020`. URL: `http://dx.doi.org/10.1016/j.physletb.2012.08.020`.

[4] S. Chatrchyan et al. "Observation of a new boson at a mass of 125 GeV with the CMS experiment at the LHC". In: *Physics Letters B* 716.1 (2012), 30–61. ISSN: 0370-2693. DOI: `10.1016/j.physletb.2012.08.021`. URL: `http://dx.doi.org/10.1016/j.physletb.2012.08.021`.

[5] Wikipedia contributors. *Standard Model — Wikipedia, The Free Encyclopedia*. 2021. URL: `https://en.wikipedia.org/w/index.php?title=Standard_Model&oldid=1022657783`.

[6] P.A. Zyla et al. "Review of Particle Physics". In: *PTEP* 2020.8 (2020), p. 083C01. DOI: `10.1093/ptep/ptaa104`.

[7] W. M. Alberico and S. M. Bilenky. *Neutrino Oscillations, Masses and Mixing*. 2003. arXiv: `hep-ph/0306239 [hep-ph]`.

[8] V. C. Rubin, Jr. Ford W. K., and N. Thonnard. “Rotational properties of 21 SC galaxies with a large range of luminosities and radii, from NGC 4605 (R=4kpc) to UGC 2885 (R=122kpc).” In: 238 (1980), pp. 471–487. DOI: 10.1086/158003. URL: https://ui.adsabs.harvard.edu/abs/1980ApJ...238..471R.

[9] Laurent Canetti, Marco Drewes, and Mikhail Shaposhnikov. “Matter and antimatter in the universe”. In: *New Journal of Physics* 14.9 (2012), p. 095012. ISSN: 1367-2630. DOI: 10.1088/1367-2630/14/9/095012. URL: http://dx.doi.org/10.1088/1367-2630/14/9/095012.

[10] Michael J. Mortonson, David H. Weinberg, and Martin White. *Dark Energy: A Short Review*. 2013. arXiv: 1401.0046 [astro-ph.CO].

[11] George Lafferty and J P Lees. “Measurement of an Excess of $\bar{B} \to D^{(*)}\tau^-\bar{\nu}_\tau$ Decays and Implications for Charged Higgs Bosons”. English. In: *Physical Review D (Particles, Fields, Gravitation and Cosmology)* D88.7 (2013). ISSN: 1550-7998. DOI: 10.1103/PhysRevD.88.072012.

[12] M. Huschle et al. “Measurement of the branching ratio of $\bar{B} \to D^{(*)}\tau^-\bar{\nu}_\tau$ relative to $\bar{B} \to D^{(*)}\ell^-\bar{\nu}_\ell$ decays with hadronic tagging at Belle”. In: *Phys. Rev. D* 92.7 (2015), p. 072014. DOI: 10.1103/PhysRevD.92.072014. arXiv: 1507.03233 [hep-ex].

[13] R. Aaij et al. “Measurement of the Ratio of Branching Fractions $\mathcal{B}(\overline{B}^0 \to D^{*+}\tau^-\overline{\nu}_\tau)/\mathcal{B}(\overline{B}^0 \to D^{*+}\mu^-\overline{\nu}_\mu)$”. In: *Phys. Rev. Lett.* 115 (11 2015), p. 111803. DOI: 10.1103/PhysRevLett.115.111803. URL: https://link.aps.org/doi/10.1103/PhysRevLett.115.111803.

[14] J. P. Lees et al. “Evidence for an Excess of $\overline{B} \to D^{(*)}\tau^-\overline{\nu}_\tau$ Decays”. In: *Phys. Rev. Lett.* 109 (10 2012), p. 101802. DOI: 10.1103/

PhysRevLett.109.101802. URL: https://link.aps.org/doi/10.1103/PhysRevLett.109.101802.

[15] J. P. Lees et al. "Measurement of an excess of $\overline{B} \to D^{(*)}\tau^{-}\overline{\nu}_{\tau}$ decays and implications for charged Higgs bosons". In: *Phys. Rev. D* 88 (7 2013), p. 072012. DOI: 10.1103/PhysRevD.88.072012. URL: https://link.aps.org/doi/10.1103/PhysRevD.88.072012.

[16] Belle Collaboration et al. "Measurement of the branching ratio of $\bar{B} \to D^{(*)}\tau^{-}\bar{\nu}_{\tau}$ relative to $\bar{B} \to D^{(*)}\ell^{-}\bar{\nu}_{\ell}$ decays with hadronic tagging at Belle". In: *arXiv e-prints*, arXiv:1507.03233 (2015), arXiv:1507.03233. arXiv: 1507.03233 [hep-ex].

[17] S. Hirose et al. "Measurement of the τ Lepton Polarization and $R(D^{*})$ in the Decay $B^{-} \to D^{*}\tau^{-}\nu_{\tau}^{-}$". In: *Physical Review Letters* 118.21 (2017). ISSN: 1079-7114. DOI: 10.1103/physrevlett.118.211801. URL: http://dx.doi.org/10.1103/PhysRevLett.118.211801.

[18] S. Hirose et al. "Measurement of the τ lepton polarization and $R(D^{*})$ in the decay $B^{-} \to D^{*}\tau^{-}\nu_{\tau}^{-}$ with one-prong hadronic τ decays at Belle". In: *Physical Review D* 97.1 (2018). ISSN: 2470-0029. DOI: 10.1103/physrevd.97.012004. URL: http://dx.doi.org/10.1103/PhysRevD.97.012004.

[19] G. Caria et al. "Measurement of $R(D)$ and $R(D^{*})$ with a Semileptonic Tagging Method". In: *Physical Review Letters* 124.16 (2020). ISSN: 1079-7114. DOI: 10.1103/physrevlett.124.161803. URL: http://dx.doi.org/10.1103/PhysRevLett.124.161803.

[20] C.S. Kim et al. "Remarks on the Standard Model predictions for $R(D)$ and $R(D^{*})$". In: *Physical Review D* 95.1 (2017). ISSN: 2470-0029. DOI: 10.1103/physrevd.95.013003. URL: http://dx.doi.org/10.1103/PhysRevD.95.013003.

[21] Heavy Flavor Averaging Group et al. *Averages of b-hadron, c-hadron, and τ-lepton properties as of 2018*. 2019. arXiv: `1909.12524 [hep-ex]`.

[22] Gregory Ciezarek. "Searches for lepton number violation, and flavour violation beyond the Yukawa couplings at LHCb". Presented 10 Jun 2014. 2014. URL: `https://cds.cern.ch/record/1755654`.

[23] J. P. Lees et al. "Measurement of branching fractions and rate asymmetries in the rare decays $B \to K^{(*)}\ell^+\ell^-$". In: *Phys. Rev. D* 86 (3 2012), p. 032012. DOI: `10.1103/PhysRevD.86.032012`. URL: `https://link.aps.org/doi/10.1103/PhysRevD.86.032012`.

[24] The BELLE collaboration. "Test of lepton flavor universality and search for lepton flavor violation in $B \to K\ell\ell$ decays". In: *Journal of High Energy Physics* 2021.3 (2021), p. 105. ISSN: 1029-8479. DOI: `10.1007/JHEP03(2021)105`. URL: `https://doi.org/10.1007/JHEP03(2021)105`.

[25] LHCb collaboration et al. *Test of lepton universality in beauty-quark decays*. 2021. arXiv: `2103.11769 [hep-ex]`.

[26] R. Aaij et al. "Test of lepton universality with $B^0 \to K^{*0}\ell^+\ell^-$ decays". In: *Journal of High Energy Physics* 2017.8 (2017). ISSN: 1029-8479. DOI: `10.1007/jhep08(2017)055`. URL: `http://dx.doi.org/10.1007/JHEP08(2017)055`.

[27] R. Aaij et al. "Test of Lepton Universality Using $B^+ \to K^+\ell^+\ell^-$ Decays". In: *Physical Review Letters* 113.15 (2014). ISSN: 1079-7114. DOI: `10.1103/physrevlett.113.151601`. URL: `http://dx.doi.org/10.1103/PhysRevLett.113.151601`.

[28] R. Aaij et al. "Test of lepton universality with $B^0 \to K_0^*\ell^+\ell^-$ decays". In: *Journal of High Energy Physics* 2017.8 (2017). ISSN: 1029-8479. DOI: `10.1007/jhep08(2017)055`. URL: `http://dx.doi.org/10.1007/JHEP08(2017)055`.

[29] Sergey Alekhin et al. “A facility to search for hidden particles at the CERN SPS: the SHiP physics case”. In: *Reports on Progress in Physics* 79.12 (2016), p. 124201. ISSN: 1361-6633. DOI: 10.1088/0034-4885/79/12/124201. URL: http://dx.doi.org/10.1088/0034-4885/79/12/124201.

[30] A. Ringwald. *Axions and Axion-Like Particles*. 2014. arXiv: 1407.0546 [hep-ph].

[31] Atakan Akmete. “Sensitivity of the SHiP Experiment to Hidden Particles at the CERN SpS”. MA thesis. Middle East Tech. U., Ankara, 2020.

[32] Oleg Lebedev, Hyun Min Lee, and Yann Mambrini. “Vector Higgs portal dark matter and the invisible Higgs”. In: *Physics Letters B* 707.5 (2012), 570–576. ISSN: 0370-2693. DOI: 10.1016/j.physletb.2012.01.029. URL: http://dx.doi.org/10.1016/j.physletb.2012.01.029.

[33] Bob Holdom. “Two U(1)’s and ϵ charge shifts”. In: *Physics Letters B* 166.2 (1986), pp. 196 –198. ISSN: 0370-2693. DOI: https://doi.org/10.1016/0370-2693(86)91377-8. URL: http://www.sciencedirect.com/science/article/pii/0370269386913778.

[34] Vanda Silveira and A. Zee. “Scalar Phantoms”. In: *Physics Letters B* 161.1 (1985), pp. 136 –140. ISSN: 0370-2693. DOI: https://doi.org/10.1016/0370-2693(85)90624-0. URL: http://www.sciencedirect.com/science/article/pii/0370269385906240.

[35] Matthew J. Strassler and Kathryn M. Zurek. “Echoes of a hidden valley at hadron colliders”. In: *Physics Letters B* 651.5-6 (2007), 374–379. ISSN: 0370-2693. DOI: 10.1016/j.physletb.2007.06.055. URL: http://dx.doi.org/10.1016/j.physletb.2007.06.055.

[36] Robert Schabinger and James D. Wells. “Minimal spontaneously broken hidden sector and its impact on Higgs boson physics at the CERN Large Hadron Collider”. In: *Physical Review D* 72.9 (2005). ISSN: 1550-2368. DOI: 10.1103/physrevd.72.093007. URL: http://dx.doi.org/10.1103/PhysRevD.72.093007.

[37] Brian Patt and Frank Wilczek. “Higgs-field portal into hidden sectors”. In: (May 2006). arXiv: hep-ph/0605188.

[38] Iryna Boiarska et al. “Phenomenology of GeV-scale scalar portal”. In: *Journal of High Energy Physics* 2019.11 (2019). ISSN: 1029-8479. DOI: 10.1007/jhep11(2019)162. URL: http://dx.doi.org/10.1007/JHEP11(2019)162.

[39] Gaia Lanfranchi. “Sensitivity of the SHiP experiment to a light scalar particle mixing with the Higgs”. In: (2017). URL: https://cds.cern.ch/record/2243034.

[40] Glennys R. Farrar and M. E. Shaposhnikov. “Baryon asymmetry of the Universe in the minimal standard model”. In: *Physical Review Letters* 70.19 (1993), 2833–2836. ISSN: 0031-9007. DOI: 10.1103/physrevlett.70.2833. URL: http://dx.doi.org/10.1103/PhysRevLett.70.2833.

[41] Buchmüller. In: *International Journal of Modern Physics A* 15 (2000), p. 5047. ISSN: 0217-751X. DOI: 10.1016/s0217-751x(00)00293-5. URL: http://dx.doi.org/10.1016/S0217-751X(00)00293-5.

[42] Yoshitaka Kuno and Yasuhiro Okada. “Muon decay and physics beyond the standard model”. In: *Reviews of Modern Physics* 73.1 (2001), 151–202. ISSN: 1539-0756. DOI: 10.1103/revmodphys.73.151. URL: http://dx.doi.org/10.1103/RevModPhys.73.151.

[43] T.S. Kosmas, G.K. Leontaris, and J.D. Vergados. “Lepton flavor non-conservation”. In: *Progress in Particle and Nuclear Physics* 33 (1994), 397–447. ISSN: 0146-6410. DOI: 10.1016/0146-6410(94)

90047-7. URL: http://dx.doi.org/10.1016/0146-6410(94)90047-7.

[44] Simone Bifani et al. "Review of lepton universality tests in B decays". In: *Journal of Physics G: Nuclear and Particle Physics* 46.2 (2018), p. 023001. ISSN: 1361-6471. DOI: 10.1088/1361-6471/aaf5de. URL: http://dx.doi.org/10.1088/1361-6471/aaf5de.

[45] Rodrigo Alonso, Benjamín Grinstein, and Jorge Martin Camalich. "Lifetime of B_c^- Mesons Constrains Explanations for Anomalies in $B \to D^{(*)}\tau\nu_\tau$". In: *Physical Review Letters* 118.8 (2017). ISSN: 1079-7114. DOI: 10.1103/physrevlett.118.081802. URL: http://dx.doi.org/10.1103/PhysRevLett.118.081802.

[46] Rodrigo Alonso, Benjamín Grinstein, and Jorge Martin Camalich. "Lifetime of B_c^- Mesons Constrains Explanations for Anomalies in $B \to D^{(*)}\tau\nu$". In: *Phys. Rev. Lett.* 118 (8 2017), p. 081802. DOI: 10.1103/PhysRevLett.118.081802. URL: https://link.aps.org/doi/10.1103/PhysRevLett.118.081802.

[47] Diego Guadagnoli. "Flavor anomalies on the eve of the Run-2 verdict". In: *Modern Physics Letters A* 32.07 (2017), p. 1730006. ISSN: 1793-6632. DOI: 10.1142/s0217732317300063. URL: http://dx.doi.org/10.1142/S0217732317300063.

[48] Darius A. Faroughy, Admir Greljo, and Jernej F. Kamenik. "Confronting lepton flavor universality violation in B decays with high-p_T tau lepton searches at LHC". In: *Physics Letters B* 764 (2017), 126–134. ISSN: 0370-2693. DOI: 10.1016/j.physletb.2016.11.011. URL: http://dx.doi.org/10.1016/j.physletb.2016.11.011.

[49] David London. *Anomalies in B Decays: A Sign of New Physics?* 2019. arXiv: 1911.06238 [hep-ph].

[50] The LHCb Collaboration. "The LHCb Detector at the LHC". In: *Journal of Instrumentation* 3.08 (2008), S08005–S08005. DOI: 10.1088/1748-0221/3/08/s08005.

[51] R Antunes-Nobrega et al. *LHCb reoptimized detector design and performance: Technical Design Report*. Technical Design Report LHCb. Geneva: CERN, 2003. URL: http://cds.cern.ch/record/630827.

[52] I Bediaga et al. *Framework TDR for the LHCb Upgrade: Technical Design Report*. Tech. rep. CERN-LHCC-2012-007. LHCb-TDR-12. 2012. URL: http://cds.cern.ch/record/1443882.

[53] Roel Aaij et al. *Physics case for an LHCb Upgrade II - Opportunities in flavour physics, and beyond, in the HL-LHC era*. Tech. rep. ISBN 978-92-9083-494-6. Geneva: CERN, 2018. DOI: 10347/15157. arXiv: 1808.08865. URL: https://cds.cern.ch/record/2636441.

[54] R. Aaij et al. "Design and performance of the LHCb trigger and full real-time reconstruction in Run 2 of the LHC". In: *Journal of Instrumentation* 14.04 (2019), P04013–P04013. ISSN: 1748-0221. DOI: 10.1088/1748-0221/14/04/p04013. URL: http://dx.doi.org/10.1088/1748-0221/14/04/P04013.

[55] LHCb Collaboration. *LHCb VELO Upgrade Technical Design Report*. Tech. rep. CERN-LHCC-2013-021. LHCB-TDR-013. 2013. URL: https://cds.cern.ch/record/1624070.

[56] P R Barbosa-Marinho et al. *LHCb VELO (VErtex LOcator): Technical Design Report*. Technical Design Report LHCb. Geneva: CERN, 2001. URL: https://cds.cern.ch/record/504321.

[57] A. Gallas. "The LHCb upgrade". In: *Physics Procedia* 37 (Dec. 2012), pp. 151–163. DOI: 10.1016/j.phpro.2012.02.364.

[58] LHCb Collaboration. *LHCb Tracker Upgrade Technical Design Report*. Tech. rep. CERN-LHCC-2014-001. LHCB-TDR-015. 2014. URL: https://cds.cern.ch/record/1647400.

[59] José Mazorra de Cos et al. "PACIFIC: SiPM readout ASIC for LHCb upgrade". In: *Nucl. Instrum. Methods Phys. Res., A* 912 (2017), 354–358. 5 p. DOI: `10.1016/j.nima.2017.12.044`. URL: `https://cds.cern.ch/record/2680127`.

[60] S Löchner and M Schmelling. *The Beetle Reference Manual - chip version 1.3, 1.4 and 1.5*. Tech. rep. LHCb-2005-105. CERN-LHCb-2005-105. Geneva: CERN, 2006. URL: `https://cds.cern.ch/record/1000429`.

[61] Espen Eie Bowen. "Upstream Tracking and the Decay $B^0 \to K^+\pi^-\mu^+\mu^-$ at the LHCb Experiment". Presented 26 Jan 2017. 2016. URL: `https://cds.cern.ch/record/2261918`.

[62] Manuel Franco Sevilla. "New silicon trackers for a triggerless LHCb : the Vertex Locator (VELO) and the Upstream Tracker (UT). 29th International Workshop on Vertex Detectors". In: (2020). URL: `https://cds.cern.ch/record/2740971`.

[63] Miroslaw Firlej et al. *SALT3 chip documentation*. Tech. rep. 2019. URL: `https://twiki.cern.ch/twiki/pub/LHCb/StripAsic/salt_v5_spec.pdf`.

[64] K. Wyllie et al. "Electronics Architecture of the LHCb Upgrade". In: LHCb-PUB-2011-011, CERN-LHCb-PUB-2011-011 (2011).

[65] F Alessio and R Jacobsson. *Readout Control Specifications for the Front-End and Back-End of the LHCb Upgrade*. Tech. rep. LHCb-PUB-2012-017. CERN-LHCb-PUB-2012-017. LHCb-INT-2012-018. Geneva: CERN, 2014. URL: `https://cds.cern.ch/record/1491666`.

[66] Altera Corporation. *Arria V and Cyclone V Design Guideness*. Tech. rep. Altera, 2016. URL: `https://www.intel.me/content/dam/www/programmable/us/en/pdfs/literature/an/an662.pdf`.

[67] Otavio Salvador and Daiane Angolini. *Embedded Linux Development with Yocto Project*. Packt Publishing, 2014. ISBN: 1783282339.

[68] Texas Instruments. *Ultra-Small, Low-Power, 16-Bit Analog-to-Digital Converter with Internal Reference*. Tech. rep. Texas Instruments, 2009. URL: `https://cdn-shop.adafruit.com/datasheets/ads1115.pdf`.

[69] Texas Instruments. *Zero-Drift, Bi-Directional CURRENT/POWER MONITOR with I^2C Interface*. Tech. rep. Texas Instruments, 2011. URL: `https://cdn-shop.adafruit.com/datasheets/ina219.pdf`.

[70] K. Kinoshita. "Reflections on beauty1Talk presented at A Symposium in Honor of the 65th Birthday of Professor P. Buford Price.1". In: *New Astronomy Reviews* 42.3 (1998), pp. 263–270. ISSN: 1387-6473. DOI: `https://doi.org/10.1016/S1387-6473(98)00011-6`. URL: `https://www.sciencedirect.com/science/article/pii/S1387647398000116`.

[71] M. Feindt et al. "A hierarchical NeuroBayes-based algorithm for full reconstruction of B mesons at B factories". In: *Nuclear Instruments and Methods in Physics Research Section A: Accelerators, Spectrometers, Detectors and Associated Equipment* 654.1 (2011), pp. 432–440. ISSN: 0168-9002. DOI: `https://doi.org/10.1016/j.nima.2011.06.008`. URL: `https://www.sciencedirect.com/science/article/pii/S0168900211011193`.

[72] R. Aaij et al. "Measurement of the Ratio of the $B^0 \to D^{*-}\tau^+\nu_\tau$ and $B^0 \to D^{*-}\mu^+\nu_\mu$ Branching Fractions Using Three-Prong τ Lepton Decays". In: *Physical Review Letters* 120.17 (2018). ISSN: 1079-7114. DOI: `10.1103/physrevlett.120.171802`. URL: `http://dx.doi.org/10.1103/PhysRevLett.120.171802`.

[73] Monika Blanke et al. “Impact of polarization observables and $B_c \to \tau\nu$ on new physics explanations of the $b \to c\tau\nu$ anomaly”. In: *Physical Review D* 99.7 (2019). ISSN: 2470-0029. DOI: 10.1103/physrevd.99.075006. URL: http://dx.doi.org/10.1103/PhysRevD.99.075006.

[74] R. Aaij et al. “Design and performance of the LHCb trigger and full real-time reconstruction in Run 2 of the LHC”. In: *Journal of Instrumentation* 14.04 (2019), P04013–P04013. ISSN: 1748-0221. DOI: 10.1088/1748-0221/14/04/p04013. URL: http://dx.doi.org/10.1088/1748-0221/14/04/P04013.

[75] Roel Aaij et al. *Optimization of the muon reconstruction algorithms for LHCb Run 2*. Tech. rep. Geneva: CERN, 2017. URL: https://cds.cern.ch/record/2253050.

[76] Phoebe Hamilton, Hassan Jawahery, and Gregory Max Ciezarek. “Simultaneous extraction of the branching fraction ratios $\mathcal{R}(D)$ and $\mathcal{R}(D^*)$ with the Run 1 Dataset using the $\tau^+ \to \mu^+\nu_\mu\overline{\nu}_\tau$ decay”. In: (2020). URL: https://cds.cern.ch/record/2728837.

[77] G Ciezarek et al. “Measurement of B semileptonic decays $B^0 \to D^{*-}\tau^+\nu_\tau$ using the $\tau^+ \to \mu^+\nu_\mu\overline{\nu}_\tau$ decay ”. In: (2014). URL: https://cds.cern.ch/record/1697787.

[78] Kyle Cranmer et al. “HistFactory: A tool for creating statistical models for use with RooFit and RooStats”. In: (June 2012).

[79] I. Antcheva et al. “ROOT — A C++ framework for petabyte data storage, statistical analysis and visualization”. In: *Computer Physics Communications* 180.12 (2009). 40 YEARS OF CPC: A celebratory issue focused on quality software for high performance, grid and novel computing architectures, pp. 2499 –2512. ISSN: 0010-4655. DOI: https://doi.org/10.1016/j.cpc.2009.08.005. URL: http://www.sciencedirect.com/science/article/pii/S0010465509002550.

[80] Roger Barlow and Christine Beeston. "Fitting using finite Monte Carlo samples". In: *Computer Physics Communications* 77.2 (1993), pp. 219 –228. ISSN: 0010-4655. DOI: `https://doi.org/10.1016/0010-4655(93)90005-W`. URL: `http://www.sciencedirect.com/science/article/pii/001046559390005W`.

[81] Jack Wimberley, Brian Keith Hamilton, and Hassan Jawahery. "A measurement of the semitauonic branching fraction ratio $\mathcal{R}(J/\psi)$". In: (2016). URL: `https://cds.cern.ch/record/2202625`.

[82] Marta Calvi et al. *Emulation of the hadronic trigger for tracker-only simulation*. Tech. rep. LHCb-INT-2019-025. CERN-LHCb-INT-2019-025. Geneva: CERN, 2019. URL: `https://cds.cern.ch/record/2703802`.

[83] Johannes Albrecht. "The LHCb Trigger System: Present and Future". In: *J. Phys.: Conf. Ser.* 623.1 (2015), 012003. 5 p. DOI: `10.1088/1742-6596/623/1/012003`. URL: `http://cds.cern.ch/record/2159110`.

[84] Vladimir V Gligorov, Christopher Thomas, and Michael Williams. *The HLT inclusive B triggers*. Tech. rep. LHCb-PUB-2011-016. CERN-LHCb-PUB-2011-016. LHCb-INT-2011-030. LHCb-INT-2011-030. Geneva: CERN, 2011. URL: `https://cds.cern.ch/record/1384380`.

[85] Vladimir V Gligorov. *A single track HLT1 trigger*. Tech. rep. LHCb-PUB-2011-003. CERN-LHCb-PUB-2011-003. LHCb-INT-2010-053. Geneva: CERN, 2011. URL: `https://cds.cern.ch/record/1323812`.

[86] Espen Eie Bowen, Barbara Storaci, and Marco Tresch. *VeloTT tracking for LHCb Run II*. Tech. rep. LHCb-PUB-2015-024. CERN-LHCb-PUB-2015-024. LHCb-INT-2014-040. Geneva: CERN, 2016. URL: `https://cds.cern.ch/record/2105078`.

[87] Ilya Trofimov, Anna Kornetova, and Valeriy Topinskiy. "Using boosted trees for click-through rate prediction for sponsored search". In: (Aug. 2012). DOI: 10.1145/2351356.2351358.

[88] William Detmold, Christoph Lehner, and Stefan Meinel. "$\Lambda_b \to p\ell^-\bar{\nu}_\ell$ and $\Lambda_b \to \Lambda_c\ell^-\bar{\nu}_\ell$ form factors from lattice QCD with relativistic heavy quarks". In: *Physical Review D* 92.3 (2015). ISSN: 1550-2368. DOI: 10.1103/physrevd.92.034503. URL: http://dx.doi.org/10.1103/PhysRevD.92.034503.

[89] R. Aaij et al. "Measurement of b hadron fractions in 13 TeV pp collisions". In: *Physical Review D* 100.3 (2019). ISSN: 2470-0029. DOI: 10.1103/physrevd.100.031102. URL: http://dx.doi.org/10.1103/PhysRevD.100.031102.

[90] Vitalii Lisovskyi. "Study of rare b-baryon decays and test of lepton universality at LHCb". PhD thesis. Sept. 2019.

[91] Carla Marin Benito. "PID strategy and performance at LHCb in Run 2". In: *PoS* ICHEP2018 (2019), 687. 4 p. DOI: 10.22323/1.340.0687. URL: https://cds.cern.ch/record/2702461.

[92] Lucio Anderlini et al. *The PIDCalib package*. Tech. rep. LHCb-PUB-2016-021. CERN-LHCb-PUB-2016-021. Geneva: CERN, 2016. URL: https://cds.cern.ch/record/2202412.

[93] F. Archilli et al. "Performance of the Muon Identification at LHCb". In: *JINST* 8.LHCB-DP-2013-001 (2013). Comments: 17 pages, 10 figures, P10020. 20 p. DOI: 10.1088/1748-0221/8/10/P10020. URL: https://cds.cern.ch/record/1553139.

[94] M. Adinolfi et al. "Performance of the LHCb RICH detector at the LHC". In: *Physical Journal C* 73.5 (2013). ISSN: 1434-6052. DOI: 10.1140/epjc/s10052-013-2431-9. URL: http://dx.doi.org/10.1140/epjc/s10052-013-2431-9.

[95] M. Pivk and F.R. Le Diberder. "A statistical tool to unfold data distributions". In: *Nuclear Instruments and Methods in Physics Research Section A: Accelerators, Spectrometers, Detectors and Associated Equipment* 555.1-2 (2005), 356–369. ISSN: 0168-9002. DOI: `10.1016/j.nima.2005.08.106`. URL: `http://dx.doi.org/10.1016/j.nima.2005.08.106`.

[96] Alex Rogozhnikov. "Reweighting with Boosted Decision Trees". In: *Journal of Physics: Conference Series* 762 (2016), p. 012036. ISSN: 1742-6596. DOI: `10.1088/1742-6596/762/1/012036`. URL: `http://dx.doi.org/10.1088/1742-6596/762/1/012036`.

[97] Philip Nelson. "Naturalness in Theoretical Physics: Internal constraints on theories, especially the requirement of naturalness, play a pivotal role in physics". In: *American Scientist* 73.1 (1985), pp. 60–67. ISSN: 00030996. URL: `http://www.jstor.org/stable/27853063`.

[98] W. Bonivento et al. *Proposal to Search for Heavy Neutral Leptons at the SPS*. 2013. arXiv: `1310.1762 [hep-ex]`.

[99] SHiP Collaboration et al. *A facility to Search for Hidden Particles (SHiP) at the CERN SPS*. 2015. arXiv: `1504.04956 [physics.ins-det]`.

[100] Richard Keith Ellis et al. *Physics Briefing Book: Input for the European Strategy for Particle Physics Update 2020*. Tech. rep. arXiv:1910.11775. 254 p. Geneva, 2019. URL: `http://cds.cern.ch/record/2691414`.

[101] C Ahdida et al. *SHiP Experiment - Comprehensive Design Study report*. Tech. rep. CERN-SPSC-2019-049. SPSC-SR-263. Geneva: CERN, 2019. URL: `https://cds.cern.ch/record/2704147`.

[102] R. Acquafredda et al. "The OPERA experiment in the CERN to Gran Sasso neutrino beam". In: *JINST* 4 (2009), P04018. DOI: `10.1088/1748-0221/4/04/P04018`.

[103] Torbjörn Sjöstrand, Stephen Mrenna, and Peter Skands. "A brief introduction to PYTHIA 8.1". In: *Computer Physics Communications* 178.11 (2008), 852–867. ISSN: 0010-4655. DOI: `10.1016/j.cpc.2008.01.036`. URL: `http://dx.doi.org/10.1016/j.cpc.2008.01.036`.

[104] Costas Andreopoulos et al. *The GENIE Neutrino Monte Carlo Generator: Physics and User Manual*. 2015. arXiv: `1510.05494 [hep-ph]`.

[105] Torbjörn Sjöstrand, Stephen Mrenna, and Peter Skands. "PYTHIA 6.4 physics and manual". In: *Journal of High Energy Physics* 2006.05 (2006), 026–026. ISSN: 1029-8479. DOI: `10.1088/1126-6708/2006/05/026`. URL: `http://dx.doi.org/10.1088/1126-6708/2006/05/026`.

[106] "Heavy Flavour Cascade Production in a Beam Dump". In: (2015). URL: `http://cds.cern.ch/record/2115534`.

[107] S. Agostinelli et al. "GEANT4: A Simulation toolkit". In: *Nucl. Instrum. Meth. A* 506 (2003), pp. 250–303. DOI: `10.1016/S0168-9002(03)01368-8`.

[108] M Al-Turany et al. "The FairRoot framework". In: *Journal of Physics: Conference Series* 396.2 (2012), p. 022001. DOI: `10.1088/1742-6596/396/2/022001`. URL: `https://doi.org/10.1088%2F1742-6596%2F396%2F2%2F022001`.

[109] Claudia Christina Ahdida et al. *SPS Beam Dump Facility: Comprehensive design study*. CERN Yellow Reports: Monographs. 2019. DOI: `10.23731/CYRM-2020-002`. URL: `https://cds.cern.ch/record/2703984`.

[110] J Beacham et al. "Physics beyond colliders at CERN: beyond the Standard Model working group report". In: *Journal of Physics G: Nuclear and Particle Physics* 47.1 (2019), p. 010501. ISSN: 1361-6471.

DOI: 10.1088/1361-6471/ab4cd2. URL: http://dx.doi.org/10.1088/1361-6471/ab4cd2.

[111] C Ahdida et al. *SHiP Experiment - Progress Report*. Tech. rep. CERN-SPSC-2019-010. SPSC-SR-248. Geneva: CERN, 2019. URL: https://cds.cern.ch/record/2654870.

[112] Oliver Lantwin. “Optimisation of the SHiP experimental design”. Presented 09 May 2019. 2019. URL: https://cds.cern.ch/record/2693177.

[113] K. Kodama et al. “Final tau-neutrino results from the DONuT experiment”. In: *Phys. Rev. D* 78 (2008), p. 052002. DOI: 10.1103/PhysRevD.78.052002. arXiv: 0711.0728 [hep-ex].

[114] Giovanni De Lellis. “The SHiP experiment at CERN”. In: *J. Phys. : Conf. Ser.* 1137.1 (2019), 012059. 6 p. DOI: 10.1088/1742-6596/1137/1/012059. URL: http://cds.cern.ch/record/2710062.

[115] F Hahn et al. *NA62: Technical Design Document*. Tech. rep. Geneva: CERN, 2010. URL: https://cds.cern.ch/record/1404985.

[116] SHiP Collaboration. *Addendum to Technical Proposal: A Facility to Search for Hidden Particles (SHiP) at the CERN SPS*. Tech. rep. CERN-SPSC-2015-040. SPSC-P-350-ADD-2. Geneva: CERN, 2015. URL: https://cds.cern.ch/record/2060742.

[117] Sibila Gómez et al. “MUSIC: An 8 channel readout ASIC for SiPM arrays”. In: Apr. 2016, 98990G. DOI: 10.1117/12.2231095.

[118] A. Blanco et al. “The SHiP timing detector based on MRPC”. In: *JINST* 15.10 (2020). Ed. by Barbara Liberti, Alessandro Paoloni, and Paolo Camarri, p. C10017. DOI: 10.1088/1748-0221/15/10/C10017.

[119] SHiP Collaboration. *Sensitivity of the SHiP experiment to Heavy Neutral Leptons*. 2019. arXiv: 1811.00930 [hep-ph].

[120] Gianluca Lamanna et al. "NA62 and NA48/2 results on search for Heavy Neutral Leptons". In: *EPJ Web Conf.* 179 (2018), 01009. 6 p. DOI: 10.1051/epjconf/201817901009. URL: https://cds.cern.ch/record/2682879.

[121] Ayuki Kamada, Masaki Yamada, and Tsutomu T. Yanagida. "Strongly-interacting massive particle and dark photon in the era of the intensity frontier". In: *Physical Review D* 102.7 (2020). ISSN: 2470-0029. DOI: 10.1103/physrevd.102.075001. URL: http://dx.doi.org/10.1103/PhysRevD.102.075001.

[122] Lincoln Wolfenstein. "Parametrization of the Kobayashi-Maskawa Matrix". In: *Phys. Rev. Lett.* 51 (21 1983), pp. 1945–1947. DOI: 10.1103/PhysRevLett.51.1945. URL: https://link.aps.org/doi/10.1103/PhysRevLett.51.1945.

[123] Victoria Bayliss, M Courthold, and T Rawlings. "Active Muon Shield - Preliminary Design Report". In: (2015). URL: https://cds.cern.ch/record/2027801.

[124] F. James. "MINUIT Function Minimization and Error Analysis: Reference Manual Version 94.1". In: (1994).

[125] M. Al-Turany et al. "The FairRoot framework". In: *J. Phys. Conf. Ser.* 396 (2012). Ed. by Michael Ernst et al., p. 022001. DOI: 10.1088/1742-6596/396/2/022001.

[126] R. Brun and F. Rademakers. "ROOT: An object oriented data analysis framework". In: *Nucl. Instrum. Meth. A* 389 (1997). Ed. by M. Werlen and D. Perret-Gallix, pp. 81–86. DOI: 10.1016/S0168-9002(97)00048-X.

[127] K. Hayasaka et al. "Search for lepton-flavor-violating τ decays into three leptons with 719 million produced pairs". In: *Physics Letters B* 687.2-3 (2010), 139–143. ISSN: 0370-2693. DOI: 10.1016/

j.physletb.2010.03.037. URL: http://dx.doi.org/10.1016/j.physletb.2010.03.037.

[128] R. Aaij et al. "Search for the lepton flavour violating decay $\tau^- \to \mu^-\mu^+\mu^-$". In: *Journal of High Energy Physics* 2015.2 (2015). ISSN: 1029-8479. DOI: 10.1007/jhep02(2015)121. URL: http://dx.doi.org/10.1007/JHEP02(2015)121.

[129] E Kou et al. "The Belle II Physics Book". In: *Progress of Theoretical and Experimental Physics* 2019.12 (2019). ISSN: 2050-3911. DOI: 10.1093/ptep/ptz106. URL: http://dx.doi.org/10.1093/ptep/ptz106.

[130] Thomas Ruf and Eric Van Herwijnen. "Description of the SHiP FixedTargetGenerator". In: (2017). URL: https://cds.cern.ch/record/2280572.